

The Radio Fundamental Catalogue. I. Astrometry

L. Y. PETROV¹ AND Y. Y. KOVALEV²

¹*NASA Goddard Space Flight Center, Code 61A, 8800 Greenbelt Rd, Greenbelt, 20771 MD, USA*

²*Max-Planck-Institut für Radioastronomie, Auf dem Hügel 69, 53121 Bonn, Germany*

(Received August 12, 2024; Revised October 12, 2024; Accepted October 14, 2024; Published January 16, 2025)

Submitted to ApJS

ABSTRACT

We present an all-sky catalog of absolute positions and estimates of correlated flux density of 21,942 compact radio sources determined from processing interferometric visibility data of virtually all very long baseline interferometry (VLBI) observing sessions at 2–23 GHz from 72 programs suitable for absolute astrometry collected for 30 years. We used a novel technique of generation of a data set of fused observables that allowed us to incorporate all available data in our analysis. The catalog is the most complete and most precise to date. It forms the foundation and reference for positional astronomy, space geodesy, space navigation, and population analysis of active galactic nuclei (AGNs), and provides calibrators for phase referencing for differential astrometry and VLBI astrophysical observations. Its accuracy was evaluated through a detailed accounting of systematic errors, rigorous decimation tests, comparison of different data sets, and comparison with other catalogs. The catalog preferentially samples AGNs with strong contemporary parsec-scale synchrotron emission. Its milliarcsecond-level positional accuracy allows association of these AGNs with detections in a wide range of the electromagnetic spectrum from low-frequency radio to γ -rays and high-energy neutrinos. We describe the innovative data processing and calibration technique in full detail, report the in depth analysis of random and systematic positional errors, and provide a list of associations with large surveys at different wavelengths.

Keywords: astrometry — catalogues — surveys — VLBI

1. INTRODUCTION

The method of very long baseline interferometry (VLBI), first proposed by Matveenko et al. (1965) allows us to determine positions of compact radio sources with a nanoradian level of accuracy (1 nrad \approx 0.2 mas). The very first VLBI catalogue contained coordinates of 35 objects (Cohen & Shaffer 1971), which are active galactic nuclei (AGNs). Since then, VLBI observations became routine for geodesy, astronomy, astrophysics, and space navigation. It was realized in 1980s that the list of sources with precisely known positions and their images at different frequencies needed to be expanded.

To achieve the goals of space geodesy — a millimeter level of accuracy in ground station position determination — a list of 100–300 bright extragalactic sources uniformly distributed over the sky with positions known at subnanoradian accuracy is necessary. To achieve the goals of space navigation — a nanoradian level of accuracy for spacecraft tracking — a list of 1000–2000 sources within $\pm 7^\circ$ of the ecliptic plane with positions known at a subnanoradian level is highly desirable. To achieve goals of astronomical VLBI observations with the use of the phase referencing technique, a larger pool of extragalactic sources with positional accuracy at the same level and with known distributions of flux density is required. When observations are performed in the phase referencing mode, the radio telescopes of an array quickly switch from a target source to a calibrator within several degrees, which allows one to extend the integration time

beyond the coherence limit set by the atmosphere and detect weaker targets and determine an offset of the target with respect to a calibrator. We performed a Monte Carlo simulation and found that it is sufficient to have 6710 calibrator sources uniformly distributed over the celestial sphere in order to find a calibrator within 3° of a given direction with the probability of 99% assuming the sources are distributed uniformly. This number raises to 15,100 if a calibrator within 2° of a given direction has to be found with that confidence level. The closer the calibrator to the target, the better the atmospheric propagation errors are compensated. Martí-Vidal et al. (2010) has characterized quantitatively the impact of residual errors on the quality of results as a function of target-to-calibrator separation. In general, a target-to-calibration separation less than 2° is desirable, a separation of $2\text{--}5^\circ$ is favorable, and a separation greater than 5° should be avoided.

Phase calibration is also used for differential astrometry. Accuracy at tens of microarcsecond can be achieved for the *positional offsets* from observations in a phase referencing mode (Reid & Honma 2014; Reid et al. 2017). A similar technique is also applicable to observations of spacecrafts (Jones et al. 2020). We should note that although differential phase referencing VLBI allows one to evaluate position offsets with respect to a calibrator with very high precision, this does not necessarily mean that a source position can be derived with that level of accuracy. The uncertainty of a target position is the sum in quadrature of the uncertainty of the positional offset and the calibrator positional uncertainty. Therefore, positional accuracy of a target source cannot be greater than the positional accuracy of a calibrator, which may be orders of magnitude worse.

A good calibrator should be strong and compact in order to be detectable with a relatively short integration time at all VLBI baselines, have a simple structure in order to reduce the errors of the fringe phase model, and have a precise position in the range of 0.2 to 10 mas depending on an application. Considering that not all calibrators fulfill these criteria and considering the nonuniformity of the distribution of AGNs over the sky, a list of $\sim 20,000$ calibrators with precise astrometry and photometry are required.

A list of sources with precisely determined coordinates forms the reference to which positions of other objects are referred to and it serves as the basis for celestial object localization. Therefore, such lists are often called “reference frames.” Since currently VLBI is one the two most precise astrometry techniques, a list of these sources provides the foundation to the positional astronomy.

Detection of a large number of sources allows us to study a population of compact objects that are almost exclusively AGNs. Not all AGNs are compact enough to be detected with VLBI at baselines longer than 100 km. Correlating the milliarcsecond-scale morphology of detected sources with the arcsecond-scale morphologies, spectral indices, and variability, provides rich information about AGNs and is a key for understanding their nature. Lists of sources that form complete samples according to certain criteria are especially valuable because sample statistics derived from their analysis can be generalized to the entire population. Since AGNs are distributed uniformly over the sky, analysis of the dependence of their apparent size versus frequency allows us to study not only their intrinsic properties, but also the scattering properties of the interstellar medium in our Galaxy (e.g., Pushkarev & Kovalev 2015; Koryukova et al. 2023).

Bright compact radio sources are relatively rare objects. The majority of them are blazars, a class of AGNs with jets pointing towards the observer with a viewing angle less than 10° . Knowing their statistics, the probability to find a compact AGN with the certain flux density within a specified search area from a given direction by chance can be evaluated. This probability is often small enough can be used to draw an important conclusion that the sources found in that specified search area are the same object with a high confidence level. This approach was successfully used for association of γ -ray sources detected by the *Fermi* LAT space telescope with AGNs (Kovalev 2009; Petrov et al. 2013; Schinzel et al. 2015, 2017; Ajello et al. 2020). Selection of high-energy neutrino associations, as well as estimates of an associated p-value can be achieved using a catalogue of compact radio sources, provided it covers all sky and it is complete at a certain flux density limit, as it has been demonstrated in Plavin et al. (2020, 2021, 2023); Bellenghi et al. (2023); Abbasi et al. (2023).

Recognizing the values of a list of compact radio sources detectable with VLBI with very precise positions, a number of observing programs for absolute astrometry were launched since 1980s. The criteria for specific programs varied, but the overarching goal was to produce an all-sky complete list of $\sim 20,000$ AGNs that are detectable at 2–20 GHz at baselines 1,000–10,000 km, determine their positions with a milliarcsecond level of accuracy, and get their images.

It took over four decades to achieve the goals of this endeavor. Although observing programs are still continuing and are expected to be continued, we think we reached a turning point after which a further expansion of the VLBI absolute astrometry catalogue is expected to approach to a stall just because of a planet-wide resource limit, and

the situation will not change before a new generation of sensitive instruments, Square Kilometer Array (SKA) and next-generation Very Large Array (ngVLA), will become fully operational in the 2030s.

Here we present the Radio Fundamental Catalogue (RFC) which is the result of our analysis of virtually all publicly available VLBI data that are suitable for the goal, including a large number of observing programs that we have initiated. To date, these analysis efforts are the most extensive and counting the number of visibilities processed exceed by an order of magnitude previous efforts. The Radio Fundamental Catalogue contains precise positions determined with a method of absolute astrometry and estimates of correlated flux densities at three ranges of projected baseline lengths. We present the RFC in its current state on 2024.10.05 as data release rfc_2024c. We will continue to provide online releases on a quarterly basis.

We split the material in Paper I (here) and future Paper II focusing the first paper on description of the observations, their analysis and astrometry results. The scope of Paper II is a study of the source counts and sky distribution, sample completeness, parsec-scale observational characteristics and astrophysical properties of extragalactic objects with strong contemporary compact radio emission. In this Paper I we make an overview of the observing programs in section 2, present the VLBI data analysis technique in section 3, describe in detail the analysis of positional error in section 4, outline the imaging results in section 5, describe the catalogue in section 6, and provide a discussion of produced results in section 7. The summary and concluding remarks are presented in section 8 followed by the Appendix that describes the machine-readable tables. The Radio Fundamental Catalogue is accompanied with the Astrogeo VLBI FITS image database that cannot be put in the attachment because of its size (212 GB) and it accessible at <https://doi.org/10.25966/kyy8-yp57>.

2. OBSERVING CAMPAIGNS

VLBI observations are organized in campaigns that can contain one or more segments also called experiments. Antennas of a given array slew to a given source and collect voltage data during a specified period of time, from 10 to 600 s. These data collections are called scans. Some stations of an array may not participate in a given scan either by design or are dropped for technical reasons. Cross-correlated data from a given scan and a given pair of participating stations are called observations. When N stations participated in a given scan, there are $N \times (N + 1)/2$ observations.

2.1. *Dedicated astronomical experiments*

A target source or several target sources, as well as a number of calibrator sources, are observed for 1–12 hours in a typical astronomical VLBI experiment. Such sources are studied in detail at full sensitivity that is achieved owing to a long integration time. This allows us to reconstruct high fidelity images and/or determine highly accurate source positions using differential VLBI. In contrast, tens to hundreds of sources are observed in a single survey experiment, and a VLBI survey campaign may involve observations of up to several thousand sources. The goal of survey experiments is to study a population of sources. Inevitably, shorter integration times are used in survey experiments. That results in poorer images and worse positional accuracy than in dedicated experiments, but a much larger number of objects is observed in a single experiment.

Most of the surveys fall into three categories: pathfinder surveys, follow-up surveys, and high-frequency extensions. The goal of a pathfinder survey is to detect target sources never observed with VLBI before, to determine their positions at a milliarcsecond level of accuracy, to measure their correlated flux density, and to synthesize their images from collected visibility data. Since VLBI has a small field of view, typically in the range of $10''$ to $5'$ at 2–24 GHz, blind surveys would be very inefficient, because the probability to find by chance a source with a VLBI flux density of 10–1000 mJy within such a narrow field of view is very low. Therefore, target sources in pathfinder surveys are selected among those that have been addlppreviously detected in prior connected radio interferometers at resolutions of 1–40'' or in single dish observations at resolutions of $0.5'–5'$, and VLBI observations just follow up objects already detected at low resolutions. Only a fraction of target sources is detected with a given VLBI pathfinder survey. Depending on criteria used for source selection, which typically involve information about total flux density, sometimes supplemented by radio spectral indexes, the fraction of detected sources is in the range of 20 to 98% (e.g., Kovalev et al. 2007; Popkov et al. 2021), with 59% being the median fraction. Selecting targets with flat radio spectra significantly increases detectability since such samples strongly favour blazars with dominant Doppler-boosted opaque compact cores (Popkov et al. 2021). However, this strategy imposes a selection bias. To overcome this bias, observing programs since 2015 gradually eliminated that criterion.

The follow-up VLBI surveys target samples of sources previously detected in VLBI pathfinder programs with the goal to improve positional accuracy or get higher quality images. The radio telescope sensitivity is usually the highest

in the range of 1–9 GHz, and source flux density is usually falling with frequency. Therefore, the chances to detect a source using given integration time are in general higher at lower frequencies. Sources detected at low frequencies are often followed up at higher frequencies in the third type of surveys called high-frequency extensions. The goal of these extensions is to get source images at higher frequencies that better characterize the core region close to the true jet base due to opacity conditions (e.g., Lobanov 1998), evaluate the suitability of target sources as calibrators at high frequencies, and in some cases to improve their positional accuracy.

In our work we collected data from *all* VLBI surveys above 2 GHz for which visibility data are available from public archives, including surveys that we designed ourselves or participated as co-investigators. Additionally, we combed through VLBI data archives and examined observing campaigns in continuum at frequencies above 4 GHz that observed 16 or more target sources without the use of phase calibrators. We also included all geodetic VLBI data collected under observing programs for determination of station positions, station velocities, and the Earth orientation parameters (EOPs) since April 1980 as an auxiliary dataset. Although including these data in our solutions had only a marginal direct impact on source position estimates, their use significantly improved estimates of station positions and the EOPs that are nuisance parameters in the context of this work, but are essential for reducing systematic errors related to the positional stability of the VLBI network and its motion with respect to the coordinate system origin.

Radio wave propagation is described by differential equations against source coordinates and other variables. Their solution requires three arbitrary initial conditions that define the orientation of the celestial coordinate system, as well as initial conditions that define the origin and orientation of the terrestrial coordinate system. If experiments have no common sources and common stations, i.e. are totally disjoint, source positions derived from each single experiment have arbitrary rotations with respect to source positions derived from another experiments. Although it still possible to align positions derived from different experiments, the alignment procedure would introduce additional errors, which we would like to avoid. Therefore, a given VLBI survey experiment by design has a number of common sources with other experiments.

When each observing session has common stations and common sources, the whole dataset can be processed in a single least squares solution. Common stations and common sources tie the dataset together. When the number of common stations or common sources is small, the impact of random errors on positions of common stations and common sources on position estimates of other sources is nonnegligible. To avoid this, the number of common stations and sources should be sufficiently large. In addition to avoiding degeneracies in estimation of coordinates, sources are observed in many campaigns for improving their positions and/or image quality by collecting more data, for examining their properties at different frequencies, or by mistake because a target source was not checked thoroughly whether it has been detected in previous campaigns. The share of unique sources that are detected only in a given campaign is in the range from 0 to 88%.

Below we list all observational programs we used in our work. For those observational programs for which we found no bibliographic reference we used the principal investigator name instead. We present the experiment name, acronym when available, the VLBI array, band, the experiment ID, duration, and the source selection criteria when known.

I. Pathfinder surveys:

1. VLBA Calibrator survey 1 (VCS1), Beasley et al. (2002); VLBA BB023; dual X/S bands; 11 segments; since 1994.08.12 through 1997.08.27. Selection criteria: 1) declinations $> -30^\circ$ and 2) detected in the Jodrell Bank–VLA Astrometric Survey JVAS (Patnaik et al. 1992; Browne et al. 1998; Wilkinson et al. 1998), an astrometric snapshot survey of compact radio sources performed with the NRAO Very Large Array during the period 1990–1993.
2. Phase-references superluminals, PI: T. Beasley; VLBA BB041; dual X/S bands; 2 segments; since 1995.06.25 through 1996.02.16.
3. The VSOP Pre-launch VLBA Observations (VLBApls), Fomalont et al. (2000); VLBA BH019; C-band; 1 segment; 1996.06.05. Selection criteria: 1) total flux density at 5 GHz > 1.0 Jy, and 2) spectral index flatter than -0.5^1 , and 3) Galactic latitude $|b| > 10^\circ$.
4. A VLBA Survey of Flat-Spectrum FIRST Sources, Ulvestad et al. (1999); VLBA BU007; C-band; 1 segment; 1996.12.19. Selection criteria: 1) total flux density greater than 50 mJy at 4.85 GHz, from the GB6 survey

¹ Spectral index α is defined as $f^{+\alpha}$ in this work, where f is frequency. We call sources with $\alpha > -0.5$ flat-spectrum objects.

- (Gregory et al. 1996), and 2) two-point spectral indices flatter than -0.5 between 1.4 GHz FIRST (White et al. 1997) and 4.85 GHz (GB6, Gregory et al. 1996), and 3) right ascension range $6-17^h$ and declination from $+29^\circ$ to $+34^\circ$.
5. The Bologna Complete Sample of Nearby Radio Sources, Liuzzo et al. (2009); VLBA BG069, BG094, BG158; 3 segments; since 1997.04.06 through 2000.01.22. Selection criteria: 1) flux density > 0.25 Jy at 408 MHz from the B2 Catalogue of Radio Sources (Fanti et al. 1974) and the Third Cambridge Revised Catalogue (Smith et al. 1976), and 2) flux density at 178 MHz > 10 Jy from the 3CR catalogue, and 3) declination $> 10^\circ$, and 4) galactic latitude $|b| > 15^\circ$, and 5) redshift $z < 0.1$.
 6. Caltech Jodrell Bank snapshot survey, Britzen et al. (2007); VLBA BB119; C-band; 3 segments; since 1999.11.21 through 1999.11.26. Selection criteria: 1) declination $> +35^\circ$, and 2) galactic latitude $|b| > 10^\circ$, and 3) flux density 5 GHz > 0.35 Jy, and 4) spectral index flatter than -0.5 between 1.4 and 4.85 GHz from analysis of NVSS (Condon et al. 1998) and GB6 (Gregory et al. 1996) surveys.
 7. Densification of the International Celestial Reference Frame, Charlot et al. (2004); EVN EC013, EC017; dual X/S bands; 3 segments; since 2000.05.31 through 2003.10.17. Selection criterion: detected in JVAS.
 8. VLBA Calibrator survey 2 (VCS2), Fomalont et al. (2003); VLBA BF071; dual X/S bands; 2 segments; since 2002.01.31 through 2002.05.14. Selection criteria: 1) declination zone $-45^\circ < -30^\circ$, or 2) galactic latitude $|b| < 10^\circ$, and 3) not observed in VCS1.
 9. VLBA observations of compact 9C sources, Bolton et al. (2006a); VLBA BB177; C band; 1 segment; 2004.02.06; Selection criteria: sources with 15 GHz variability.
 10. VLBA Calibrator survey 3 (VCS3), Petrov et al. (2005); VLBA BP110; dual X/S bands; 3 segments; since 2004.04.30 through 2004.05.27. Selection criteria: 1) declination $> -45^\circ$, and 2) total flux density > 100 mJy at both at 2.3 and 8.6 GHz, and 3) spectral index flatter than -0.5 , and 4) have no known calibrator within 3.9° .
 11. VLBA Calibrator survey 4 (VCS4), Petrov et al. (2006); VLBA BP118; dual X/S bands; 3 segments; since 2005.05.12 through 2005.06.30. Selection criteria: multiple criteria with the primary goal to observe sources in the areas where no prior VLBI calibrator objects within 4° radius are known.
 12. Observations of compact sources selected at 15 GHz, Bolton et al. (2006b); VLBA BC151; X/C band; 4 segments; since 2005.06.16 through 2005.08.04. Selection criteria: sources with 15 GHz variability.
 13. VLBA Calibrator survey 5 (VCS5), Kovalev et al. (2007), VLBA BK124; dual X/S bands; 3 segments; since 2005.07.08 through 2005.07.20. Selection criteria: 1) declination $> -30^\circ$, and 2) spectral index flatter than -0.5 , and 3) flux density interpolated at 8.6 GHz using data from multiple radio astronomy catalogues > 150 mJy.
 14. VLBA Imaging and Polarimetry Survey at 5 GHz (VIPS), Helmboldt et al. (2007); Petrov & Taylor (2011); VLBA BT085; C-band; 16 segments; since 2006.01.03 through 2006.08.12. Selection criteria: 1) declination $> +15^\circ$ and $< +65^\circ$, and 2) flux density > 0.085 Jy, and 3) present in the Cosmic Lens All-Sky Survey (CLASS) (Myers et al. 2003), and 4) present in the Sloan Digital Sky Survey SDSS (York et al. 2000) footprint.
 15. The VLBA Galactic Plane Survey (VGaPS), Petrov et al. (2011a); VLBA BP125; K-band; 3 segments; since 2006.02.04 through 2006.10.20. Selection criteria: 1) all detected sources from the VERA 22 GHz Fringe Search Survey (Petrov et al. 2007), and 2) flux density interpolated at 22 GHz using data from multiple radio astronomy catalogues > 0.2 Jy, and 3) spectral index flatter than -0.5 , and 4) galactic latitude $|b| < 10^\circ$.
 16. Northern Polar Cup Survey, Popkov et al. (2021); VLBA BK130; dual X/S bands; 3 segments; since 2006.02.14 through 2006.02.23. Selection criteria: 1) declination $> +75^\circ$ and 2) flux density > 0.2 Jy from NVSS.
 17. Compactness of weak radio sources at high frequencies, Majid et al. (2009); VLBA BM252; X-band; 2 segments; since 2006.11.06 through 2006.11.13. Selection criteria: 1) flux density at 31 GHz > 10 mJy and 2) two right ascension fields near 2^h and 20^h .
 18. VLBA Calibrator survey 6 (VCS6), Petrov et al. (2008), VLBA BP133; dual X/S bands; 3 segments; since 2006.12.18 through 2007.01.11. Selection criteria: 1) declination $> -30^\circ$, and 2) spectral index flatter than

- 0.5, and 3) flux density interpolated at 8.6 GHz using data from multiple radio astronomy catalogues > 0.2 Jy, or 4) intra-day variable sources observed in the framework of the MASIV survey (Lovell et al. 2003) and flux density > 130 mJy.
19. VERA Galactic Plane Survey, PI: L. Petrov; VERA R07030A, R07100A; K-band; 2 segments; since 2007.01.30 through 2007.03.21. Selection criteria: 1) either within 6° of the Galactic plane, or 2) within 11° of the Galactic center, or 3) within 2° of a known maser source, and 4) detected in the VERA Fringe Search Survey (Petrov et al. 2007).
 20. LBA Calibrator Survey-1 (LCS-1), Petrov et al. (2011b); LBA V230R, V254, V271AR, V271BR, V271CR; X-band; 5 segments since 2008.02.05 through 2009.12.12. Selection criteria: 1) declination $< -45^\circ$, and 2) flux density at 8.3 GHz > 150 mJy from 20 GHz AT20G (Murphy et al. 2010), and 3) spectral index flatter than -0.6 .
 21. Searching for candidate radio sources for the GAIA astrometric link (OBRS-1), (Petrov 2011); VLBA+EVN GC030; 1 segment; 2008.03.07. Selection criteria: 1) cross-match of NVSS and the catalogue of quasars and active nuclei (Véron-Cetty & Véron 2010), and 2) $B_{\text{mag}} < 18$, and 3) $\delta > -40^\circ$.
 22. The EVN Galactic Plane Survey (EGaPS), (Petrov 2012); EVN EP066; K band; 1 segment; 2009.10.27. Selection criteria: 1) galactic latitude $|b| < 6^\circ$, and 2) declination $> -20^\circ$, and 3) flux densities extrapolated to 22 GHz > 80 mJy using at least two measurements above 2 GHz, and 4) spectral indices flatter than -0.5 .
 23. Bessel Calibrator Search (BeSSeL), (Immer et al. 2011); VLBA BR145; X-band; 34 segments; since 2009.11.16 through 2010.08.29. Selection criteria: 1) point-like sources from the NVSS (sizes $< 20''$), and 2) present in CORNISH catalogs Purcell et al. (2008) with flux densities above 30 mJy, and 3) within circles with a radius of 1.5° around the 109 target maser sources formed of the BeSSeL program.²
 24. Low Luminosity gamma-ray blazars, (Linfood et al. 2012); VLBA S2078, BT110; C-band; 7 segments; since 2009.11.22 through 2010.07.30. Selection criteria: 1) present in the γ -ray Fermi Large Area Telescope First Source Catalog 1FGL (Abdo et al. 2010) and 2) brighter than 30 mJy at 8 GHz from CRATES catalogue (Healey et al. 2007), or 3) detected with VIPS survey (Helmboldt et al. 2007).
 25. LBA Calibrator Survey-2 (LCS-2), (Petrov et al. 2019a); LBA V271DR, V271ER, V271F, V271G, V271H, V271I, V271J, V271K, V271L, V271M, V271N, V271O, V441, V493; X band; 14 segments; since 2010.03.11 through 2016.06.28. Selection criteria: 1) declination $< -40^\circ$, and 2) spectral index flatter than -0.5 , and 3) present in the Parkes quarter-Jansky survey Jackson et al. (2002) with flux density interpolated to 8 GHz > 0.2 Jy, or 4) present in ATC20G catalogue (Murphy et al. 2010) with flux density m interpolated to 8 GHz > 0.15 Jy, or 5) present in the Parkes-MIT-NRAO (PMN) catalogue (Griffith & Wright 1993; Wright et al. 1994; Griffith et al. 1994; Condon et al. 1993; Tasker et al. 1994; Griffith et al. 1995; Wright et al. 1996) with flux density interpolated to 8 GHz > 0.18 Jy, or 6) present in the Australia Telescope Parkes-MIT-NRAO ATPMN (McConnell et al. 2012) catalogue with flux density interpolated to 8 GHz > 0.17 Jy.
 26. Searching for candidate radio sources for the Gaia astrometric link and Global VLBI observations of weak sources (OBRS-2), (Petrov 2013); VLBA+EVN GC034, GB073; 7 segments; since 2010.03.23 through 2012.05.27. Selection criteria: 1) declination $\delta > -40^\circ$, and 2) present either in NVSS, and 3) present in the catalogue of quasars and active nuclei (Véron-Cetty & Véron 2010), and 4) $B_{\text{mag}} < 18$.
 27. A systematic search for inspiraling, binary, and recoiling black holes in nearby galaxies (V2M), (Condon et al. 2017); VLBA BC191, BC196, BC201; X band; 94 segments; since 2010.07.15 through 2012.06.05. Selection criteria: 1) declination $> -40^\circ$, and 2) identified as a galaxy with $K_{20fe} < 12.25$ mag from 2MASS catalogue (Skrutskie et al. 2006), and 3) NVSS flux density > 50 mJy.
 28. 1FGL Active Galactic Nuclei at parsec scales, PI: Y. Kovalev; VLBA S3111; X-band; 3 segments; since 2010.12.05 through 2011.01.09. Selection criteria: 1) declination $> -40^\circ$ and 2) detected γ -ray emission with Fermi in 1FGL (Abdo et al. 2010) and associated with a radio source not observed before with VLBI.

² <https://www3.mpifr-bonn.mpg.de/staff/abrunthaler/BeSSeL/index.shtml>

29. Bessel Calibrator Search follow-on, PI: M. Reid; VLBA BR149, BM317; X-band; 14 segments; since 2010.02.06 through 2013.08.04. Selection criterion: sources within 3° of the Galactic plane in a close distance to target sources of the BeSSeL program.
30. VLBA Calibrator Densification 7 (VCS7), (Petrov 2021); VLBA BP171; dual X/C bands; 17 segments; since 2013.02.08 through 2013.08.01. Selection criteria: 1) declinations $> -45^\circ$, and 2) flux densities extrapolated at 8 GHz > 0.1 Jy, and 3) spectral index > -0.55 , and 4) no planetary nebulae or HII region within $2'$.
31. 2FGL Active Galactic Nuclei at Parsec Scales, PI: Y. Kovalev; VLBA S4195; X-band; 3 segments; since 2013.05.07 through 2013.06.22. Selection criteria: 1) declination $> -40^\circ$ and 2) detected γ -ray emission with Fermi in 2FGL (Nolan et al. 2012) and associated with a radio source.
32. VLBI follow-up of Fermi sources, (Schinzel et al. 2015); VLBA S5272; X-band, 4 segments; since 2013.08.06 through 2013.12.05. Selection criteria: 1) declination -45° , and 2) flux density > 10 mJy at 4.5 or 8.4 GHz, and 3) detected with Very Long Array (VLA) or Australia Telescope Compact Array (ATCA) within the 95% localization error ellipse of γ -ray sources reported in 2FGL Fermi catalogue.
33. VLBA Calibrator Densification 8 (VCS8), (Petrov 2021); VLBA BP177; dual X/C bands; 10 segments; since 2014.01.07 through 2014.02.23. Selection criteria: 1) declinations $> -45^\circ$, and 2) flux densities extrapolated at 8 GHz and greater 150 mJy, and 3) spectral index > -0.55 , and 4) no planetary nebulae or HII region with $2'$.
34. VLBI Ecliptic band survey with the CVN (VEPS-1), (Shu et al. 2017); CVN VEPS; X band; 17 segments; since 2015.02.13 through 2017.12.14. Selection criteria: 1) ecliptic latitude $|\beta| < 7.5^\circ$ and 2) present in GB6 and PMN catalogues with flux density at 5 GHz > -0.05 Jy.
35. 2FGL AGNs at parsec scales, 2nd survey, (Schinzel et al. 2015); VLBA BS241; X-band; 7 segments; since 2015.02.16 through 2015.07.01. Selection criteria: 1) declination $> -40^\circ$ and 2) detected γ -ray emission with Fermi in 2FGL (Nolan et al. 2012) and associated with a radio source.
36. VLBA Calibrator Densification 9 (VCS9), (Petrov 2021); VLBA BP192; dual X/C bands; 99 segments; since 2015.08.07 through 2016.09.07. Selection criteria: 1) declinations $> -40^\circ$ and 2) flux density at 4.8 GHz > 0.07 Jy from GB6 or PMN catalogues.
37. 3FGL at parsec scales, (Schinzel et al. 2017); VLBA S7104; X-band; 9 segments; since 2016.06.27 through 2016.07.26. Selection criteria: 1) declinations $> -40^\circ$ and 2) detected with Very Long Array (VLA) or Australia Telescope Compact Array (ATCA) within the 95% localization error ellipse of γ -ray sources reported in 3FGL Fermi catalogue (Acero et al. 2015), and 3) flux density at 5 or 9 GHz > 10 mJy.
38. Search for SOuthern Fermi Unassociated sources (SOFUS), PI: L. Petrov; LBA SOFUS, V592, WARK1; X-band; 4 segments; since 2017.04.07 through 2021.05.08. Selection criteria: 1) declinations $< -40^\circ$ and 2) detected with Australia Telescope Compact Array (ATCA) within the 95% localization error ellipse of γ -ray sources reported in 3FGL Fermi catalogue (Acero et al. 2015) 3) Flux density at 5 or 9 GHz > 10 mJy.
39. VLBA Survey of unassociated gamma-ray objects in the 7-year Fermi/LAT catalog. PI: F. Schinzel, VLBA BS262; dual X/C bands; 21 segments; since 2018.04.08 through 2018.07.24. Selection criteria: 1) declinations $> -40^\circ$ and 2) detected with Very Long Array (VLA) within the 95% localization error ellipse a γ -ray source reported in 4FGL Fermi catalogue (Abdollahi et al. 2022). Flux density at 5 or 9 GHz > 10 mJy.
40. VLBA Survey of unassociated gamma-ray objects in the 7-year Fermi/LAT catalog, 2nd survey. PI: F. Schinzel; VLBA SB072; dual X/C bands; 31 segments; since 2018.08.25 through 2019.02.17. Selection criteria: 1) declinations $> -40^\circ$ and 2) detected with Very Long Array (VLA) within the 95% localization error ellipse a γ -ray source reported in 4FGL Fermi catalogue (Abdollahi et al. 2022), and 3) flux density at 5 or 9 GHz > 10 mJy.
41. Study of the population of steep-spectrum compact radio sources, XC part (VCS10); VLBA BP242, BP245; dual X/C bands; 19 segments; since 2019.07.24 through 2020.02.11. Selection criteria: 1) declinations $> -40^\circ$ and $< 0^\circ$, and 2) all sources from AT20G not observed before with VLBI, regardless of their spectral index, or 3) flux density from GB6 and PMN catalogues > 0.07 mJy and ecliptic latitude $|\beta| < 7.5^\circ$.
42. A search for high-frequency calibrators within 10 degrees of the Galactic center, PI: L. Petrov; KVN N20LP01; K and Q bands; 14 segments; since 2020.03.05 through 2020.06.16. Selection criteria: 1) angular

- distance to the Galactic center less than 10° , and 2) known objects detected with VLBI at 2–8 GHz but never observed at 22/43 GHz, and 3) sources from VLASS (Gordon et al. 2021) with peak flux density > 30 mJy and the ratio total/peak flux density less than 1.5, and 4) have never been observed with VLBI.
43. VLBA flux-limited Surveys of VLASS Fields — Pilot Observations; PI: A. Beasley VLBA BB409; C band; 4 segments; since 2020.05.20 through 2020.07.20. Selection criterion: detected with VLASS in three fields.
 44. Completion of Surveys for a Gravitational Lens Search to Explore Dark Matter (VCS11), PI: T. Readhead; VLBA BR235; 18 segments; since 2020.09.11 through 2021.02.16. Selection criteria: 1) declinations $> -40^\circ$ and 2) sources from CLASS and CRATES catalogues with flux density > 49.4 mJy.
 45. Reaching completeness of the VLBI-selected AGN sample North of -40 deg (VCS12) PI: L. Petrov VLBA BP252; dual X/C bands; 53 segments; since 2021.09.21 through 2022.12.02. Selection criteria: 1) declinations $> -40^\circ$, and 2) flux density > 0.1 Jy at 5 GHz from GB6, or 3) flux density > 0.1 Jy at 5 GHz from PMN, or 4) flux density > 0.1 Jy at 3 GHz from VLASS.

II. Astrometric follow-ups:

46. Regular geodesy with VLBA (RDV), (Petrov et al. 2009); VLBA RV, RDV, BE010, BF012, BF025, BF090, BP138, BR005, BR025, BW008, BW025, CN18, CN19, RDGEO, RDS, RDV, RDWAPS, RDWPS, TC001, BR, TC, BW, RDG, WAP, CN18, CN19; dual X/S bands; 207 segments, since 1994.07.08 through 2023.04.25.
47. Dual X/S Astrometry Program, (Fey & Charlot 1997); VLBA BF025; dual X/S bands; 2 segments; since 1997.01.10 through 1997.01.11.
48. Investigation of residual systematic errors in dual-band linear combinations of delays caused by the ionosphere, (Petrov 2021); VLBA BP175; dual X/C-band; 10 segments; since 2013.10.26 through 2013.12.26. Selection criteria: 1) declination $> -40^\circ$ and 2) median correlated flux density > 0.2 Jy at 8.4 GHz at baseline projection lengths longer than 5000 km.
49. The second epoch VLBA Calibrator survey (VCS-II), (Gordon et al. 2016); VLBA BG219; dual X/S bands; 9 segments; since 2014.01.04 through 2015.03.17. Selection criterion: re-observations of the sources detected in VCS1, VCS2, VCS3, VCS4, VCS5.
50. VLBA Ecliptic Plane Survey (VEPS-V1), (Shu et al. 2017); VLBA BS250; dual X/S bands; 4 segments; since 2016.03.22 through 2016.05.19. Selection criterion: re-observations of the sources detected in the prior VLBI Ecliptic Band Survey with the CVN.
51. The third epoch VLBA Calibrator survey (VCS-III), (de Witt et al. 2021); VLBA UF001; dual X/S bands; 20 segments; since 2017.01.16 through 2017.10.21. Selection criterion: re-observations of the sources detected in VCS1, VCS2, VCS3, VCS4, VCS5.
52. Revealing milliarcsecond optical structure through VLBI observations of Gaia detected AGNs at Southern Hemisphere, PI: L. Petrov; LBA V561; dual X/S bands; 2 segments; since 2017.06.16 through 2018.03.14. Selection criteria: 1) detected in LCS-1 and LCS-2, and 2) declinations $< -45^\circ$, and 3) correlated flux density at 8 GHz within the range of $[0.07, 0.3]$ Jy, and 4) have a *Gaia* counterpart, and 4) no prior X/S VLBI observations.
53. SOuthern Astrometry Program (SOAP), PI: L. Petrov; LBA AUA, V515; dual X/S bands; 26 segments; since 2017.06.18 through 2019.12.04. Selection criteria: 1) declinations $< -45^\circ$, and 2) correlated flux density at 8.4 GHz from prior VLBI observations > 0.25 Jy, and 3) no prior X/S VLBI observations.
54. The fourth epoch VLBA Calibrator survey (VCS-IV), (de Witt et al. 2021); VLBA UG002; dual X/S bands; 24 segments; since 2018.01.18 through 2019.01.21. Selection criterion: re-observations of the sources detected in VCS1, VCS2, VCS3, VCS4, VCS5.
55. VLBA Ecliptic Plane Survey 2 (VEPS-3), PI: L. Petrov; CVN EPA; dual X/S bands; 2 segments; since 2018.01.24 through 2018.02.10. Selection criterion: re-observations of the sources detected in the prior VLBI Ecliptic Band Survey with the CVN.
56. VLBA Ecliptic Plane Survey 2 (VEPS-2), PI: F. Shu; VLBA BS264; dual X/S bands; 6 segments; since 2018.03.21 through 2018.06.15. Selection criterion: re-observations of the sources detected in the prior VLBI Ecliptic Band Survey with the CVN.

57. Probing milliarcsecond optical structure through VLBI observations of Gaia detected AGNs, PI: L. Petrov; VLBA BP222, BP236; dual X/S bands; 38 segments; since 2018.05.15 through 2020.04.19. Selection criterion: re-observations of the sources with large offsets between VLBI and Gaia positions and with low quality of their VLBI images.
58. The Asian VLBI Galactic Plane Survey, PI: L. Petrov; EAVN AP001A; K band; 4 segments; since 2018.10.09 through 2019.01.28. Selection criteria: 1) declinations $> -40^\circ$, and 2) Galactic plane defined as the region with galactic longitude $|l| < 15^\circ$ and galactic latitude $|b| < 12^\circ$ or $|l| > 15^\circ$, and 3) VLBI positional accuracy worse than 0.5 mas, and 4) correlated flux density at any band within 4 to 24 GHz, and 5) detected with Gaia, or 6) ecliptic latitude $|\beta| < 7.5^\circ$.
59. The fifth epoch VLBA Calibrator survey (VCS-V), (de Witt et al. 2021); VLBA UG003; dual X/S bands; 26 segments; since 2019.01.27 through 2020.08.09. Selection criterion: re-observations of the sources detected in VCS1, VCS2, VCS3, VCS4, VCS5.
60. The sixth epoch VLBA Calibrator survey (VCS-VI), (de Witt et al. 2021); VLBA UH007; dual X/S bands; 28 segments; since 2020.09.18 through 2022.12.12. Selection criterion: re-observations of the sources detected in VCS1, VCS2, VCS3, VCS4, VCS5.
61. Study of the population of steep-spectrum compact radio sources, XS part (VCS10); VLBA BP245; dual X/S bands; 6 segments; since 2020.03.02 through 2020.03.23. Selection criteria: 1) declination $> +75^\circ$, and 2) flux density > 0.2 Jy from NVSS, and 3) no detection or weak detection in the prior Norther Polar Cup Survey campaign.

III. High frequency extensions:

62. K/Q survey, (Lanyi et al. 2010; Charlot et al. 2010); VLBA BR079, BL115, BL122, BL151, BL166; X/K/Q bands; 14 segments; since 2002.05.15 through 2011.02.05. Selection criterion: sources with correlated flux density at 8 GHz brighter than 0.3 Jy.
63. K-band KVN calibrator survey, (Lee et al. 2017; Lee et al. 2023); KVN N13JL01, S14TJ05, S14JL01; K-band; 7 segments; since 2013.09.04 through 2014.12.24. Selection criterion: sources with flux density > 0.2 Jy at 22 GHz and not previously detected with VLBI.
64. Improving the K-band Celestial Reference Frame in the North, (de Witt et al. 2023); VLBA BJ083; K band; 5 segments; since 2015.07.21 through 2016.06.20 Selection criterion: sources that have been detected in prior 22 GHz VLBI surveys;
65. K-band EVN observations for geodesy and astrometry (Gomez et al. 2021); EVN EL054, EC076; K band; 2 segments; since 2016.06.15 through 2020.10.23
66. Improving the K-band Celestial Reference Frame in the North, (de Witt et al. 2023); VLBA UD001; K band; 24 segments; since 2017.01.08 through 2018.07.22. Selection criterion: sources that have been detected in prior 22 GHz VLBI surveys.
67. Improving the K-band Celestial Reference Frame in the North (the 2nd campaign), (de Witt et al. 2023); VLBA UD009; K band; 35 segments; since 2018.09.09 through 2021.06.12. Selection criterion: sources that have been detected in prior 22 GHz VLBI surveys.
68. Detection of the background position noise due to non-stationary of the Galactic gravitational field, PI: L. Petrov, KVN GAJI; K/Q bands; 5 segments; since 2018.09.25 through 2018.12.29. Selection criteria: 1) declinations $> -40^\circ$, and 2) galactic latitude $|b| < 1.5^\circ$, and 3) galactic longitude $|l| < 20^\circ$.
69. Asian K-band observations for geodesy and astrometry; PI: S. Xu; EAVN S20TJ, A20, A21, A22, A23; K band; 9 segments; since 2020.11.05 through 2013.06.08.
70. K- and Q-band VLBI Calibrators near the Galactic Center, PI: Y. Pihlstrom; VLBA BP251; K/Q bands; 2 segments; since 2021.03.19 through 2021.04.15. Selection criteria: 1) angular distance to the Galactic center less than 10° and 2) detected in prior K/Q observations with KVN.
71. Improving the K-band Celestial Reference Frame in the North (the 3rd campaign); PI: A. de Witt; VLBA UD015; K band; 18 segments; since 2021.07.26 through 2023.01.06. Selection criterion: sources that have been detected in prior 22 GHz VLBI surveys.

72. Further improving the K-band Celestial Reference Frame in the North (the 4th campaign); PI: A. de Witt; VLBA UD018; K band; 4 segments; since 2023.07.03 through 2023.07.24. Selection criterion: sources that have been detected in prior 22 GHz VLBI surveys.

Starting at 2013, pathfinder surveys switched to the upgraded wide C-band receiver at VLBA because of a low level of radio interference at the time and its high sensitivity. It covers 4–8 GHz, and we call such observations dual-band X/C. The dual-band X/S and X/C data were used in a joint dual-band solution in this work.

Table 20 presented in the Appendix shows the list of 72 observing campaigns that we processed. Most of the observations were made at the Very Long Baseline Array (VLBA), which covers the declinations $> -40^\circ$. Sources at declinations $< -40^\circ$ were observed with the Australian Long Baseline Array (LBA). We used also data, mainly at 22 and 43 GHz, from the European VLBI Network (EVN), the East Asian VLBI Network (EAVN), the Korean VLBI Network (KVN), and the VLBI Exploration in Radio Astronomy array (VERA).

2.2. Geodetic VLBI experiments

The International VLBI Service for geodesy and astrometry (IVS, Schlüter & Behrend 2007) coordinates observing programs dedicated to geodesy. These programs are similar to astrometric programs. The main differences are schedule optimization, antenna sensitivity, and source selection. There are two flavors of geodetic programs: 24 hr experiments that typically involve 8–10 stations (Thomas et al. 2024) and 1 hr experiments dedicated for determination of the Earth orientation parameter UT1 that typically run at a single baseline (Nothnagel et al. 1994; Sekido et al. 2008). There are ~ 250 regular 24 hr geodetic sessions per year, i.e. on average, a geodetic experiment runs every second day. The regular 1 hr observing sessions started on April 01, 1985. Their number gradually increased from 236 in 1988 to 860 in 2023, i.e. on average, more than two such experiments per day run since the 2020s.

Observing schedules of geodetic experiments are optimized to a determination of site positions and the Earth orientation parameters, which is almost orthogonal to optimization of astrometric programs. Antennas used in geodetic programs are less sensitive than those used in astronomy programs. The source list with rare exceptions is limited to 50–100 frequently observed bright objects. Positions of these sources are determined so well in astrometric experiments that additional observations have virtually no impact. There were attempts to include additional sources of interest to astrometry into schedules of geodetic experiments. Although it was demonstrated that it is possible to determine positions of several dozens of sources with a nanoradian level of accuracy (Le Bail et al. 2016), these observations are not competitive with respect to dedicated astrometric campaigns.

We used all publicly available geodetic experiments in our work in order to improve estimates of station positions and Earth orientation parameters. The high density of geodetic observations helps to stabilize the global VLBI solution and allows us to make it fully self-consistent without the use of any external geodetic or astrometric information.

2.3. Scheduling Observations

A VLBI schedule consists of a table with entries called scans that for each station defines the start time, slewing to a program source, the start time for recording baseband data that are the digitized voltage samples from a receiver, and the scan end time. Upon completion of one scan, an antenna executes another scan. A campaign design sets a goal to observe sources from a given list in given number of scans at at least the minimum number of stations with a given integration time per scan. If the number of scans per source is greater than one, additional requirements are set, such as the minimum time interval between observations of a given source or observing a source in the given minimum number of scans at the specified number of ranges at hour angle of the array reference antenna. Observing at different azimuths, elevations, and hour angles reduces systematic errors in estimates of source coordinates and improves the uv -coverage of program sources, which makes imaging more robust. Only a fraction of target sources in pathfinder surveys is detected at some baselines, and even a smaller fraction is detected at more than one half of the baselines. Therefore, in order to minimize losses of antenna time for observing sources that we cannot detect, pathfinder surveys observe target sources in one or two scans only.

A sequence of scans is generated with a specialized software. It consecutively computes for each program source (i) the number of antennas that see it above the physical horizon mask, (ii) slewing time, (iii) the likelihood that a given source can be visible at a given minimum number of stations in the future either during the current observing session or during the entire campaign, and (iv) the score that depends on all these factors. A scan with the highest score is selected for the schedule and the process is repeated. The algorithm for computing the final score is adjusted

in such a way that the maximum number of sources is included into the schedule that satisfy the campaign design criteria, and the overall slewing time is close to the minimum.

In addition to program sources, a schedule includes observations of known strong sources that are considered calibrators. A common practice is to include every hour observations of blocks of four strong sources selected in such a way that at each station at least one of them is observed at low elevations, for instance 10° – 30° , and one source is observed at high elevations, say 45° – 90° . The purpose of including calibrators in survey observations is fourfold: (1) these sources are used as fringe-finders for initialization of the correlation process; (2) these sources are used for computation of the complex bandpass calibration; (3) these sources are used for improving separation of variables when estimating residual atmospheric path delay; and (4) these sources are frequently observed in many other programs and therefore, provide a connection of coordinate estimates of the program sources with the core sources that define the orientation of the coordinate system. In general, 10 to 25% observing time is spent for observing calibrators. In addition, some telescope, like the Green Bank Telescope (GBT), require observing every 2–4 hours so-called pointing calibrators that are used for adjusting the pointing model. Phased VLA or ATCA require observing so-called phasing calibrators for adjusting phases of individual telescopes of the array in such a way that the phased arrays can be used for further processing as if it is a single telescope. High frequency surveys may require observations of planets for flux density calibration.

Optimization of the observing schedule takes into account campaign design goals, placement of calibrators, and other constraints. It is a fairly complicated task that is performed by a specialized software (Petrov 2021; Schartner & Böhm 2020; Schartner et al. 2021, see for more details). A campaign consists of segments that are scheduled separately and run at different days. The scheduling procedure keeps records which sources were observed in prior surveys. For pathfinder surveys that are designed to have one observation per source, a source is removed from the list after putting it into a schedule. In order to facilitate optimization, the input source list has more sources than a campaign can observe. The oversubscription rate is a modest, 2–30%, for follow-up surveys and large, a factor of 1.5 to 4, for pathfinder surveys. Because of that, the number of combinations of admissible observations that can fit a given time slot is very large. The scheduling process selects that combination of admissible scans that maximizes the metric of a given campaign, for instance, the total number of observed sources with a given minimum number of scans per source. A chance of a given source to be observed can be altered by assigning a weight to such a source that impacts the score calculation. This mechanism is used for fine-tuning the source selection process: the sources are split into several categories and their weights are assigned according to categories they belong.

For some survey campaigns segment durations are fixed, and observing schedules are prepared in advance, while most of pathfinder campaigns after 2010 with VLBA were scheduled dynamically. That means the array operator launches the schedule generation process by using a web form when the array has a gap between high priority programs that are more demanding to weather conditions and/or the required range of local sidereal time. The principal investigator of observing campaigns scheduled that way does not have direct control when and even whether a given source will be observed. But following that approach, more observing time can be allotted because otherwise, the array would have stayed idle.

3. DATA ANALYSIS

Radio telescopes synchronously track a sequence of radio sources. VLBI hardware records voltage from receivers sampled at several intermediate frequencies (IFs) at rates from 8 to 256 Mbps at 2 bits per IF. Each recording block with a typical size of 5–32 kB is called a frame, and it has metadata that includes time stamps from a local hydrogen maser. The first stage of data analysis is performed by a correlator that computes time series of cross- and auto-correlation spectra with a resolution in the range from 15.6 KHz to 2 MHz averaged over the correlator accumulation time that is in the range from 0.1 to 4 sec. The original raw VLBI data from radio telescopes are purged upon the initial quality control after correlation, since currently it is still not feasible to keep them because of their large volume. All astrometric voltage data reported here amount to 66 PB. Time averaging at the correlator reduces the output data volume to 146 TB. These data are kept at the data archives listed in the acknowledgment section indefinitely as a legacy of observing facilities. Three other stages of data processing are a) visibility analysis that takes the correlator output as an input, and computes phase, group delays and visibilities averaged over frequency and time; b) astrometric analysis that takes group delays as an input and adjusts for source coordinates and other nuisance parameters and flags for outliers; and c) imaging data analysis that uses the time and frequency-averaged visibilities, as well as flags

determined at the previous step and reconstructs source images. These steps are, in general, interdependent and at least one iteration is required between visibility analysis, astrometric analysis, and imaging.

3.1. Correlation

Data acquisition terminals at stations split the input radio frequency signal from radio telescope receivers into a number of subband channels called here intermediate frequencies (IFs) and write them into disks or tapes with time tags from H-masers. The original records of voltage are played back at an array operating centers, shifted according to the a priori model of path delay, correlated, and time averaged with either special hardware complex or software Mark-III, Mark-IV, S2, K3, K4, K5, VLBA, SFXC, Mitaka, KJCC, and DiFX (Deller et al. 2007, 2011). The correlator produces time series of auto- and cross- correlation of input data streams. These time series, augmented with auxiliary information, form a Level 1, or visibility, VLBI dataset.

Time averaging and frequency resolution affect the field of view of the interferometer. The higher spectral resolution within an IF and finer time averaging, the wider the field of view. Once the correlator setup is made for a given experiment, data are correlated, and the recording media with raw data is released, that choice is final, and it is not feasible to fix the correlator settings. Early hardware correlators were inflexible in setting spectral and time resolutions due to their architecture and they limited the output record rate. A common correlator setup provided a field of view of 5–20". If an a priori positional error was greater, time or frequency smearing would result in a reduction of interferometric signal. Newer software correlators do not have that limitation, and imaging of the entire prime beam of telescopes became feasible, although that feature is not frequently used.

3.2. Analysis of visibilities

Using visibility data, we evaluate residual phase and group delay, as well as their time derivatives. A given visibility, i.e. a constituent of the cross-spectrum averaged over a given interval of time called an accumulation period and a given spectral range can be presented as a complex number.

We treated observations that were used for absolute astrometry and for geodesy differently. We reprocessed all astrometric data at the visibility level using our software *PLMA* (Petrov et al. 2011a) that is a part of the Space Geodesy Data Analysis Software Suite³ (SGDASS), but only a portion of geodetic data. For the remaining geodetic datasets we used in our solution group delays computed by the IVS correlation centers.

Source positions were determined using not the complex visibility data v_{ij}^o but derived quantities, group delays τ_g :

$$v_{ij}^o = g_i S_c e^{-2\pi i(f_0(\tau_p^o - \tau_p^a) + (f_i - f_0)(\tau_g^o - \tau_g^a) + f_0(\dot{\tau}_p^o - \dot{\tau}_p^a)(t_j - t_0) + (f_i - f_0)(\dot{\tau}_g^o - \dot{\tau}_g^a)(t_j - t_0))}, \quad (1)$$

where g_i is antenna gain, S_c is correlated flux density, τ_p is phase delay, f_i is frequency of the i -th spectral channel, f_0 is the reference frequency, t_j is time of j -th accumulation period, and t_0 is the fringe reference time. Superscripts ‘o’ and ‘a’ denote observed and a priori delays and their rates, respectively. Quantities τ_p , τ_g , as well as their time derivatives, are evaluated in the fringe fitting procedure. The procedure of fringe fitting used in our work is described in detail in Petrov et al. (2011a) and Petrov (2021). We only outline it here while making an emphasis on computation of group delay uncertainties.

Since fringe visibility depends on path delay strongly nonlinearly, estimation of these quantities is performed in two steps. First, the sum of visibilities over all IFs, all spectral channels, and all accumulation periods is computed on a 2D grid of trial τ_g and $\dot{\tau}_p$, and the maximum is sought. The location of the maximum and its magnitude is found by a parabolic fit using the element at the 2D grid that provides the maximum and four adjacent elements. The group path delay and phase delay rate that correspond to the maximum are considered coarse estimates.

Then we compute the mean amplitude of $\sum \sum v_{ij}^o$ when no signal is present. We select randomly N elements at the 2D grid used for the coarse fringe search and put the sums of visibilities in an array. N is the minimum of 32768 and 1/4 of the total number of visibilities of a given observation. We sort this array in the ascending order, compute the mean and root mean square (rms), and run an iterative outlier elimination procedure. We remove an element with the maximum amplitude, recompute the average and rms, and repeat the procedure till the maximum element is less than 3.5 times of the rms. This procedure cleans the noise array from a possible contamination with a signal from

³ See <https://astrogeo.smce.nasa.gov/sgdass>

observed sources. The ratio of the amplitude of the maximum to the mean amplitude of noise we call a signal to noise ratio (SNR)⁴.

In order to get optimal estimate of group delay and phase delay rate, as well as their uncertainties, the visibility data were transformed to a form suitable for least square adjustment. The 2D array of visibilities of a given observation is split into segments with an SNR at each segment equal to approximately 1. We applied coarse estimates of group delays and phase delay rates denoted with superscript ‘c’ to segmented visibilities, i.e. we counter-rotated phases of visibilities averaged over a certain range of time and frequency that we call a segment:

$$v_{lm}^s = \sum_{i=a}^{i=b} \sum_{j=c}^{j=d} v_{ij}^o e^{2\pi i((f_i - f_0)(\tau_g^c - \tau_g^a) + f_0(\tau_p^c - \tau_p^a)(t_j - t_0))}. \quad (2)$$

The phases of segmented visibilities were used for consecutive data analysis. Based on the abovementioned estimates of the signal to noise ratios in segmented visibilities and assuming the real and image parts of the noise in the visibilities are independent *within the segment* and normally distributed, we computed uncertainties of visibility phases. These uncertainties are the base of the ladder of error propagation to source positions.

Then we used weighted least squares to find τ_g , τ_p , as well as their rates, using phases of segmented visibilities as observables and reciprocal phase uncertainties as initial weights. Visibility phases are considered uncorrelated. In general, systematic errors in the signal chain and in the propagation media affect visibility phases to a greater extent than visibility phases and therefore, uncertainties in segmented visibility phases computed on the basis of SNR in amplitudes are underestimated. In order to account for the contribution of these factors that increase the phase scatter within a scan, we adjust initial weights by adding in quadrature an extra variance, which is constant within a scan. That makes the ratio of the weighted sum of residuals to their mathematical expectation close to unity. This procedure to a greater extent affects observations with high SNR, say > 30 , and makes uncertainties less unrealistic. At the same time, the additive reweighting technique cannot fully account for the impact of the systematic errors affecting group delay estimates since visibility phases are still considered uncorrelated.

3.3. Analysis of group delays: dual-band, single-band, fused

Astrometric analysis of group delays involves two major steps: a) computation of theoretical path delays and forming small differences between the observed and theoretical delays called o-c, as well as computation of partial derivatives of o-c over parameters, b) preprocessing; and c) parameter estimation using o-c as a right-hand side. We used our software VTD for computation of path delay and software pSolve for astrometric analysis. They are components of SGDASS package.

Computation of group delay in general followed the so-called IERS Conventions (Petit & Luzum 2010), with a number of improvements. We mention here six of them. First, we applied site displacements for the atmospheric pressure loading, land water storage loading, tidal ocean loading, and non-tidal ocean loading on the observation level. The loading time series of 3D displacements were taken from the International Mass Loading Service (Petrov 2015a). Second, we computed displacements caused by solid Earth tides using rigorous equations (see Petrov & Ma 2003, for details). Third, we applied in data reduction a priori slant path delays computed by a direct integration of equations of wave propagation through the heterogeneous atmosphere (Petrov 2015b) using the output of NASA numerical weather model GEOS-FPIT (Rienecker et al. 2018). Fourth, we modeled the contribution of Galactic aberration rate to path delay. We used the distance to the Galactic center and the velocity of the Sun with respect to the Galactic center 8.34 kpc and 255.2 km/s respectively according to Reid et al. (2014). This gives us the acceleration toward the Galactic center $2.531 \cdot 10^{-10} \text{ m/s}^2$, which corresponds to the $5.49 \mu\text{as/yr}$ annual change of the Galactic aberration. Fifth, we applied the data reduction for parallax for known radio stars that have parallaxes determined with *Gaia* and published in the Early Data Release 3 (Lindgren et al. 2021) and for Sgr A* determined from dedicated differential VLBI observations (Oyama et al. 2024). Sixth, we included in our data reduction the ionospheric contribution computed from the GNSS global ionospheric model CODE (Schaer 1999) with important modifications: elevation for the ionospheric mapping function was scaled by 0.9782, the nominal height of the ionosphere was increased by 56.7 km, and the total electron content (TEC) was scaled by 0.85. A thorough discussion of the impact of these modifications is given in Petrov (2023).

⁴ One may define SNR as the ratio of the maximum to the rms amplitude of the noise. The SNR defined that way is $\sqrt{2/\pi}$ of the SNR according to our definition.

The contribution of the ionospheric path delay can be expanded into series of frequency. For accounting for path delay in the ionosphere, it is sufficient to retain only one term that is reciprocal to the square of the effective frequency. As it was shown by Hawarey et al. (2005), the impact of a higher order of expansion on the group delay, namely proportional to f^{-3} , does not exceed several picoseconds and is not detectable. The impact of the ionosphere on group delay is almost entirely eliminated if to observe simultaneously at two or more widely separated frequency bands. The following linear combination of two group delays at the upper and lower bands, τ_u and τ_l , respectively, is ionosphere free:

$$\tau_{\text{if}} = \frac{f_u^2}{f_u^2 - f_l^2} \tau_u - \frac{f_l^2}{f_u^2 - f_l^2} \tau_l. \quad (3)$$

Here f_u and f_l are effective ionospheric frequencies at the upper and lower bands, respectively. We do not apply the contribution of the ionosphere to group delay from the GNSS global ionospheric model when we process dual-band observations.

The downside of this approach is that the uncertainty of an ionosphere-free group delay is greater than uncertainties of τ_u and τ_l . For instance, when observations are made at 2.2 and 8.4 GHz and uncertainties of group delays at both bands are the same, the uncertainty of τ_{if} is increased by a factor of 1.08. When observations are made at 4.3/7.6 GHz, the uncertainty of the ionosphere free path delay is increased by a factor of 1.56. However, there are two cases when the ionosphere free path delays cannot be used.

First, an experiment can use only one band by design. In that case we apply the a priori contribution to group delay from the GNSS global ionospheric model. However, the model accounts only for a part of the contribution. In Petrov (2023) we performed a detailed study and evaluated the residual errors of the ionospheric contribution. We found that the rms of the residual errors σ_{rr} can be represented as the following regression through the scatter of total ionospheric path delay at a given baseline:

$$\sigma_{\text{rr}}(f, e) = \left(\frac{f_{8\text{GHz}}}{f} \right)^2 \sum_{k=-2}^{k=n-1} c_k B_k^3(\sigma(\tau_{\text{gt}})) \sqrt{M^2(e_1) + M^2(e_2)}. \quad (4)$$

Here f is the frequency in GHz, e is the elevation, $M(e)$ is the ionospheric mapping function that describes the elevation dependence of the ionospheric model, $B_k^3(x)$ is the B-spline function of the 3rd degree with the pivotal knot k , and $\sigma(\tau_{\text{gt}})$ is the rms of the total ionospheric path delay. For computation of $\sigma(\tau_{\text{gt}})$ we calculated the coordinates of 16384 points uniformly distributed over the celestial sphere using a random number generator. Then for each baseline and each time epoch of a given VLBI experiment, azimuth and elevation angles of those points, A_i , and e_i , are computed at both stations of the baseline. If elevations above the horizon are greater than 5° at both stations, that point is selected for further computations. If not, the next point is drawn. Then the total ionospheric path delay $\tau_i(A_1, e_1, A_2, e_2)$ is computed using the GNSS TEC maps. We normalize it by dividing by the mean mapping function $M = (M(e_1) + M(e_2))/2$. The process is repeated for 1440 time epochs that cover the time interval of a given VLBI experiment under consideration with a step of 1 minute. Then for each baseline we computed $\sigma(\tau_{\text{gt}})$ over this time series of 1440 normalized τ_i values. Validation of this regression model, as well as the values of numerical coefficients, can be found in Petrov (2023). The uncertainty of group delay $\sigma_{\text{rr}}(f, e)$ is added in quadrature to the uncertainty of group delay determined by the fringe fitting procedure.

As it was shown in Petrov (2023), the use of GNSS global ionospheric model to account for ionospheric path delay causes a declination-dependent bias in declination that can reach 0.4 mas at 8 GHz. The origin of this bias is an oversimplification of the dependence of the total electron content with height as a thin shell layer for computation of the GNSS ionospheric models.

Second, there are situations when fringes can be detected for a given observation only at one band in a dual-band VLBI experiment. Usually, only a small fraction of dual-band observations is affected: from 2 to 20%. For the remaining observations we compute the ionospheric path delay τ_i^v from VLBI group delay at the upper and lower frequency bands. We represent this ionospheric delay at stations j and k as:

$$\tau_i^v(t) = b_j(t) - b_k(t) + \frac{e^2}{8\pi^2 c m_e \epsilon_0 f_u^2} \left(\left(\text{TEC}_j(\phi_j, \lambda_j, t) + a_j(t) \right) M(e_j) - \left(\text{TEC}_k(\phi_k, \lambda_k, t) + a_k(t) \right) M(e_k) \right), \quad (5)$$

where TEC is the total electron content from the GNSS global ionosphere model, $b_j(t) = \sum_{i=1}^{i=n} b_{ij} B_i^0(t)$ is a delay bias expanded over the B-spline basis of the 0th degree, $a_j(t) = \sum_{i=-2}^{i=n-1} a_{ij} B_i^3(t)$ is the TEC bias expanded over the B-spline basis of the 3rd degree, ϕ, λ are coordinates of the ionosphere piercing point, which depend on positions of observing stations, as well as on azimuths and elevations of observed sources, e is the charge of the electron, m_e is the mass of the electron, ϵ_o is the permittivity of free space, and c is the velocity of light in vacuum. The clock bias has jumps at epochs of clock discontinuities. If clock had no jumps in a given experiment, b_j is a constant. The value $a_j(t)$ describes the time variable bias in the total electron content from the GNSS global ionospheric map.

We estimated coefficients a_{ij} and b_{ij} in a single weighted least squares run for each dual-band astrometric VLBI experiment. Weights were chosen to be reciprocal to the uncertainty of the ionospheric contribution from VLBI dual-band group delays with a floor 12 ps added in quadrature. The model in equation 5 is an approximation, and its use causes systematic errors. That floor was added to accommodate systematic errors of the model and avoid the dominance of few observations with small uncertainties in the solution. The B-spline knots for modeling a_{ij} were selected with spans equal to 900 s. Constraints on a_{ij} , its first and second time derivatives with reciprocal weights $5 \cdot 10^{-10}$ s, $4 \cdot 10^{-14}$, and $2 \cdot 10^{-18} s^{-1}$ respectively, were imposed in order to stabilize the solution when there are too few observations and to enforce the continuity of TEC bias evolution with time. Using estimates of a_{ij} and b_{ij} coefficients, we computed $\tau_i^m(t)$ following equation 5. Invoking the law of error propagation, we computed the full covariance matrix of a_{ij} and b_{ij} , and then using that full covariance matrix we computed the uncertainty of $\tau_i^m(t)$, scaled it by the empirical fudge factor of 0.889, and added in quadrature that uncertainty to the of group delay uncertainty. The empirical scaling factor of 0.889 was found by comparison of modeled $\tau_i^m(t)$ with observed $\tau_i^m(t)$ using a dataset of 4 million observations. The validation procedure for computation of $\tau_i^m(t)$ is described in full detail in Petrov (2023).

This approach allows us to treat dual-band and single-band data uniformly. When processing single-band delay experiments, we computed ionospheric path delays using the GNSS global ionospheric model, as well as their uncertainties, from the regression expression 4. When processing dual-band delay experiments, we used ionosphere-free linear combinations of group delays at lower and upper bands when observables at both bands were available. If observables only at one band were available, we computed the ionospheric contribution τ_i^m from coefficients a_{ij} and b_{ij} evaluated by processing dual-band data of that experiment, and computed the uncertainty of τ_i^m using the full covariance matrix. We call a dataset with a mixture of dual-band and single-band data of a given experiment ‘‘fused.’’ The summary of fused delay computation is presented in Table . This is a new technique. The validity of this approach hinges on the accuracy of τ_i^m and its uncertainty and on a lack of significant biases based on comparison of results from processing fused data when some dual-band data were artificially treated as single-band data against the reference solution. In our prior papers (Petrov 2023, 2024) we presented an in depth investigation of this approach and its validation.

Table 1. Summary of generation of fused observables and their uncertainties.

Available band		τ_{fused}	$\sigma^2(\tau_{\text{fused}})$
upper	lower		
yes	yes	$\kappa_1 \tau_u - \kappa_2 \tau_l$	$\kappa_1^2 \sigma^2(\tau_u) + \kappa_2^2 \sigma^2(\tau_l)$
yes	no	$\tau_u + \kappa_3 / f_u^2 ((TEC_1 + a_1) M(e_1) - (TEC_2 + a_2) M(e_2))$	$\sigma^2 \tau_u + \kappa_3^2 / f_u^4 (\sigma^2 a_1 M^2(e_1) + \sigma^2 a_2 M^2(e_2))$
no	yes	$\tau_l + \kappa_3 / f_l^2 ((TEC_1 + a_1) M(e_1) - (TEC_2 + a_2) M(e_2))$	$\sigma^2 \tau_l + \kappa_3^2 / f_l^4 (\sigma^2 a_1 M^2(e_1) + \sigma^2 a_2 M^2(e_2))$
no	no	not used	not applicable
only	—	$\tau_u + \kappa_3 / f_u^2 (TEC_1 M(e_1) - TEC_2 M(e_2))$	$\sigma^2 \tau_u + \sigma_{rr}^2(f_u)$

NOTE— The first four rows describe a case when fused data are generated from a dual-band experiment depending on which band data are available for a given observation. The fifth row describes a case of a single-band experiment. $\kappa_1 = \frac{f_u^2}{f_u^2 - f_l^2}$, $\kappa_2 =$

$$\frac{f_l^2}{f_u^2 - f_l^2}, \quad \kappa_3 = \frac{e^2}{8 \pi^2 c m_e \epsilon_o}$$

3.4. Parameter estimation

We estimated parameters in a single least squares run using a given dataset. The total number of estimated parameters exceeds 5 million in the fused solution. Inversion of a normal matrix of this size is possible through partitioning. We used three partitioning classes: global parameters that were estimated using the entire dataset, local parameters that were estimated for each observing session, and segmented parameters that were estimated for each station for an interval of time that is shorter than an observing session.

The parametric model included estimation of the following segmented parameters:

- clock function, except for the reference station;
- residual atmospheric path delay in zenith direction;
- the tilt of the symmetry axis of the refractivity field, also known as atmospheric gradients.

These parameters were modeled as an expansion over the B-spline basis of the 1st degree. The span between knots was 60 minutes for clock function, 20 minutes for the atmospheric path delay in zenith direction, and 6 hours for tilt angles.

The parametric model included estimation of the following local parameters:

- baseline-dependent clock;
- UT1, polar motion, and their time derivatives for experiments prior January 01, 1990.

Weak stabilizing constraints were imposed on UT1, polar motion, and their rates: $2.18 \cdot 10^{-7}$ rad and $2.53 \cdot 10^{-12}$ rad/s. These constraints allowed to process experiments that use a single baseline or experiments that had too few observations at some stations, or experiments that had only short baselines.

The parametric model included estimation of the following global parameters:

- Positions of all the stations at the reference epoch 2000.01.01.
- Linear velocities of all the stations.
- Antenna axis offsets of 104 stations.
- Sine and cosine components of harmonic site position variations at diurnal, semi-diurnal, annual, and semi-annual frequencies of 69 stations with a long history of observations. This technique is described in Petrov & Ma (2003) in detail. Estimation of harmonic variations allows to mitigate remaining systematic errors, for instance, the impact of thermal variations.
- B-spline coefficients that model the nonlinear motion of 29 stations. The nonlinear motion includes sudden co-seismic position changes at FORTORDS, GILCREEK, KASHIM11, KASHIM34, KOGANEI, MK-VLBA, MIURA, MOJAVE12, PRESIDIO, SINTOTU3, SOURDOGH, TATEYAMA, TIGOCONC, TSUKUB32, USUDA64, VERAMZSW, WARK12M, WHTHORSE, YAKATAGA, smooth post-seismic relaxation at GILCREEK, KASHIM11, KASHIM34, TIGOCONC, TSUKUB32, SINTOTU3, VERAMZSW, nonlinear change of the antenna tilt at PIETOWN, nonlinear uplift due to glaciers melting at NYALES20, nonlinear local motion of HRAS_085, and discontinuities due to station repair at DSS15, DSS65, EFLSBERG, GGAO7108, MEDICINA, SINTOTU3, TSUKUB32, URUMQI, and YEBES40M. The degree and placements of B-spline knots varied. Some knots were multiple to describe discontinuities in positions. The optimal placements of B-spline knots was determined by a trial. In order to assess the validity of the estimation model, we performed a residual solution where we used the estimates of the B-spline coefficients, as well as estimates of sine and cosine components of harmonic position variations as a priori. We estimated station positions for each experiment independently in the residual solution and examined time series of baseline lengths for the presence of residual discontinuities and non-linear motions.
- Coefficients of the empirical model of the perturbational Earth rotation vector $\mathbf{q}_e(t)$ with respect to the a priori model. In the framework of this formalism, a station vector in the co-rotating terrestrial coordinate system \mathbf{r}_T is related to a vector in the inertial celestial coordinate system \mathbf{r}_C from the a priori Earth rotation matrix $\mathcal{M}_a(t)$ and a small vector of the perturbational rotation $\mathbf{q}_e(t)$ as

$$\mathbf{r}_C = \widehat{\mathcal{M}}_a(t) \mathbf{r}_T + \mathbf{q}_e(t) \times \mathbf{r}_T. \quad (6)$$

We model vector $\mathbf{q}_e(t)$ in the terrestrial coordinate system as a sum of the coefficients of a B-spline that describe the slow constituents in the Earth rotation, coefficients of harmonic variations in the Earth rotation at periods 32 hours and shorter, and a cross-term $t \times \sin(t)$, $t \times \cos(t)$ for one harmonic:

$$\mathbf{q}_e(t) = \begin{pmatrix} \sum_{k=-2}^{n-1} e_{1k} B_k^3(t) + \sum_j^N (P_j^c \cos \omega_j t + P_j^s \sin \omega_j t) + t (S^c \cos -\Omega_n t + S^s \sin -\Omega_n t) \\ \sum_{k=-2}^{n-1} e_{2k} B_k^3(t) + \sum_{j=1}^N (P_j^c \sin \omega_j t - P_j^s \cos \omega_j t) + t (S^c \sin -\Omega_n t - S^s \cos -\Omega_n t) \\ \sum_{k=-2}^{n-1} e_{3k} B_k^3(t) + \sum_{j=1}^N (E_j^c \cos \omega_j t + E_j^s \sin \omega_j t) \end{pmatrix}, \quad (7)$$

where $B_k^m(t)$ is the B-spline function of degree m determined at a sequence of knots $t_{1-m}, t_{2-m}, \dots, t_0, t_1, \dots, t_k$; ω_j are the frequencies of external forces; the coefficients $e_{ik}, P_j^c, P_j^s, S^c, S^s, E_j^c, E_j^s$; are the parameters of the expansion; and Ω_n is the nominal frequency of the Earth's rotation. Here n is the dimension of the B-spline basis and N is the dimension of the Fourier basis.

We estimated harmonic variations at 877 frequencies. That included:

1. all the frequencies with nutation amplitude exceeding 10 prad from the REN2000 rigid Earth nutation series (Souchay & Kinoshita 1996, 1997; Souchay et al. 1999) to model nutation (q_1 , and q_2 only);
2. all harmonics of the tide generating potential (Hartmann & Wenzel 1995) with amplitudes greater than 0.002 of the M_2 tide amplitude to model all tidal variations in polar motion and UT1, except zonal tides;
3. 31 frequencies in the range of $-7.31149 \cdot 10^{-5}$ to $-7.29622 \cdot 10^{-5}$ rad/s with a step of $f_s = 2\pi/\Delta t = 4.9273 \cdot 10^{-9}$ rad/s to model the retrograde free core nutation (q_1 , and q_2 only), where Δt is the interval of time for estimation of harmonic variations in the Earth orientation parameters, 40.7 years;
4. 19 frequencies in the range of $-7.28370 \cdot 10^{-5}$ to $-7.27385 \cdot 10^{-5}$ rad/s with a step of f_s rad/s to model the prograde free inner core nutation (q_1 , and q_2 only);
5. 47 frequencies in the range of $-2.188774 \cdot 10^{-5}$ to $-2.188774 \cdot 10^{-5}$ rad/s, as well as $2.188774 \cdot 10^{-5}$ to $2.188774 \cdot 10^{-5}$ rad/s with a step of f_s to model prograde and retrograde variations within the ter-diurnal frequency band with a broadened spectrum due to seasonal modulations;
6. 47 frequencies in the range of $-2.915706 \cdot 10^{-5}$ to $-2.917986 \cdot 10^{-5}$ rad/s, as well as $2.915706 \cdot 10^{-5}$ to $2.917986 \cdot 10^{-5}$ rad/s with a step of f_s to model prograde and retrograde variations within the quad-diurnal frequency band with a broadened spectrum due to seasonal modulations.

The knot sequence of the B-spline basis used for modeling $\mathbf{q}_e(t)$ spanned time interval January 01, 1990 through September 05, 2024 with a step of 2 days. This technique is described in full detail in Petrov (2007).

- Positions of all the sources with at least three usable observations.
- Proper motions of Galactic sources that had a least two epochs: radio stars and Sgr A*. The reference epoch for source positions of these sources was 2016.01.01.

This parameter estimation model allowed us to adjust all parameters in a single least squares run. We used all VLBI data: 24 hr astrometric experiments, 3–8 hr survey style astrometric experiments, 24 hr geodetic experiments, and 1-hr so-called intensive experiments dedicated to estimation of UT1. These experiments were optimized for different goals. Many astrometric experiments, especially surveys, are not well suitable for estimation of the Earth orientation parameters and station positions. Treating these parameters as local, i.e. estimating them in each experiment, as it was often made in the past (see, for example, Diamantidis & Haas 2023), causes solution instabilities due to the cross-talk between radio source positions and the Earth orientation parameters. This adds a jitter in source position estimates.

Using the a priori nonlinear motion and the Earth orientation parameter series from external results that are regarded reputable in the geodetic community, opens a door for propagation of errors from these results to our solution. For

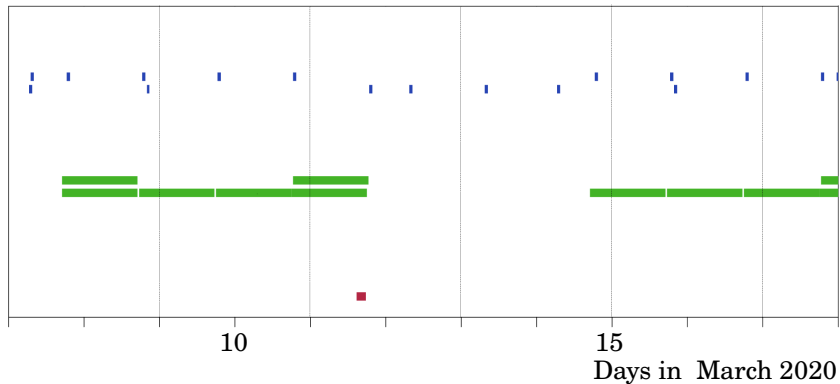


Figure 1. Time allocation for VLBI experiments for 10 days in March 2020. Upper (blue): 1-hr IVS Intensive experiments. Middle (green): 24-hr IVS geodetic experiments. Bottom (red): an astrometric experiment. Thin vertical lines correspond to epochs of B-spline knots.

instance, the ITRF2020 solution endorsed by the International Union of Geodesy and Geophysics that recommends its use as a standard, does not model the nonlinear motion of VLBA radio telescope PIETOWN that was known for decades (Petrov et al. 2009). Omission of peculiar motion of PIETOWN causes noticeable errors in source positions. Our careful analysis reveals noticeable errors in IERS time series of the Earth orientation parameters in 1997–2000. In addition to errors in the external solutions that can be identified during quality control, the use of external solutions introduces biases due to model inconsistencies. For instance, the IERS time series is the smoothed weighted mean of solutions from different analysis centers that either use different mass loading models or do not use them at all.

Estimating B-spline coefficients directly using all the observations, we have implemented an assimilation scheme. The B-spline of the 3rd degree is sensitive to data within three span intervals before and after a given epoch, i.e. within an interval of 14 days. All data, astrometric, 24 hr geodetic, and 1 hr geodetic contribute to estimates of the Earth rotation. As we can see in Figure 1, the density of geodetic data is high, and there is a number of overlaps. The density of geodetic data was low in the 1980s, which is not always sufficient for the use of the assimilation scheme. Therefore, we started B-spline in 1990.01.01 and estimated the Earth orientation parameters in the old-fashioned geodetic style as local parameters prior that date. Data prior to 1990 have a negligible direct impact on source position estimates. We included data since 1984.01.04, when geodetic VLBI observations became regular to make estimates of station positions more stable.

Estimating harmonic variations in the Earth orientation parameters, we eliminated the need to adjust nutation daily offsets introduced by Herring et al. (1986) as a temporary measure for processing datasets that were shorter than the 18.6 year principle nutation term. The retrograde free core nutation and putative prograde inner core free nutation are not harmonic processes, but we assume they are band-limited. To account for their contribution, we just sampled them within their bands at the Nyquist frequency $2\pi/T$, where T is the total interval of observations, 40.7 years. Thus, instead of estimating the time series of free core nutation, we directly estimated their spectrum, together with known spectral constituents of forced nutations, variations in the Earth rotation caused by ocean tides and other ad hoc harmonic processes.

3.5. Constraints used in the solution

We used constraints of three types in our solutions: identifying constraints that eliminate a degeneracy in observation equations, decorrelation constraints that substantially reduce correlations between parameters, and weak constraints that stabilize estimation of some parameters when there are not enough data to provide a reliable estimate. Constraints are equations that do not originate from observations: they augment them. The choice of constraints and their weights is up to some degree subjective. Since results depend on constraints, we disclose below all constraints that we have imposed in full.

3.5.1. Identifying constraints

The equation for path delay τ of a two element interferometer with stations \mathbf{r}_1 and \mathbf{r}_2 in the terrestrial coordinate system observing a source with a unit vector \mathbf{s} in the inertial celestial coordinate system can be simplified to a from:

$$\tau = \frac{1}{c} \widehat{\mathcal{E}}(\mathbf{r}_1 - \mathbf{r}_2) \cdot \mathbf{s} + O(c^{-2}), \quad (8)$$

where $\widehat{\mathcal{E}}$ is the Earth rotation matrix. We can see immediately that equation 8 is invariant with respect to a translation of the coordinate system, as well as to its time derivatives. Rotating the terrestrial coordinate system by matrix $\widehat{\mathcal{P}}_t$ is equivalent to a replacement of the Earth rotation matrix $\widehat{\mathcal{E}}$ with $\widehat{\mathcal{E}}\widehat{\mathcal{P}}_t^\top$. Therefore, path delay is invariant with respect to a rotation of the terrestrial coordinate system and its time derivative. Rotating the celestial coordinate system by matrix $\widehat{\mathcal{P}}_s$ is equivalent to a replacement of the Earth rotation matrix $\widehat{\mathcal{E}}$ with $\widehat{\mathcal{P}}_s^\top \widehat{\mathcal{E}}$. Therefore, path delay is invariant with respect to a rotation of the celestial coordinate system. When we estimate positions of all the stations, velocities of all the station, and coordinates of all the sources, there are five invariant conditions with 15 degrees of freedom. Observations themselves does not provide enough data and cannot provide them in principle to determine a unique solution. In order to invert the normal matrix, we have to augment the system of equations with 15 constraint equations that identify the solutions. These constraints make the rank of the system of equations equal to the number of parameters. Using the same logic, we conclude that the specific choice of identifying constraints that makes the system of equations invertible is not important, since any choice satisfies observations in exactly the same way.

We formulated identifying constraint by requiring that the net translation of station positions, net translation of station velocities, the mean of the Earth orientation parameters, their rate of change, and the net rotation of source positions be equal to some right-hand side vector that is not necessarily zero.

Constraint equations in a general form can be written as

$$C(x_e - x_r) = R, \quad (9)$$

where C is a matrix of constraint equations, x_e is the vector of estimates of constrained parameters, x_r is the vector of reference values of those parameters, and R is the vector of the rand-hand side constraint equations.

We specified the translational constraints of a coordinate system in a form that requires the unweighted net translation in positions and net translation of velocities of 27 stations with respect to the reference catalogue ITRF2000 (Altamimi et al. 2002) be zero. General equation 9 is reduced to:

$$\sum_i^n \Delta x_{ei}^j = \sum_i^n x_{ri}^j - \Delta x_{ai}^j, \quad (10)$$

where $\Delta x_e = x_a - x_e$, index i runs over stations, superscript j runs over 3 components of station positions and three components of station velocities, and indices a , r , and e denote vectors of a priori, reference, and estimates, respectively. The reciprocal constraint weights are 0.1 mm for station positions and 0.1 mm/yr for station velocities.

We specified the rotational constraints of the coordinate system in a form that requires the unweighted differences in estimates of the Euler angles describing the Earth rotation $E_e(t)$ with respect to the time series IERS C04 E_e to have no bias and no linear trend over [2000.0, 2024.0] time interval. The general equation 9 is reduced to:

$$\begin{aligned} \sum_i^N E_{ei}^j - E_{ri}^j &= 0 \\ \sum_i^N (E_{ei}^j - E_{ri}^j)(t - t_0) &= 0, \end{aligned} \quad (11)$$

where E_{ei}^j is the estimate of the j th component of the Euler angle at i th epoch and E_{ri}^j is that Euler angle from the reference time series. Summation is performed over N epochs within the interval [2000.0, 2024.0], which is narrower than the total interval of the EOP estimation with the B-splines. Then these equations are transformed to:

$$\begin{aligned} \sum_i^N \Delta E_{ea}^j &= \Phi^j \\ \sum_i^N \Delta E_{ea}^j &= \dot{\Phi}^j(t - t_0), \end{aligned} \quad (12)$$

where $\Delta E_{ea}^j = E_{ei}^j - E_{ai}^j$, Φ^j and $\dot{\Phi}^j$ are the mean value and linear trend in differences $E_{ri}^j - E_{ai}^j$. These equations are transformed to

$$\begin{aligned} \sum_{k=1}^{k=N} \sum_{i=1-m}^{i=n-1} e_{ji} B_i^m(t_k) &= \Phi^j N + \dot{\Phi}^j \sum_{k=1}^{k=N} (t_k - t_0) \\ \sum_{k=1}^{k=N} \sum_{i=1-m}^{i=n-1} e_{ji} B_i^m(t_k) (t_k - t_0) &= \Phi_i \sum_{k=1}^{k=N} (t_k - t_0) + \dot{\Phi}^j \sum_{k=1}^{k=N} (t_k - t_0)^2, \end{aligned} \quad (13)$$

where e_{ji} are B-spline coefficients for the j th component of the Euler angle and i th time epoch. The reciprocal constraint weights are $7 \cdot 10^{-9}$ rad on the mean value and $3 \cdot 10^{-17}$ rad/s on the linear trend.

We impose identifying constraints on source positions in a form that requires the net rotation of estimated positions \mathbf{s}_e of the subset of 212 sources with respect to the ICRF1 catalogue (Ma et al. 1998) denoted as \mathbf{s}_r be zero, i.e. $\sum_i^N \mathbf{s}_{ei} \times \mathbf{s}_{ri} = 0$. These conditions expressed via $\Delta \mathbf{s} = \mathbf{s}_e - \mathbf{s}_a$ lead to

$$\sum_i^N \Delta \mathbf{s}_i \times \mathbf{s}_{ri} = \sum_i^N (\mathbf{s}_{ri} - \mathbf{s}_{ai}). \quad (14)$$

This equations can be easily expanded for components in right ascensions and declination:

$$\begin{cases} \sum_i^N -\cos \alpha_{ri} \operatorname{tg} \delta_{ri} \Delta \alpha_{ri} + \sin \alpha_{ri} \Delta \delta_{ri} = \sum_i^N -\cos \alpha_{ri} \operatorname{tg} \delta_{ri} (\alpha_{ai} - \alpha_{ri}) + \sin \alpha_{ri} (\delta_{ai} - \delta_{ri}) \\ \sum_i^N -\sin \alpha_{ri} \operatorname{tg} \delta_{ri} \Delta \alpha_{ri} - \cos \alpha_{ri} \Delta \delta_{ri} = \sum_i^N -\sin \alpha_{ri} \operatorname{tg} \delta_{ri} (\alpha_{ai} - \alpha_{ri}) - \cos \alpha_{ri} (\delta_{ai} - \delta_{ri}) \\ \sum_i^N \Delta \alpha_{ri} = \sum_i^N (\alpha_{ai} - \alpha_{ri}) \end{cases} \quad (15)$$

The reciprocal constraint weights are $1 \cdot 10^{-10}$ rad.

These identifying conditions with the associated reference catalogues, list of objects, and weights (unity in our case) unambiguously define the origin and orientation of the catalogues of station positions and source coordinates. We should stress that the choice of identifying conditions is a matter of convention in a similar way as the Greenwich meridian is used as a fiducial reference for longitude. We used relatively old catalogues ITRF2000 (Altamimi et al. 2002) and ICRF1 (Ma et al. 1998), despite the positions of individual objects are not the best because we think it is important to provide the continuity in the convention.

3.5.2. Decorrelation constraints

Some combinations of estimated parameters are not exactly linearly dependent, but close to that. Their estimation makes the system of equations ill-conditioned and causes correlations between some groups of parameters be very close to ± 1 . To overcome these problem, we impose decorrelation constraints. They include the following.

- Constraints between the constituents of the harmonic expansion of the Earth orientation parameters with a frequency separation less than $0.8 f_s = 3.941 \cdot 10^{-9}$ rad/s. We require that the ratio of the complex amplitudes of estimated parameters P be the same as the ratio of the a priori complex amplitudes A :

$$\frac{P_1^c + iP_1^s}{P_2^c + iP_2^s} = \frac{A_1^c + iA_1^s}{A_2^c + iA_2^s}, \quad (16)$$

where index 1 denotes the main components of the spectra that correspond to nutations and tidal variations and index 2 denotes the secondary close component. In this context the constituents that have a frequency separation between each other $> 0.8 f_s$ are called primary. The reciprocal constraint weights are $3 \cdot 10^{-11}$ rad.

- Net-translation constraints on sine and cosine components of station position variations at each frequency:

$$\begin{aligned}\sum x_{ei}^c &= 0, \\ \sum x_{ei}^s &= 0,\end{aligned}\tag{17}$$

where the superscript runs over cosine and sine components and the subscript i runs over four frequencies. These parameters are considered nuisance in the context of this work. We should note that since we estimate harmonic position variations of only a subset of stations, this does not lead to the singularity of the normal matrix, but makes it ill-conditioned. The reciprocal constraint weights are 0.3 mm.

- Net-rotation constraints on sine and cosine components of station position variations at each frequency:

$$\begin{aligned}\sum X_a \times x_{ei}^c &= 0, \\ \sum X_a \times x_{ei}^s &= 0,\end{aligned}\tag{18}$$

where X_a is a vector of a priori site positions. The reciprocal constraint weights are 0.3 mm.

- Decorrelation between station position at the reference epoch and the B-spline model of the station position evolution. B-spline of the degree 0 and greater is linearly dependent with station position estimates. We require that the integral of the B-spline model over the interval of observations be zero:

$$\int_{t_0}^{t_n} \sum_{k=1-m}^{k=n-1} x_{ik} B_k^m(t) dt = 0,\tag{19}$$

where x_{ik} is the B-spline coefficient at the k -th knot of the i th station position component, which is reduced to:

$$\sum_{k=1-m}^{k=n-1} x_{ik} I_k^m(t) = 0,\tag{20}$$

where $I_k^m(t) = \int_0^t B_k^m(t) dt$. The reciprocal constraint weights are 0.3 mm.

- Decorrelation between station velocity and the B-spline model of station position evolution when the B-spline degree is > 0 . B-spline of the degree 1 and greater is linearly dependent with station velocity estimates. We require that the momentum integral of the B-spline model over the interval of observations be zero:

$$\int_{t_0}^{t_n} \sum_{k=1-m}^{k=n-1} x_{ik} t B_k^m(t) dt = 0.\tag{21}$$

This is reduced to

$$\sum_{k=1-m}^{k=n-1} x_{ik} K_k^m(t) = 0,\tag{22}$$

where $K_k^m(t) = \int_0^t t B_k^m(t) dt$. We should note there exist recurrent relationships for computation of functions $I_k^m(t)$ and $K_k^m(t)$ analogous to computation of B-spline functions themselves. The reciprocal constraint weights are 0.3 mm/yr.

- Tie velocities. We constraint the differences in velocity estimates at stations that are located within 0.03–2 km because they are the subject of the same tectonic motions. Constraints on the i th component of velocities of stations X and Y are imposed in this form:

$$\dot{X}_i - \dot{Y}_i = 0.\tag{23}$$

The reciprocal constraint weights are 0.3 mm/yr.

3.5.3. *Weak constraints*

There are situations when there are no sufficient data to get realistic estimates of some parameters. Imposing weak constraints allows us to stabilize the solution by expense of causing biases of estimated parameters towards the a priori values. We imposed the following weak constraints.

- Weak constraints on time derivative of clock function to process data with gaps and to make estimates smoother. Default reciprocal constraint weights: $2 \cdot 10^{-14}$. The reciprocal constraint weights were increased in rare cases when clock function had large variations (> 500 ps) due to hardware malfunctioning.
- Weak constraints on time derivative of atmospheric path delay in the zenith direction. The reciprocal constraint weights are $1.39 \cdot 10^{-14}$.
- Weak constraints on time derivative of tilts of the refractivity field symmetry axis. The reciprocal constraint weights are $7.72 \cdot 10^{-17} \text{ s}^{-1}$.
- Weak constraint on the second derivative of B-spline that models nonlinear station position evolution. The reciprocal constraint weights are 1 mm/yr^2 .
- Weak constraints on the Earth orientation parameters modeled with B-spline, its first, and second time derivative. This allows to stabilize the Earth orientation parameter estimates in the periods of time that cover gaps in observations, usually due to public holidays. Imposing constraints on the second time derivatives makes the time series smoother. The reciprocal constraint weights are $2 \cdot 10^{-6} \text{ rad}$, $3 \cdot 10^{-14} \text{ rad/s}$, and $1 \cdot 10^{-19} \text{ rad/s}^2$ for the value and the first and second derivatives, respectively.
- Weak constraints on the Earth orientation parameters and their rate models as local parameters in the range of 1980–1990. Imposing weak constraints allows to process single-baseline data and data at short baselines. The reciprocal constraint weights are $2.18 \cdot 10^{-7} \text{ rad}$ for Earth orientation parameters and $2.53 \cdot 10^{-12}$ on their rate of changes.
- Constraints on estimates of velocities of 49 stations. This allows to process data with a short history of observations. The reciprocal weights are 0.1 mm/yr for the vertical components and 3.0 mm/yr for the horizontal component. Strictly speaking these constraint are not weak.

3.6. *Filtering data for outliers*

A VLBI dataset of a given experiment may have from 5 to 80% outliers, i.e. observations with group delay errors much greater than reported uncertainties. The most common reasons of such errors are a) failures in the fringe fitting procedure because of insufficient baseline sensitivity; b) failures in the fringe fitting procedure because of poor phase calibration; c) failures in the fringe fitting procedure due to radio interference; d) scattering in the ionosphere or in rare cases in the solar corona; e) malfunctioning of either a Hydrogen maser or a maser signal distributor. In addition, some observations may have excessive residuals due to deficiencies of the model of radio wave propagation in the atmosphere, especially when observing at elevations below 20° or because of unaccounted source structure. It is essential that these outliers are identified and excluded from the final data analysis during the preprocessing part of the analysis.

The fringe fitting process provides an estimate of group delay even in the absence of the contribution of a signal from the observed source in visibility data. However, when the fringe fitting procedure is applied to the noise without a signal, the amplitude of the best fit is low. The distribution of the amplitudes weakly depends on the frequency and time resolution of visibility data, and therefore, varies within 10–30% from a campaign to campaign. The distribution density of the SNR has two components: from the noise and from the signal of the target sources (see Figure 9 in Petrov 2021). The first component vanishes at the $\text{SNR} > 5.5\text{--}7.0$. Fitting the first component, we can separate them and compute the probability of false detection.

At the beginning, we compute the distribution density of fringe amplitudes and determine the SNR when the probability of false detection is less than 0.001, 0.01, and 0.1. We process a given experiment with suppressing observations with the SNR cutoff that corresponds to the probability of false detection 0.001. Then we run a preliminary solution estimating station clock function, atmospheric path delay in zenith direction, polar motion, and UT1, as well as positions of some sources. Initially, we apply weights that are reciprocal to group delay uncertainty determined by fringe fitting. Then we run the procedure of outlier elimination and reweighing.

The presence of outliers distorts the solution and the residuals. To overcome this difficulty, we implemented the following iterative outlier elimination procedure with five steps:

1. Computation of postfit residuals and normalizing them by multiplying by the weight.
2. Sorting the normalized residuals.
3. Flagging the observations with the highest by modulo residual.
4. Update of the vector of estimate \mathbf{x} for exclusion of the flagged observation with index k . Invoking the lemma of the inversion of an extended matrix, also known as Sherman-Morrison lemma, this can be done on the basis of the prior least squares solution:

$$\mathbf{x}_u = \mathbf{x} - \hat{V} \mathbf{a}_k w_k \frac{y_k - \mathbf{a}_k \cdot \mathbf{x}}{1 + w_k \mathbf{a}_k^\top \hat{V} \mathbf{a}_k}, \quad (24)$$

where \mathbf{a}_k is the equation of observation, w_k is weight, and \hat{V} is the covariance matrix of the estimate vector \mathbf{x} .

5. Update of the covariance matrix for exclusion of the flagged observation

$$\hat{V}_u = \hat{V} + \frac{\hat{V} \mathbf{a}_k w_k \mathbf{a}_k^\top \hat{V}}{1 + w_k \mathbf{a}_k^\top \hat{V} \mathbf{a}_k}. \quad (25)$$

The procedure is repeated, until the maximum by modulo of a normalized residual exceeds the specified limit.

The procedure can be reversed and we can update the estimate vector and its covariance matrix from the least squares solution when we include observation r that has been previously excluded by changing a sign after \mathbf{x} in equation 24 and after V in equation 25. If we have more than one excluded observation, we find among them the observation with the smallest by modulo normalized residual considered. We call that reversed procedure data restoration. Some observations can be considered ineligible for restoration, for instance, because their SNRs are less than the threshold or phase calibration data were missing.

Processing pathfinder astrometric experiments poses an additional complication. When these experiments include observations of sources never before observed with VLBI, their positional errors may reach arcminutes. We have to estimate their coordinates. Estimation of positions affects robustness of the outlier elimination process. According to our experience, the following situation happens with the probability of 5–20%: only two observations of a given source remained at the end of the outlier elimination process, and only one of them is the outlier. When we estimate right ascension and declination using two observations, the residual is zero and the observations look good. We single out sources with estimated positions that have only two good observations and two or more outliers. We check for other combinations of flags for a given source in a given experiment using the brute force approach starting with short baselines first. This procedure has a chance of 20–30% to end up with a combination of flags that restores three or more observations and provides the normalized residuals less than 4, and thus, fixes the failure of the outlier elimination procedure.

Another complication emerges in processing double sources with a component separation greater than ~ 100 mas and with a ratio of flux densities less than 3–5. The fringe fitting process may catch different components of a source at different baselines. These sources are singled out as objects with an excessive outlier rate among observations with the probability of false detection < 0.01 . In that case we inverse the suppression flags for observations of these sources and repeat the outlier elimination procedure. This procedure may have two outcomes: (1) only two observations will remain and (2) three or more observations will remain. In the first case we discard results of this procedure. In the second case we further examine results by running the imaging process if the difference in positions of that source is less than $1''$ or examine Very VLA images from the archive, when available. If images confirm the presence of the second component close to the derived positions, we assign a new pointer to the visibility data and treat the dataset of these observations as having two or more sources in the field of view. We rerun the procedure of visibility data analysis from the very beginning. We fix positions of two or more sources in the field of view to the values determined in the previous round of data analysis during the first run of the outlier elimination, then estimate positions of these sources or source components, and then run one more iteration of restoration of observations and outlier elimination. In rare cases when we cannot confirm the second component in images, we keep questionable observations suppressed.

We performed the outlier elimination for each fused, dual-band, and single-band observables independently and kept flags and reweighting parameters q_b separately for each combination of group delays. Upon completion, we re-run the fringe fitting for eligible outliers with the narrow group delay window, 0.7–2.0 ns depending on band. Observations of sources that had fewer than three usable observations or with failed phase calibration are considered ineligible. Then we repeat the procedure of outlier elimination using the flags that were set in the prior analysis. This round restores a fraction of previously eliminated observations, from 10 to 80%.

Sources with two or fewer usable observations at a given pathfinder session but with more than three or more usable observations among all the observing sessions were additionally checked. We ran a preliminary global solution using all the sessions, estimated positions of these sources, and examined residuals. Then we performed the outlier elimination procedure for these sources, but using a whole dataset. All observations of those sources that had fewer than three unflagged observations in a global dataset were not used in the final solution. Three observations per source provide a minimum redundancy. A failure of the fringe fitting or the radio interference distorts group delays. Fitting right ascension and declination to one or two observations will result in zero residuals, regardless whether group delays were correct or not, while fitting to three or more observations will cause large residuals if one of the group delays was wrong, and examining residuals will allow us to detect an anomaly. Thus, this redundancy provides a safeguard against contamination of the output catalogue by spurious results.

Finally, in order to mitigate subjectivity, the outlier elimination procedure that uses prior results as an initial guess is executed in the fully automatic mode once again.

3.7. Weight update

In addition to outlier elimination, we ran the weight update procedure. First, we added in quadrature the elevation-dependent weights in the form of $\beta * \sqrt{\tau_{w1}^2 + \tau_{w2}^2}$, where τ_{wi} is the wet path delay in the direction of the observed source at the i -th station and β is a scaling factor. We used $\beta = 0.1$ in our work. As a trial, we ran a set of geodetic solutions when we estimated station positions from each experiment individually. We got a time series of baseline lengths, fitted the linear model with discontinuities due to seismic events at some stations, and computed the rms of the residuals to that model, the so-called baseline length repeatability. We repeated these trial solutions with different β and found that $\beta = 0.1$ resulted to the smallest repeatabilities for most of baselines. The use of this reweighting scheme accounts for errors in modeling path delay as a sum of the a priori path delay derived from numerical weather models, adjusted corrections to the zenith path delays, and adjusted tilts of the refractivity field symmetry axis. Considering that the wet constituent of the zenith path delay averaged over all experiments and all stations is 371 ps, the added elevation-dependent noise was on average 52 ps when the source was in zenith at both stations and 260 ps when the source was at 10° elevation.

We compute the ratio of the sum of weighted residuals R and its mathematical expectation $\mathcal{E}(R)$ using the following approximation:

$$\mathcal{E}(R) = n - \left(m - \text{Sp}(\hat{V} \hat{B}^\top \beta^{-1} \hat{B}) \right), \quad (26)$$

where n is the number of observations, m is the number of equations, \hat{V} is a covariance matrix of estimates, \hat{B} is a matrix of constraints, and β is a matrix of constraint weights, and Sp denotes a matrix trace. When no constraints are imposed, eq. 26 is reduced to $n - m$, also known as the number of degrees of freedom (ndf). Analysis of statistics showed that adding the elevation-dependent noise is insufficient to make $\mathcal{E}(R)$ close to unity.

If the used weights were reciprocal to the true uncertainties of observations and correlations between observations were zero, this ratio would have been one. Usually, this ratio is greater than one. Using an estimate of R , we can improve weights under two assumptions: a) observations are not correlated and b) there is another unknown independent source of errors in group delays with the zero mean and unknown baseline-dependent variance, i.e. the used weights are $1/w^2 = \sigma^2 - q_b^2$. Then after some algebra we arrive to the estimate of q parameter for a given baseline b :

$$q_b = \sqrt{\frac{\mathcal{E}(R_i) - \left(n_b - \text{Sp}(V A^\top W_i^{-1} A) \right)}{\text{Sp}(W_b^{-1}) - \text{Sp}(V A^\top W_i^{-2} A)}}, \quad (27)$$

where W is the a priori weight matrix and index n_b is the number of equations used in the solution at a given baseline b .

Cleaning the dataset involves several cycles. First, we discard observations with an SNR less than a quantity which corresponds to the probability of false detection of 0.001. We execute the sequence: 1) outlier elimination at a given maximum by modulo normalized residual N_σ ; 2) weight update, and 3) outlier elimination. Observations with an SNR less than the threshold are barred from restoration. We start with $N_\sigma = 8$, then reduce it to 6, 5, and 4. Then we gradually reduced the threshold of the probability of false detection to 0.01, 0.1, and finally to 0.2. Those observations that we discarded in the previous cycle because of their SNR are automatically flagged as outliers, but become eligible for restoration.

Although we raised the threshold of false association to 0.2 in the filter, that does not mean that the final dataset has 1/5 spurious group delays. The weight root mean square of residuals (wrms) of detected observations is in range of 20 to 100 ps for astrometric experiments and the residuals have a distribution that is close to Gaussian. Nondetections have a uniform distribution within a search window that ranges from ± 1 to $\pm 16 \mu s$. In a typical case when the wrms of postfit residuals is 50 ps and the fringe search window is $\pm 2 \mu s$, the probability of that a nondetection will pass 4σ filter is 10^{-4} . Therefore, the overall rate of presence of nondetections in the final data set is $2 \cdot 10^{-5}$, which is acceptable.

3.8. Fused solution, single frequency, and dual-frequency solutions

We performed six solutions that uses different observables. Of them, two are full solutions are four we residual solutions.

The main solution uses the fused group delay observables, i.e. dual-band ionosphere-free combinations of group delay observables when usable group delays were available at both bands, and single-band delays when usable group delays were available only at one band. We call an observable good if it was retained in the solution after an iterative outlier elimination procedure that keeps the normalized residuals greater than 4.5σ at S band, 4.0σ at other bands and in the fused dataset, and 3.5σ at dual-band ionosphere-free liner combinations. All global parameters were estimated in the fused and dual-band solutions, which is why we call them full solutions.

The advantage of the fused data approach is that it takes the most from the existing observations and treats inhomogeneous data in the most consistent way. The disadvantage of this approach is that it blends genuine positional offsets between frequency bands. A small fraction of sources, 2 to 6%, depending on the statistical criteria used, have different positions at different frequencies. The loss of information about these offsets is undesirable. To overcome this problem, we performed five auxiliary solutions. The first auxiliary solution used dual-band data only, i.e. X/S and X/C datasets. We mixed together X/S and X/C data because a dedicated pilot 48 hr campaign of observing 394 sources in a mode when each scan was observed two times in X/S and X/C showed no measurable biases between X/S and X/C observables (Petrov 2021) and between source position estimates. We can consider the fused solution as an extension of the dual-band solution by including single-band observations when dual-band linear combinations of observables are missing.

We ran four single-band solutions in a different mode. We applied estimates of station positions, including harmonic station position variations and nonlinear station motions in a form of the B-spline, antenna axis offsets, coefficients of the harmonic variations in the Earth parameters, and the coefficients of the expansion of the Earth orientation parameters from the fused solution as a priori in the single-band solutions. The only global estimated parameters in single-band solutions were source positions. We had to use this approach because we do not have enough data to derive positions of all the stations and the Earth orientation parameters from all the epochs from single-band solutions with an accuracy comparable to the accuracy of dual-band or fused solutions.

Strictly speaking, results of single-band solutions are not entirely independent from the dual-band solution because they implicitly depend on estimates of station positions and the Earth orientation derived from dual-band delays. We neglect this statistical dependence. The reduced set of estimated parameters decreases estimates of position uncertainties with respect to the full solution. However, reciprocal weights in single-band solutions were inflated to account for errors in the ionosphere path delay modeling, and this observation down-weighting affects the position uncertainties to a greater extent than a reduction of the number of parameters.

We represent source positions from single-band and dual-band solutions as offsets with respect to the positions from the fused solution that is considered the primary result. Positions from single-band and dual-band solutions are considered as auxiliary results.

3.9. Datasets used in astrometric solutions

Tables 2 and 3 show the statistics of the datasets used in six RFC solutions. The fused solution used dual-band observables from the geodetic experiments, both 24 hr and 1 hr, fused observables from dual-band astrometric experiments, and single-band observables from single-band astrometric experiments.

Table 2. Statistics of the RFC solutions.

Solution type	# src	# exp	# obs	postfit wrms
fused	21,942	20,575	26,005,718	25.367 ps
dual-band	17,461	20,150	22,561,262	25.097 ps
S-band	6636	466	6,124,272	270.133 ps
C-band	16,379	318	1,186,786	68.418 ps
X-band	19,742	1209	7,356,535	38.883 ps
K-band	1872	179	1,723,933	23.462 ps

NOTE—dual-band means ionosphere-free combinations of either X/S or X/C observables.

In total, 1740 sources have been detected in three or more observations in geodetic experiments. However, the frequency of observations of sources is substantially uneven. For instance, observations of 244 sources, or 14% of the total number, provided 95% of geodetic data. Among 21,942 sources detected in three or more observations in astrometric experiments, observations of 7222 objects, or 33%, provided 95% astrometric data. The median number of observations of a given source in the astrometric experiments is 41. See Figure 2 for the distributions of the number of sources with a given number observations that are used in solutions.

Table 3. Types of data used in the RFC solutions.

Data type	# sess	Duration (hr)
Geodetic 1 hr	11,848	12,118.4
Geodetic 24 hr	7,587	182,291.4
Astrometric	1,140	16,943.9
Total	20,575	211,353.3

The histogram in Figure 3 illustrates the statistics of detected sources per band. This histogram demonstrates the choice of frequencies in survey programs and does not reflect a source detectability at given frequencies.

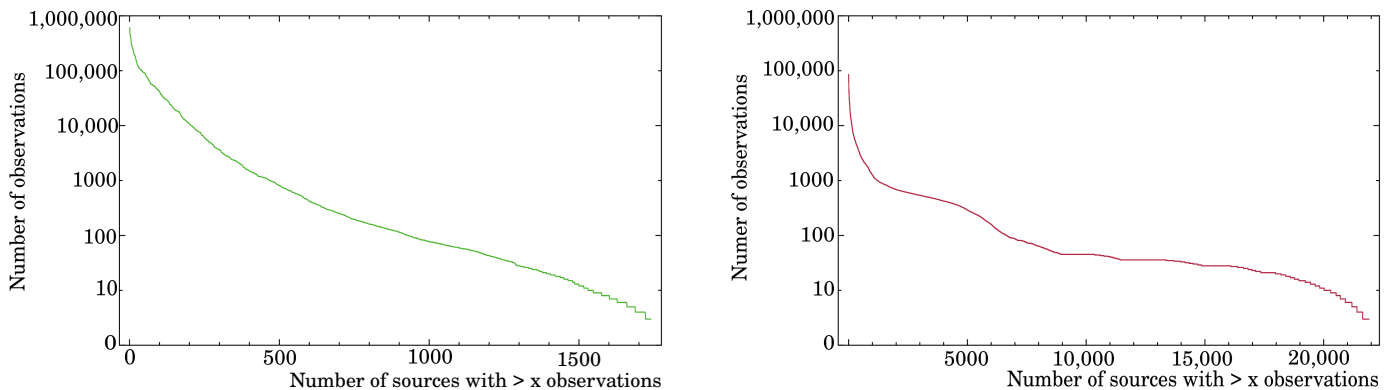


Figure 2. The distributions of sources by the logarithm of the number of observations used in the solutions in geodetic observing sessions (left) and astrometric sessions (right).

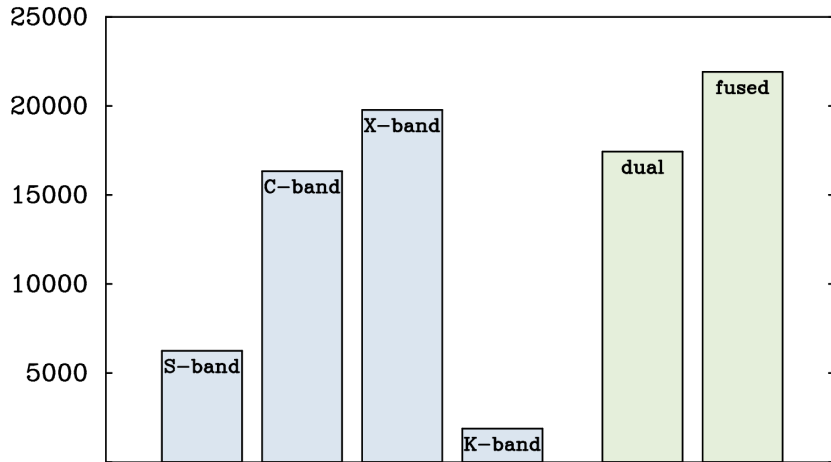


Figure 3. A histogram of the number of detected sources per band. The dual-band box shows the number of sources that have been detected in both bands simultaneously. A detected source has at least three observations that have passed the outlier detection tests.

4. ERROR ANALYSIS

It is common to call uncertainties of source positions derived from uncertainties of observable via the error propagation law formal. In the case where the parametric model fully describes the observations and the stochastic model of the observables used in the data analysis correctly describes the measurement noise, the formal uncertainties provide a realistic measure of errors of the parameter estimates. Violations of these conditions cause biases in source positional error estimates, usually as in a form of underestimation. We performed a number of statistical tests for an assessment of the reported errors.

4.1. Decimations

A common technique to assess the realism of positional errors is to perform a decimation test: to split the dataset into several groups, process them separately, and then compare. If the errors are uncorrelated and Gaussian, the differences in positions divided by the sum of individual solution errors in quadrature will be Gaussian with a zero first moment and the second moment equal to 1. In the presence of systematic errors, the moments of the distribution will be different than 0 and 1, and the distribution itself may deviate from Gaussian.

A dataset of n points can be split into two subsets with $n!$ combinations. In the presence of the red noise the decimation results will depend on the way how a dataset is split. In this paper we call a noise with the power spectral density at lower frequency greater than at high frequencies red. The longer the history of observations, the more prominent the impact of the red noise. In order to fully assess the impact of the red noise on source position estimates, we considered two extreme cases that we dubbed as local and global decimation. We sorted data of each source first in the chronological order and then in alphabetic order of baseline names. We labeled the sequence of observations as OEOEOEOEOEOE, where “O” marks an odd observation and “E” marks an even observation. The first dataset downweights even observations by a factor of 1000, and the second datasets downweights odd observations. We call this decimation local. Then we relabeled observations of each sources as FFFFFFFLLLLL, where “F” marks first $n/2$ observations of a given source and “L” marks last $n/2$ observations. We call this decimation global.

We have to limit the list of sources eligible for the decimation solution. We did not consider for our decimation tests 3205 sources that have fewer than 16 usable dual-band observations, i.e. 8 in each decimation subset, and 106 sources with more than 10,000 observations. Sources with too few observations provide unstable statistics. The frequently observed sources heavily contributed to geodetic experiments and their down-weighting would have caused a numerical instability and a degradation of estimates of the Earth orientation parameters. We would like to exclude the impact of distorted Earth orientation parameter on our results. We created four datasets of updated weights for 14150 sources: their weights were divided by a factor of 1000 for one half of observations used in the solution. Weights of the remaining 3311 sources were not modified. Two updated weight lists corresponded to odd and even subsets for the local decimations. Two other weight lists corresponded to first and last subsets of the global decimations.

Figure 4 shows the distribution of residuals divided by $\sqrt{\sigma_1^2 + \sigma_2^2}$ of decimation solutions 1 and 2. The Gaussian distribution is shown for comparison. We indeed, see significant differences in the statistics. In that figure we limited the dataset to sources with positional errors < 0.2 mas. These are mainly sources with a long history observation. In contrast, most of the sources with uncertainties > 2.0 mas were observed in one scan, and therefore, both global and local decimations would pick up observations at the same epoch, but at different baselines.

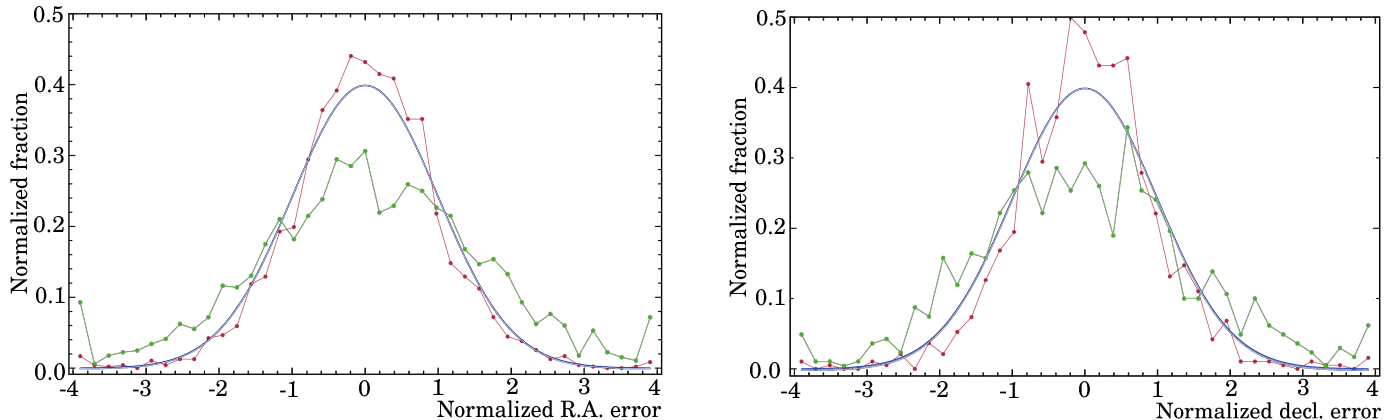


Figure 4. A histogram of normalized source positional errors for right ascensions scaled by the $\cos \delta$ factor (left) and declination (right) derived from decimation solutions. The upper red curve corresponds to the local decimation solutions. The lower green curve corresponds to the global decimation solutions. Only sources with positional errors < 0.2 mas are considered. The central blue curve is the $N(0,1)$ Gaussian function shown as a reference.

We see that results of global decimation (low green line) indicate that the errors are underestimated, while results of local decimation (red upper line) indicate the opposite. Let us recollect that we added in quadrature baseline-dependent errors computed over all observations of a given session to provide the ratios of the square of weighted residuals to their mathematical expectation close to unity. This added variance accounts for the full impact of unmodeled errors for *that experiment*. This added noise affects both “O” and “E” observables and it is partially canceled in observable differences. On the other hand, considerably fewer observations in “F” and “L” subset will be from the same observing session in the global decimation scheme. They would be affected with the red noise that is not accounted for by reweighting.

As we mentioned above, global decimation provides a strong evidence that the errors in source positions are underestimated. We seek error re-scaling in the most simple empirical form: $\sigma_{\text{final}} = \sqrt{(s \sigma_{\text{original}})^2 + F^2}$, where s is the scale that describes multiplicative errors and F is the floor that describe errors that are independent on observations. Most likely, the realistic model is more complicated, but we do not have evidence to advocate for a more sophisticated model.

We fitted for the error scale s and the floor F to the histogram of normalized residuals and sought for the minimum in residuals. Obviously, if the source positional errors are large, the impact of a small error floor is small. Therefore, we limited out analysis to sources with position errors less than 0.4 mas to exercise a balance between the sample size and the sensitivity to the error floor. Figures 5–6 show the residuals of the best fit as a function of the error floor and scale. The residual are dimensionless. Dark colors correspond to a better fit. For clarity, the dynamic range of these figures was restricted to 1:2. The spread of these diagrams illustrates the poor separability of the floor and scale parameters.

These floor-scale diagrams are very different for local and global decimations. The diagrams demonstrate rather clearly the upper limits of the error floor. They are 0.06 and 0.075 mas for right ascension scaled by $\cos \delta$ and declinations for the local decimation, respectively, and 0.12 mas for the global decimation.

The local decimation is appropriate in a situation where one investigates the potential of the observing technique to determine source positions by focusing on the short-term noise and discarding the long-term noise. The global decimation better characterizes the impact of the long-term noise. Since we focus this study to characterization of source positions averaged over the 30 year period of observations, we restrict further analysis to the global decimation.

Figures 5 and 6 present evidence that the floor and scale estimates are correlated, which does not allow us to separate the floor and scale parameters reliably without additional assumptions. We sorted positional errors in a rising order

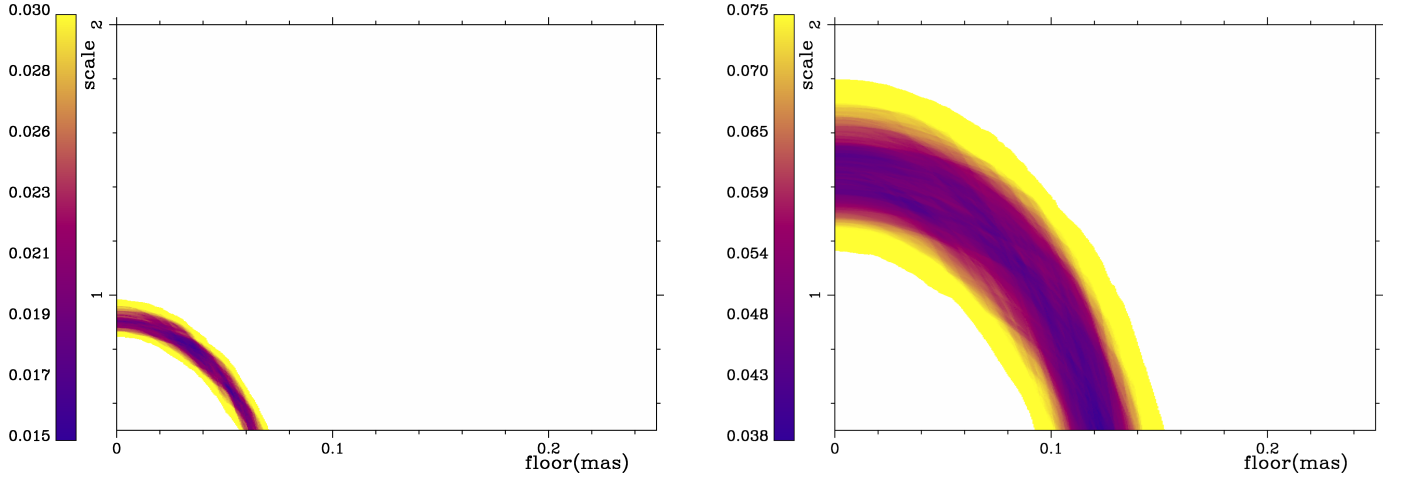


Figure 5. A floor-scale diagram for the right ascensions scaled by the $\cos \delta$ factor: local decimation (left) and global decimation (right). The color corresponds to the rms of the fit. Only the sources with positional errors < 0.4 mas are considered.

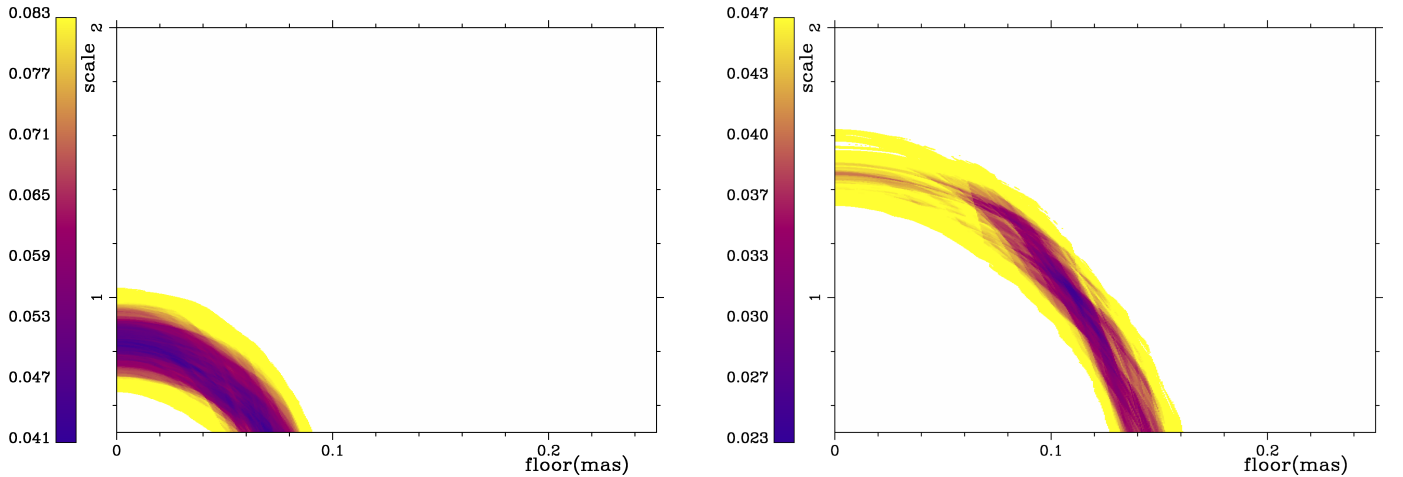


Figure 6. A floor-scale diagram for the declinations: local decimation (left) and global decimation (right). The color corresponds to the rms of the fit. Only the sources with positional errors < 0.4 mas are considered.

and computed a set of 14159 histograms of a partial datasets with a sliding window of 1000 positional errors and estimated the scaling factor keeping the floor parameter fixed to zero. Figure 7 shows the scale estimates as a function of the average error in the sliding window. We see that for errors > 1 mas, the error scale is around 1.0. The scale error wiggles from 1.0 to 1.5 for declination errors < 1 mas. We interpret this as the contribution of the error floor, which is negligible for large declination errors. Analysis of these scale estimates prompted us to make an assumption that the scaling parameters affect all the sources regardless of their positional errors. We performed a similar analysis for right ascension errors scaled by $\cos \delta$ and using all the positional errors > 1 mas, we derived the scaling factors 1.08 for right ascensions scaled by $\cos \delta$ and 1.16 for declinations.

To evaluate the error floor, we explored its declination dependence. We discarded observations with errors exceeding 0.4 mas, ordered positional errors over declination, applied scaling factors, computed the histograms for the range of declinations $[\delta_l, \delta_u]$, fitted to them the error floor, shifted the declination window by $\Delta \delta$, and repeated the process. We ran this process from declinations -40° with a window 20° and a step of 1° . We do not have enough information to derive the error floor for the sources with declinations $< -45^\circ$. These sources were observed with the arrays at the Southern Hemisphere, and therefore, they were observed in a more favorable conditions than low declinations sources observed with the northern arrays. Therefore, the error floor should be less than the maximum. In the absence of information about the error floor we elected to use the upper limit arguing that the overestimation of the error floor

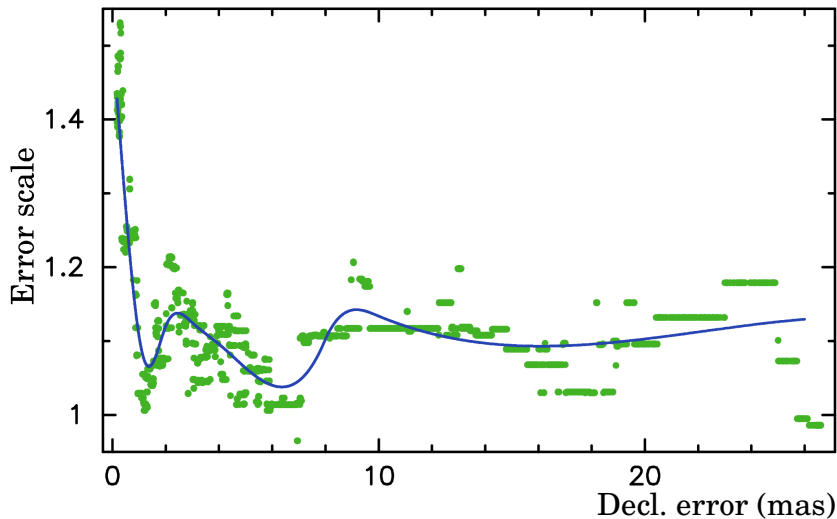


Figure 7. Estimates of the scale s for declination errors from the global declination solution with the error floor fixed to zero as a function of the mean declination error within a sliding window $[\sigma_l, \sigma_u]$. There were 1000 declination error estimates within each window. The blue line shows the result of smoothing with B-spline.

inflicts less harm than underestimation. The results of fitting the error floor with a fixed scaling factor are shown in Figure 8.

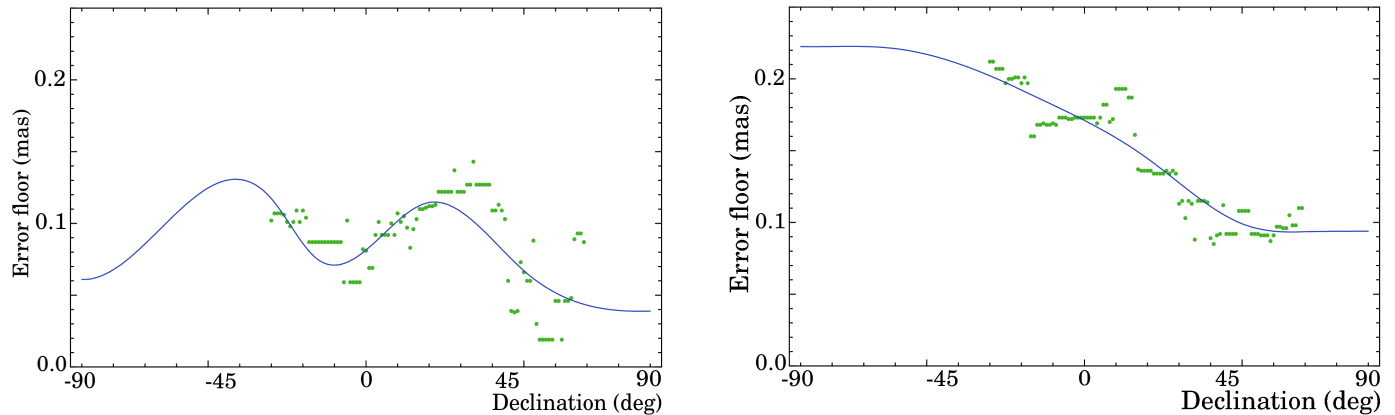


Figure 8. Estimates of the error floor from the global declination solutions as a function of declination for right ascensions (left) and declinations (right). The thin blue line approximates them with a smoothing spline.

Not surprisingly, the error floor for declination errors at low declinations is greater. The sources in the declination range $[-40^\circ, 0^\circ]$ were mainly observed with VLBA in a disadvantageous configuration at systematically low elevations and are supposed to be affected by mismodeling the atmospheric path delay to a greater extent than observations of high declination sources. The origin of the wiggling pattern of the error floor estimates for right ascension errors is not clear.

We smoothed the declination dependence of the error floor estimates with a spline by applying constraints on first and second derivatives. The error floor parameters tabulated with a step of 1° are shown in Table 13 in the Appendix. We used this scale-floor model for error re-scaling in our further analysis. Figure 9 shows the histogram of the normalized source positional errors after applying the re-scaling model. Compare them with the distribution of original errors shown in Figure 4.

4.2. Positional errors from single-band experiments

The analysis above considered the dual-band solutions. Single-band solutions suffer from mismodeling path delays in the ionosphere. In fused solutions single-band observables are properly downweighted, their share usually in the range

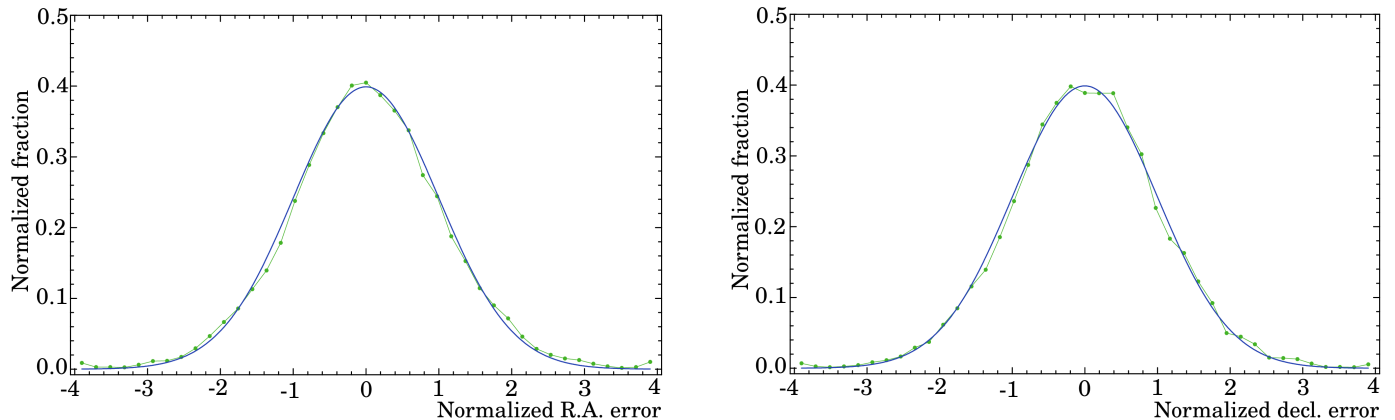


Figure 9. The histogram of the final normalized source positional errors for right ascensions scaled by the $\delta \cos$ factor (left) and declination (right) after applying error re-scaling (green points). The smooth blue curve is a Gaussian function shown as a reference.

of 10–20%, and the ionospheric biases of global TEC model were adjusted. However, position estimates derived from processing single-band experiments are affected by mismodeling ionospheric contribution to a greater extent because no adjustments of ionospheric bias is possible. Since the ionosphere has a bulge in low latitudes, ionosphere errors are declination-dependent. Observations of southern sources with the Northern Hemisphere arrays, such as VLBA, are systematically made at low elevations. Therefore, declination-dependent errors in modeling path delay in the ionosphere will be correlated with elevation-dependent errors of modeling path delay in the neutral atmosphere when observing sources at declinations in the range of $[-40^\circ, 0^\circ]$. This cross-talk is expected to lead to declination-dependent systematic errors.

Such errors were investigated in full detail in Petrov (2024). In particular, it was revealed that the differences between dual-band and K-band source position estimates can be characterized by three constituents: 1) the common intrinsic noise with a second moment of ~ 0.050 mas per component, 2) the Gaussian noise along jet directions with the second moment 0.09–0.12 mas; and 3) the noise in declination that causes a bias of 0.050 mas and the rms at a level of 0.07 mas at declinations $> 0^\circ$ that monotonically grows with a decrease in declination and reaches 0.3 mas at declination -45° . These three constituents close the error budget.

Figure 10 shows the differences in declinations from the K-band solution with respect to the dual-band solution. Only sources with declination positional errors less than 0.3 mas are shown. The thick line shows the result of smoothing using B-splines. We can see a negative bias that is growing with a decrease in declinations. The overall bias averaged over 833 sources is -0.074 mas. A similar comparison, but using a different dataset and a different set of estimated parameters in Petrov (2024) revealed a bias -0.042 mas. Is that bias an indication of some deficiency in our solution?

It is instructive to visualize the impact of including the ionospheric contribution in a solution. Surprisingly, the impact noticeably depends on whether station positions are estimated or kept fixed. Figure 11 shows the differences in declinations when the contribution of the ionosphere to path delay is included in a data reduction model. The left plot shows the differences when station positions were estimated, and the right plot shows the differences when stations are kept fixed. Estimating additional parameters, station positions and velocities, makes a solution less robust. Station position estimates absorb in part the contribution of the ionosphere. A distortion in station position causes a distortion in declination estimates. That is why we have chosen not to estimate station positions in single-band solutions.

In order to investigate the declination biases further, we ran three solutions using three data subsets. These subsets corresponded to 1) campaigns bj083 and ud001 in 2015.5–2018.5, 2) ud009 in 2018.7–2021.5, and 3) ud015, bp251, s20tj, a20, a21, a22, and a23; in 2021.5–2023.5. Station positions were not estimated. The smoothed differences in declinations are shown in the left plot of Figure 12. The upper green line in these plots corresponds to differences in solutions 1 and 2, blue and red lines correspond to differences in solutions 1 and 3 and in solutions 2 and 3, respectively. The average biases are -0.011 , -0.146 , -0.151 mas. It is worth mentioning that subsets 1 and 2 were observed during the minimum of the solar activity and the subset 3 was observed during the maximum. As expected, the differences in solutions 1 and 2 are the smallest. It is instructive to note that the declination bias is at a level of 0.2 mas. Is the declination biases a feature that is specific for K-band solutions?

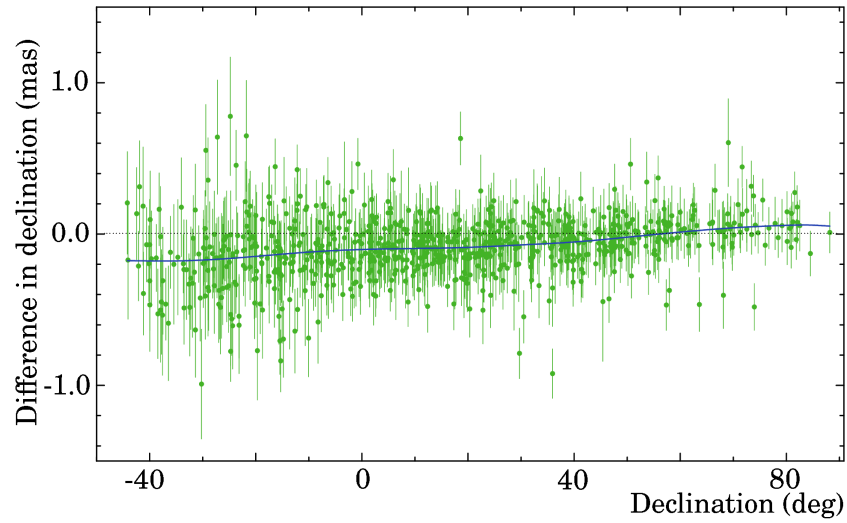


Figure 10. The differences in declinations from the K-band solution with respect to the dual-band solution. The thick blue line shows smoother differences. The dash black line shows 0.0.

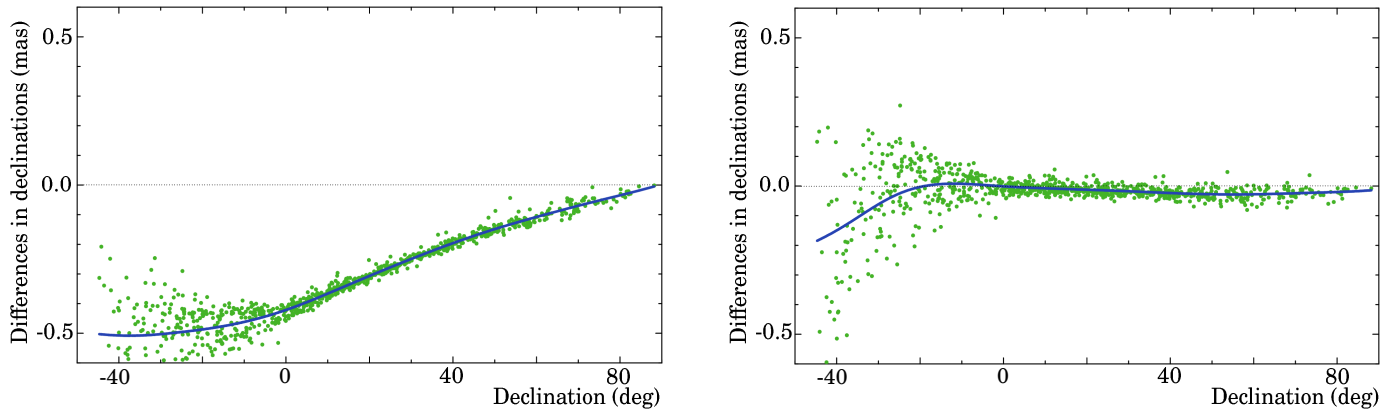


Figure 11. The differences in declinations from K-band solutions when the ionospheric contribution is applied with respect to solutions when it is not applied. *Left:* station positions are estimated. *Right:* station positions are not estimated.

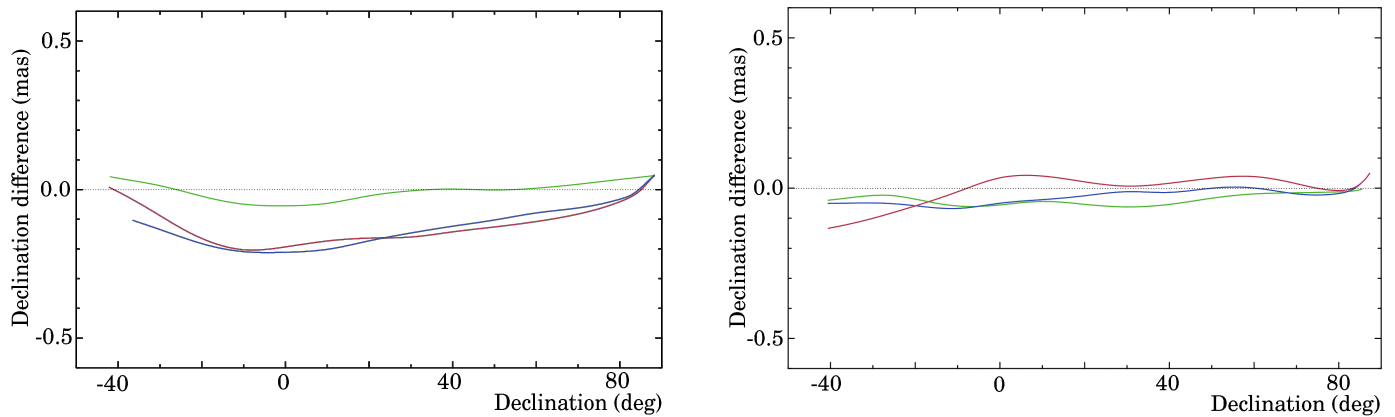


Figure 12. The smoothed differences in declinations from three solutions using subsets of data as a function of declination. *Left:* the differences in K-band solutions. *Right:* the differences in dual-band solutions.

We performed a similar test for three subsets of dual-band solutions: uf001, ug002, and ug003. Station positions were kept fixed. The differences in declinations between these three solutions are shown in the right plot of Figure 12.

The average biases are 0.022, -0.021 , and -0.040 mas, respectively. We see that declination biases at 8 GHz are 0.030–0.100 mas, which is significantly lower than at 23 GHz. We conclude that the declination biases caused by mismodeling path delay in the neutral atmosphere are enhanced by the unaccounted ionospheric contribution. We should also note that no biases in right ascension have been found. Decimation tests of the K-band solution show the presence of the extra variance on par with that found the dual-band solutions. Compare Figure 8 with Figure 16 in Petrov (2024).

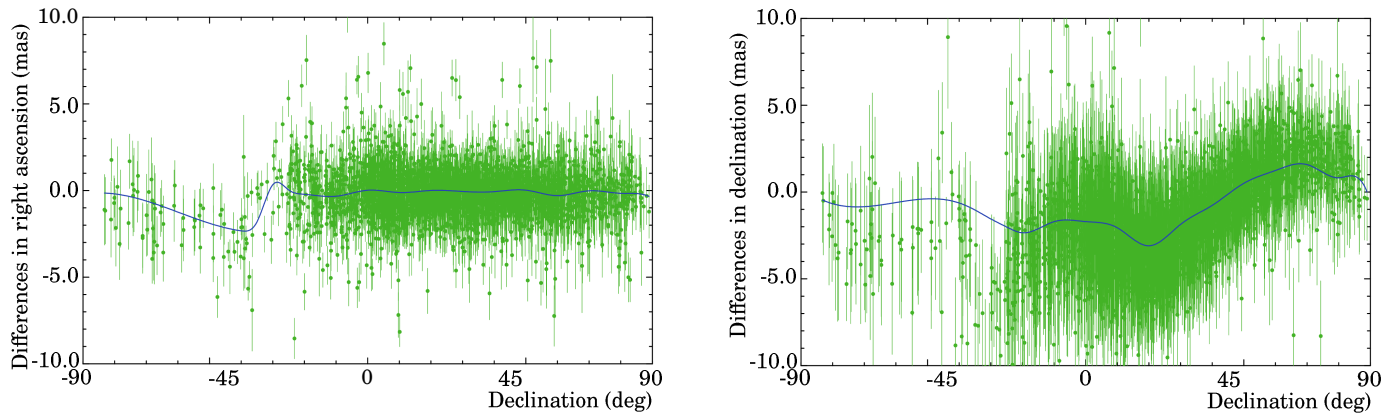


Figure 13. The differences in source position estimates from the S-band solution with respect to the dual band solution. Only sources with positional errors < 3 mas are shown. *Left:* the differences in right ascension scaled by $\cos \delta$. *Right:* the differences in declination.

Figures 13, 14, 15 show the source position differences derived from single-band data with respect to the positions from dual-band data at S, C, and X-band, respectively. We see the declination biases with the maximum approximately 3 mas at S-band, 0.7 mas at C-band, and 0.2 mas at X-band. The bias scales approximately as reciprocal to a square of the observing frequency. Differences in right ascension do not exhibit biases. We should stress that the maxima in biases of single band solutions are comparable with reported position uncertainties.

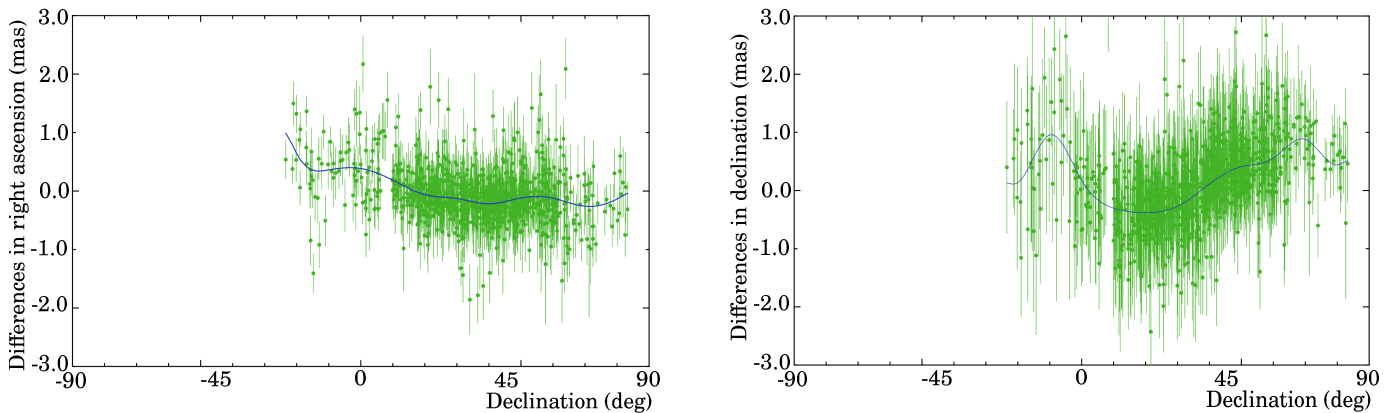


Figure 14. The differences in source position estimates from the C-band solution with respect to the dual band solution. Only sources with positional errors < 1 mas are shown. *Left:* the differences in right ascension scaled by $\cos \delta$. *Right:* the differences in declination.

4.3. Comparison with *Gaia*

The only absolute astrometry catalogue with an accuracy comparable with VLBI is that produced by *Gaia* mission (Lindgren et al. 2021). Most of the targets of *Gaia* mission are stars, but a number of AGNs were detected as well. We perform a procedure of matching common objects between two catalogues using the approach described in Petrov & Kovalev (2017a). We determined the list of 12,864 common sources in both catalogues with the probability of false associations not exceeding 0.001. The procedure of cross association is described in section 6.4.

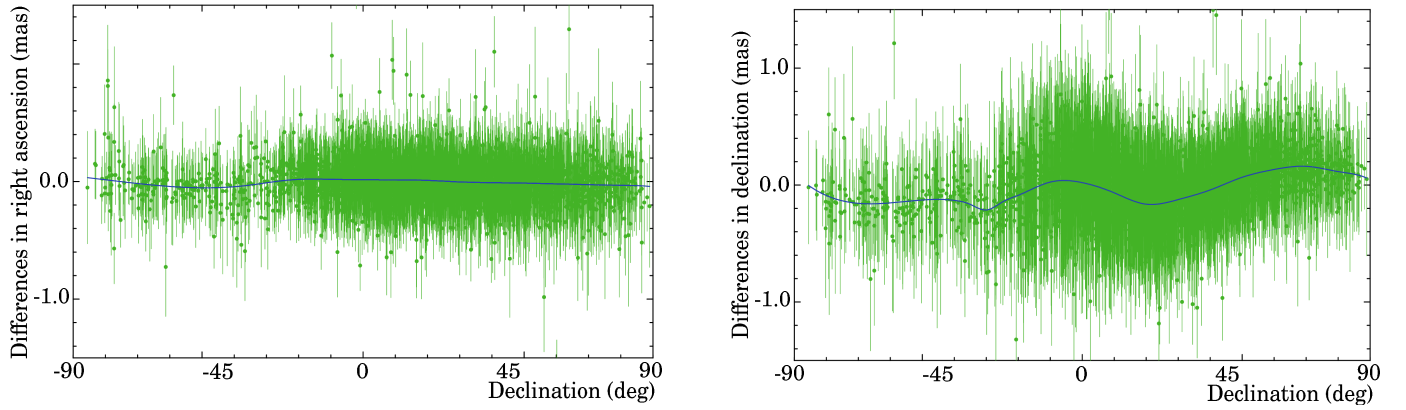


Figure 15. The differences in source position estimates from the X-band solution with respect to the dual band solution. Only sources with positional errors < 0.5 mas are shown, solutions using subset of data as a function of *Left*: the differences in right ascension scaled by $\cos \delta$. *Right*: the differences in declination.

A cursory examination of plots of position differences of the common sources did not reveal significant biases in source positions between these two catalogue along right ascension and declinations. The declination bias is -0.025 mas. However, a close examination revealed that the differences from *Gaia* positions with respect to RFC positions favor the declination direction. Figure 16 shows the histogram of the position angles of the *Gaia* positions with respect to the RFC positions. It turned out the less observations a given source had, the more noticeable peaks around 0° and 180° are in the histogram. The sources that had fewer than 30–60 observations were mostly observed in 1 to 2 scans with the VLBA. positional errors of these sources along declination are greater because the extension of the VLBA along longitude. The geometry of the VLBA has less impact on positions of those sources that were observed in many scans. We interpret it as observing in more than 1–2 scans provides a better sampling of different projections of baseline vectors on the source direction, which makes estimate of source position more stable, in a similar way as more scans makes a better *uv*-coverage, which improves image fidelity.

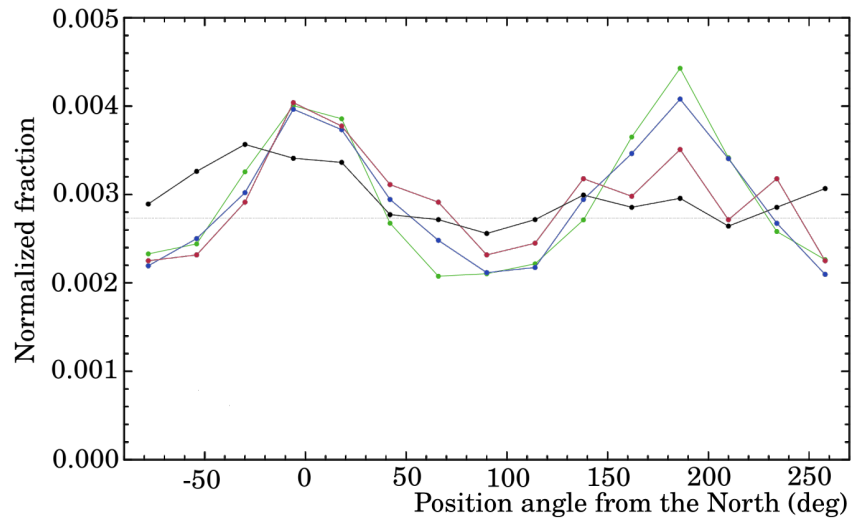


Figure 16. The normalized distributions of position angles of the differences in source coordinates from *Gaia* with respect to RFC counted from the north celestial pole (green circles) for four subsets. Each subset corresponded to sources that had a certain range of the number of observations used in a solution. The green line: 3 to 40; the blue line: 40 to 80; the red line: 81 to 120; and the black line > 120 . The thin dashed red line shows a uniform distribution.

In order to assess the level of the agreement between the RFC and the *Gaia* Data release 3 (Lindgren et al. 2021), we computed arc lengths between VLBI and *Gaia* positions along those 12,864 matches. We computed the uncertainties of these arc lengths based on reported uncertainties in right ascension and declination from both VLBI and *Gaia*

solutions and correlations between them (see Petrov et al. 2019b, for details of the computation). The left panel of Figure 17 shows the distribution of arc lengths among all matching sources. We see the distribution has a certain deviation from the Rayleigh distribution. What is the origin of this deviation?

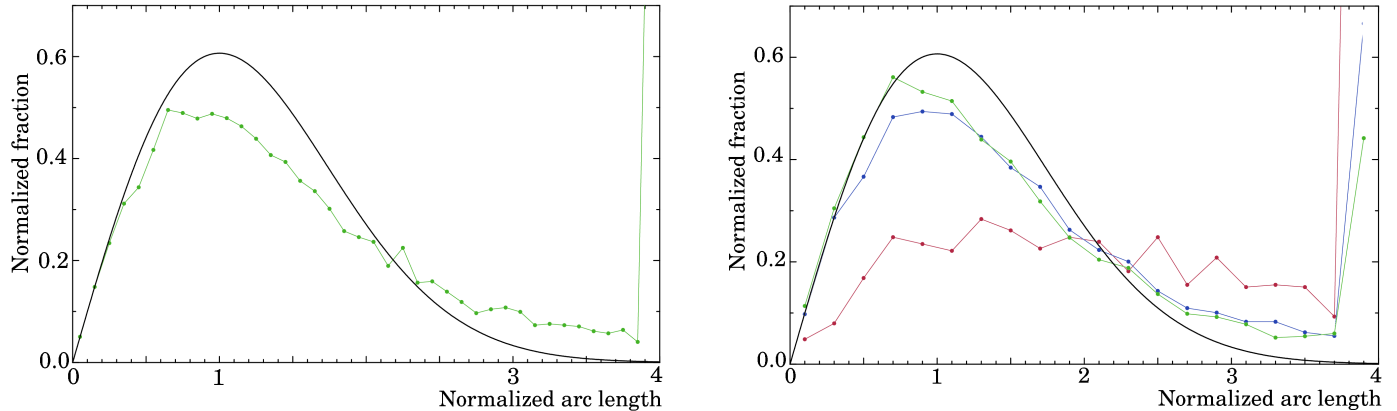


Figure 17. The distributions of the normalized arc lengths between RFC and *Gaia* position estimates. A Rayleighian distribution with $\sigma = 1.0$ is shown with a black thick line for reference. Left: all the matching sources. Right: the dataset was split into three subsets according to χ^2/ndf *Gaia* variable: the green line: $\chi^2/\text{ndf} < 1.1$, the blue line: $1.1 < \chi^2/\text{ndf} < 2.0$, and the red line: $\chi^2/\text{ndf} > 2.0$. The last bin collects all the normalized arc lengths ≥ 4 .

It was noted in Petrov et al. (2019b) that the statistics of *Gaia* source positions depend on parameter `astrometric_chi2_al` from the *Gaia* catalogue, which is the ratio of χ^2 per degree of freedom. We split the dataset into three brackets of χ^2/ndf : < 1.1 (46% matches); $[1.1, 2.0]$ (43% matches); and > 2.0 (11% matches) and computed the arc length distribution for each dataset. The results are shown in the right panel of Figure 17. The distribution from the subset with $\chi^2/\text{ndf} < 1.1$ is the closest to the Rayleighian distribution, while the distribution from the subset with $\chi^2/\text{ndf} > 2.0$ is strongly non-Rayleighian. Can the remaining difference be explained by omission of some error scaling factor in the VLBI solution?

To investigate the validity of the RFC source positional errors further, we formed a subset of data with a) $0.9 < \chi^2/\text{ndf} < 1.2$; b) excluding those sources that have the position angle of differences VLBI minus *Gaia* with respect to the jet direction less than 30° ; c) the semi-major axis of the positional error ellipse < 0.2 mas either VLBI or *Gaia*. It was found in Petrov & Kovalev (2017a); Kovalev et al. (2017) that VLBI/*Gaia* positions differences favor the jet direction (Plavin et al. 2022). Strong pieces of evidence were presented in Petrov & Kovalev (2017b); Petrov et al. (2019b); Plavin et al. (2019a); Lambert et al. (2024) in favor of the explaining this phenomena with the presence of bright optical jets that are shorter than the *Gaia* point spread function, but are still long enough to affect positions of source centroids in the optical range. Exclusion of these objects eliminates the origin of the discrepancies that is not related to astrometry errors. We excluded sources with small position errors to avoid a dichotomy whether the error re-scaling models should be additive or multiplicative since we cannot discriminate them. We divided *Gaia* sources uncertainties by χ^2/ndf following the line of evidence presented in Petrov et al. (2019b). Then we computed three distributions by scaling VLBI errors by a factor 1.0, 1.2, and 1.4. The distributions are shown in Figure 18.

We see that re-scaling VLBI errors even by a factor of 1.2 increases the disagreement with the *Gaia* catalogue. When we increase the scaling factor, the distribution of normalized arc lengths is shifted to the left. Although we excluded a number of sources in these tests, it did not cause a selection bias for the validation of VLBI error model, because the exclusion criteria were based entirely on properties of the *Gaia* sample.

Presented results allow us to conclude that a) the deviation of the normalized arc length distribution of RFC/*Gaia* EDR3 position differences is explained in part by unaccounted *Gaia* positional errors and by the presence of milliarcsecond scale source structure; b) the upper limit of biases in the RFC error model is 20%, which is in line with Lindegren et al. (2021).

4.4. Impact of source structure

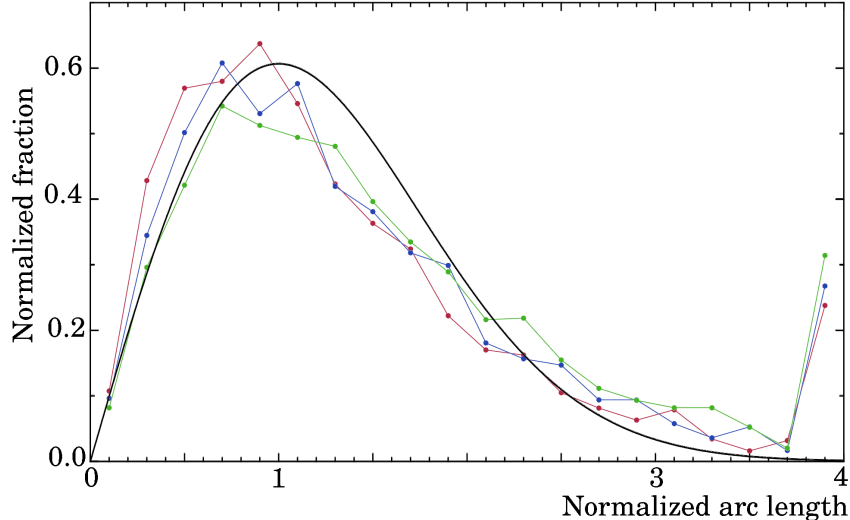


Figure 18. The distributions of the normalized arc lengths between *Gaia* and RFC position estimates from a subset of matching sources with differently re-scaled errors. A Rayleighian distribution with $\sigma = 1.0$ is shown with a black thick line for reference. The green line shows the distribution without re-scaling. The blue line shows the distribution with a re-scaling factor of 1.2. The red line shows the distribution with a re-scaling factor of 1.4.

Equation 28 relates the position of a point with coordinates \mathbf{s} . In general, the complex coherence function Γ_{12} according to the Van Zitter-Zernike theorem is:

$$V_{12}(b_x, b_y, f) = e^{2\pi i f \tau_0} V_s(b_x, b_y, f),$$

$$V_s(b_x, b_y, f) = \iint_{-\infty}^{+\infty} B(x - x_0, y - y_0, f) e^{-2\pi i(xu + yv)} dx dy, \quad (28)$$

where f is the circular reference frequency of received signal, τ_0 is the geometric delay to the nominal reference point on the source (x_0, y_0) , B is a two-dimensional function of the brightness distribution, which depends on angular coordinates x, y along right ascension and declination and on frequency, and $u = b_x f/c$, $v = b_y f/c$ are scaled projections of the baseline vector $\mathbf{b} = \mathbf{r}_1 - \mathbf{r}_2$ to the plane that is perpendicular to the image plane at the image nominal reference point.

When $B(x, y) = \delta(x, y)$, the integral in the lower formula in equation 28 becomes 1 and the source structure contribution $\tau_{\text{gr, str}} \frac{1}{2\pi} \frac{\partial}{\partial f} \arg(V_s)$ becomes zero. The integral will be constant also if a source has a circular symmetry.

In all other cases the source structure will not be zero. Thomas (1980) and later Charlot (1990) considered a simple case of a two-component model. Although the contribution of group delay for that simple case can be written in a close form analytically, the contribution of source structure to source position does not have a simple analytical form. It depends not only on the source brightness distribution, but also on the geometry of the network and on the observing schedule.

When the source brightness distribution is well known, source contribution to group delay can be computed from the integral in expression 28. Although the feasibility of this approach was established in Campbell et al. (1988), source structure contribution is not yet applied on a routine basis because of logistical difficulties in developing of the infrastructure that would support the synthesis of reliable images and identifying the reference point on the image in an automatic fashion using all the data. The RFC catalogue, like all other prior VLBI astrometry catalogues, does not apply source structure contribution, and the omission of such a correction propagates as a systematic source-specific error to reported positions.

We can evaluate the magnitude of these errors via simulation, comparison of source positions with and without applied source structure contribution, and via comparison of source positions derived without applying the source structure contribution at difference frequencies. The simulation study of Plank et al. (2016) demonstrated that the contribution of source structure to delay at 8 GHz affects source positions in the range of 10–80 μas for most of the

sources. In Petrov & Kovalev (2017b) we processed a dataset of 29 active galactic nuclei observed under MOJAVE program (Lister et al. 2018) at 15 GHz, computed source structure contribution to group delay from images, applied it to data analysis, derived source positions, and compared source position estimates with and without accounting to source structure. Position differences were in the range from 0.01 to 2.40 mas with the median of 0.06 mas, which is consistent with simulation.

In Petrov (2024) we computed the position angles of the differences in source coordinates derived from X/S data with respect to source coordinates derived from K-band data, subtracted the position angle of jet direction, and built a histogram of the resulting position angles counted from jet directions. That histogram showed two peaks along and opposite to the jet direction. Detailed modeling of the histogram allowed us to estimate the magnitude of the systematic position differences along the jet direction in a form of a Gaussian distribution. The second moment of the Gaussian distribution was in the range of 90 μas (low limit) to 120 μas (upper limit). Since the jet axis is the intrinsic property of the source that describes the asymmetry of the brightness distribution, these systematic errors are undoubtedly associated with the presence of source structure and/or core shift. All these estimates are consistent with each other and indicate that *on average*, the unaccounted source structure contribution is close to 70 μas per source position component, right ascension and declination.

Words “on average” are essential in the above mentioned estimate. Comparison of X/S and K-band catalogues in Petrov (2024) showed that the position differences derived from X/S data versus derived K-band data exceeded 3σ for 6% sources and 5σ for 2% sources. There are sources with differences in position estimates derived from observations at different frequencies that exceed the average difference by orders of magnitude. Examples of such sources were reported for the first time in Petrov et al. (2011a). Later, more sources like those have been found (for instance, Petrov 2013; Titov et al. 2022; Xu et al. 2022). All of these sources have a striking feature: they have two or more compact components with a comparable brightness. The most prevailing class of such sources show core-jet morphologies with a compact bright hot spot in the jet. The second, more rare class is gravitational lenses (Claeskens & Surdej 2002). And finally, there are several sources that are genuine binary systems, such as J0405+3803 (Rodriguez et al. 2006), J0749+225A/J0749+225B (Shen et al. 2021), and J2157+662A/J2157+662B (I. Duev et al., in preparation) of gravitationally bounded AGNs. Establishing the nature of these sources is in general not an easy task, and it requires supporting argumentation. This task goes beyond the scope of the current study and we reserve it for future publications. Here we collectively call these sources visually binary.

The fringe fitting process, as implemented, implicitly assumes that the source brightness distribution is a δ function. Morphologies in the form of a compact core and an extended asymmetric feature do not affect the efficiency of the fringe fitting process in a measurable way. However, morphologies in the form of more than one compact components do affect the fitting. It is advantageous to apply an a priori source brightness distribution model during fringe fitting in processing VLBI observations of gravitational lenses (Porcas 2004). We did not do that step to keep data analysis uniform. Sources with more than one compact component will be reprocessed in the future.

Since with rare exceptions the spectral index of a core is flat, but the spectral index of a hot spot in a jet is steep (e.g., Hovatta et al. 2014; Plavin et al. 2019b), situations when the hot spot is brighter at a low frequency, but the core is brighter at a higher frequency, are not uncommon. There are instances that the position estimate at a low frequency corresponds to one component (usually a hot spot in a jet), but at higher frequencies it corresponds to another component (usually a core). Such sources are called colloquially “flip-floppers.” Such a feature affects source position estimates from single-band data: the reported position is close to the specific source component. Such a feature affects the source position estimate from dual-band data as well, but in a way that is a little bit less obvious: the dual-band position estimate is shifted by a factor of $a = f_l^2/f_u^2$ along the line connecting two components in the direction opposite to the second component.

In Petrov (2024) we found that the total number of outliers between dual-band, quad-band, and single-band observations at 23 GHz exceeding 3σ was at a level of 6% and exceeding 5σ was at a level of 2%. For most of these cases a close examination of images easily revealed peculiar source structure, f.e., the presence of a second component. It follows from this comparison that for 94% of the sources the contribution of source structure on source position is not detected, and for 2% of the sources it is definitely dominates the error budget.

We note that even if the source structure effect can be compensated for, this does not mitigate the problem of the absence of a stable reference point in extragalactic radio sources. Physically, we expect the nuclei of active galaxies, i.e. supermassive black holes and accretion disks surrounding them, as well as the true base of AGN jets, to have stable positions (Blandford et al. 2019). However, they are not observable with ground-based VLBI arrays at centimeter

wavelengths. The next subsection discusses in detail properties of the bright apparent jet base that is also called “the core” — the feature that is actually observed.

4.5. Impact of the core-shift on reported source positions

AGN morphology at milliarcsecond resolutions is typically characterized by an opaque core and an optically thin jet that may or may not show bright features on VLBI images (Hovatta et al. 2014; Lister et al. 2018; Blandford et al. 2019). Due to the limited dynamic range, the jet may not be detected, but the core as a partially resolved feature is almost always present. The size of the visible core is determined by the area for which the optical depth due to synchrotron self-absorption is close to unity (Blandford & Königl 1979). The center of the core is shifted along the jet with respect to the central engine due to the synchrotron opacity. For simplicity, we assume here that the distance between the AGN central engine and the true physical jet base is equal to zero.

Since the synchrotron opacity depends on frequency f , the apparent core-shift is frequency dependent (Lobanov 1998). Considering the core-shift frequency dependence is described as a power law, the source position $\mathbf{S}(f) = \mathbf{S}_0 + \mathbf{h} f^a$, where \mathbf{h} is usually aligned with the jet direction. In the first approximation, the fringe phase is the product of the travel distance difference and frequency divided by the speed of light. Phase delay is the ratio of the fringe phase to the reference frequency and therefore, is equal to the travel distance difference divided by c , while group delay is a partial derivative of fringe phase over frequency:

$$\tau_{\text{gr}} = \frac{1}{c} \frac{\partial(f(\mathbf{S}_0 + \mathbf{h} f^a) \cdot \mathbf{b})}{\partial f} + O(c^2) = \frac{1}{c} \mathbf{S}_0 \cdot \mathbf{b} + \frac{1}{c} (1+a)(\mathbf{h} \cdot \mathbf{b}) f^a + O(c^2), \quad (29)$$

where \mathbf{b} is the baseline vector in the inertial coordinate system.

When the energy density of the relativistic particles and magnetic field is approximately equal, the so-called equipartition condition, and jet geometry is conical, this dependence is predicted to be f^{-1} (Königl 1981; Lobanov 1998). Observations, in generally, confirm that (e.g., Kovalev et al. 2008; Sokolovsky et al. 2011; Abellán et al. 2018). However examples of deviations of the power law from -1 are also known (e.g., Kutkin et al. 2014; Chamani et al. 2023).

To make the situation even more complicated, according to Plavin et al. (2019b); Chamani et al. (2023), core-shift varies with time on a scale from months to years, and these variations are related to a flaring activity. During flares the density of charged relativistic particles moving through the jet changes. These disturbances cause a violation of the equipartition condition, and as a result, break the -1 power law. Moreover, due to the basic causality arguments and the finite speed of plasma propagation along the jet, any plasma disturbance moving along the jet will break the -1 power law (Plavin et al. 2019b).

When the power law index in the core-shift versus frequency dependence is -1 , as we see from equation 29, core-shift has no impact on astrometric position derived from group delays which in this case pinpoints the true base of AGN jet as it was pointed out by Porcas (2009). We underline that this is the case for all presented solutions: fused, dual-band, and single-band. The core-shift impacts source positions derived from group delays only when the power law index deviates from -1 , the closer the power law index to -1 , the less is its impact.

We do not apply correction of the core-shift to data reduction. Therefore, its contribution manifests as a noise which is challenging to evaluate due to the complex effects discussed above. To date, the core-shift was measured for more than a hundred AGNs by Kovalev et al. (2008); Sokolovsky et al. (2011); Pushkarev et al. (2012) and its variability was systematically studied in 40 AGNs (Plavin et al. 2019b). Namely, it was found that the typical differential core-shift between 2 and 8 GHz was on a level of 0.4–0.5 mas, but it may reach 1.5 mas (Kovalev et al. 2008; Plavin et al. 2019b). According to Plavin et al. (2019b), the typical differential core-shift rms between 2 and 8 GHz is 0.18 mas. Kovalev et al. (2008) provided a theoretical estimate of the typical core-shift between 8 GHz and the true jet base: 0.1 mas. However, when source positions or source position differences are derived from *phase delays*, the core-shift will affect them at that level.

In order to estimate the magnitude of the core-shift impact on RFC source positions, we need to utilize epoch-specific variability information on both as well as the core-shift value and its power law, which are currently poorly known. The scarcity of such measurements prevents us from making quantitative estimates. In Petrov (2024) we have established that the extra noise along the jet between 8 and 24 GHz positions has a second moment of 0.09 mas. We attribute this to both the core-shift and source structure contribution. This estimate can be considered as a conservative upper bound of the differential core-shift impact between 8 and 24 GHz.

4.6. *Impact of scattering in the interstellar medium*

A source positional error from a given observation is reciprocal to the projected baseline length. Due to refractive scattering in the interstellar medium (Pushkarev & Kovalev 2015; Koryukova et al. 2022), the correlated flux density at long baselines at low frequencies is substantially reduced, sometimes by one order of magnitude, and a corresponding image reveals a smooth elliptical Gaussian shape — see Figure 19 as an example.

Scattering in the interstellar medium affects mainly compact AGNs within $\pm 10^\circ$ of the Galactic plane. Group delay uncertainties are increased by the same factor, which increases the positional error. Correlated signal at long baselines may fall even below the detection limit, and therefore, such observations will not be used in data analysis, which increases the source positional error even further. The scattered source size typically depends on frequency as f^{-2} , while the intrinsic opaque core size depends on frequency as f^{-1} (see discussion in Lobanov 1998; Pushkarev & Kovalev 2015; Koryukova et al. 2022). As a result, the higher the frequency, the lower the influence of scattering is expected on astrometric accuracy.

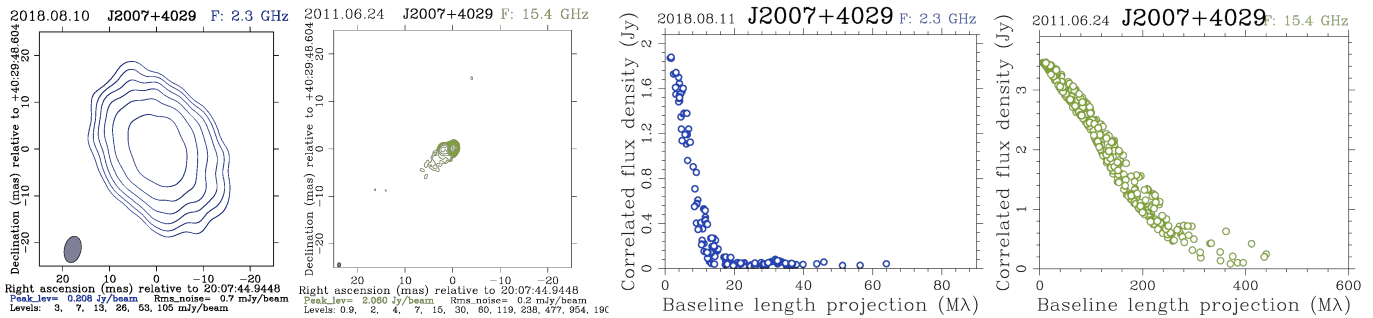


Figure 19. Example of a source that is affected by scattering in the interstellar medium. The first plot from the left: scattered image at 2.3 GHz. The second plot: image of the same source at 15.4 GHz where scattering is negligible. The third and the fourth plots show the calibrated visibility amplitude as a function of the projected baseline length. See details in Koryukova et al. (2023).

We should notice that correlated amplitudes in Figure 19 have a steep drop in the range from 0 to 15 $M\lambda$, but then do not vanish, and stay of 1–2% of the peak level in the range of 20 to 64 $M\lambda$. This pattern is due to the presence of refractive scattering substructures in an AGN, originally discovered for Sgr A* with the VLBA+GBT (Gwinn et al. 2014) and found also in quasars (Johnson et al. 2016) using Space VLBI observations with *RadioAstron* (Kardashev et al. 2013). Although in these cases the scattering is broad enough to be completely resolved out, substructures with smaller size are compact enough to provide a measurable flux density at long baselines with a random, noise-like character. According to Gwinn et al. (2014), the substructure is expected to be fixed for a time of an observing session, 4 to 24 hour and average out over times longer than that for Galactic rotation to carry the line of sight across the scattered image, i.e. a few weeks. Although these observations at long baseline will be used in astrometric solutions, the position estimates will be related either to the scattering substructure of an AGN if data from only one epoch are used, or will be affected by a jitter due to changing substructures when data from many epochs are used in data analysis.

Additionally, a lens-like structure in the ionized component of the Galactic interstellar medium may rarely produce multiple images of a compact AGN due to refractive plasma effects. This can be observed at parsec scales. Such a phenomenon can affect even high radio frequencies and, consequently, degrade astrometric solutions, see an example for the quasar 2023+335 at 15 GHz in Pushkarev et al. (2013).

4.7. *Comparison with ICRF3*

Since most VLBI data are publicly available, there are other groups that use the data and derive source positions. It is instructive to compare our catalogue with other solutions based on a subset of the full collection of VLBI data. We selected for comparison the ICRF3 catalogue (Charlot et al. 2020). The ICRF3 catalogue lists positions of 4536 sources derived from the dual-band solution and 824 sources derived from K-band. It also contains positions derived from 32 GHz VLBI data, but since that catalogue is based entirely on proprietary data, we exclude it from consideration. All the sources from the ICRF3 catalogue are found in the RFC, and therefore, we can consider it as a subset of the

RFC, approximately 1/5 of the total RFC source count. The ICRF3 includes *some* astrometric programs (see for details Charlot et al. 2020), while we aimed to use *all* suitable observations in our work.

The two catalogues, RFC and ICRF3 (dual-band version), are rotated against each other at angles of 0.024, 0.048, and -0.042 mas along x-, y-, and z-axes. The declination bias defined as the weighted mean declination difference, which is -0.020 mas. The catalogues have a different error model. The ICRF3 catalogue was derived from group delays computed by the AIPS and Fourfit software (Greisen 2003; Gordon et al. 2012), which did not account for the phase noise and therefore, their estimates of group delay uncertainties were smaller and less realistic than those derived by *PLMA* (Petrov et al. 2011a). The ICRF3 catalogue adopted a multiplicative scaling factor of 1.5 and an error floor of 0.030 mas based on the local decimation, while RFC used scaling factors 1.08 and 1.16 for right ascensions and declination and the declination-dependent error floor in a range from 0.06 to 0.2 mas based on results of global decimation.

Figure 20 shows the share of sources with the differences $|\Delta x|$ in the positions between two catalogues as a function of the significance level defined as $|\Delta x| < N\sigma$. In order to account for the disparity of the error models, three distributions were plotted: $|\Delta x| < N \min(\sigma_{\text{rfc}}, \sigma_{\text{icrf3}})$ (upper plot), $|\Delta x| < N\sigma_{\text{rfc}}$ (middle plot), and $|\Delta x| < N \max(\sigma_{\text{rfc}}, \sigma_{\text{icrf3}})$ (low plot). It is remarkable that one third of the sources have differences at the 3σ level when the minimum between the uncertainties of the two catalogues is considered. What is the origin of these differences?

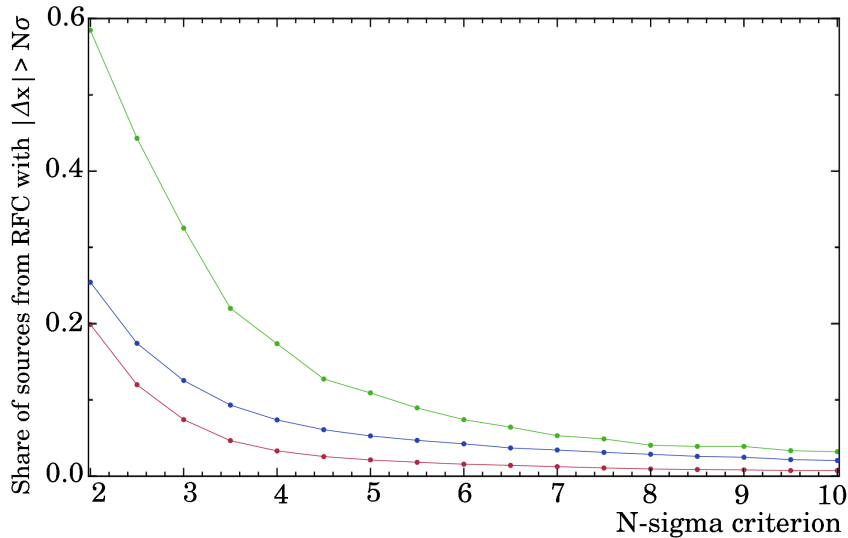


Figure 20. The distribution of the share of sources with position differences between the RFC and ICRF3 catalogues significant at a given $N\sigma$ level. The upper green line corresponds to $\sigma = \min(\sigma_{\text{rfc}}, \sigma_{\text{icrf3}})$. The middle blue line corresponds to $\sigma = \sigma_{\text{rfc}}$. The low red line corresponds to $\sigma = \max(\sigma_{\text{rfc}}, \sigma_{\text{icrf3}})$.

The position uncertainties in the RFC and ICRF3 catalogues heavily depend on the number of observations. For all the sources, the RFC uses all the observations the X/S ICRF3 catalogue used and many other observations the ICRF3 did not use. For frequently observed sources for which ICRF3 positional errors < 0.1 mas, the RFC uncertainties are greater by the factor of 3.54 for right ascension and 2.12 for declinations. For the sources with ICRF3 positional errors < 0.2 mas, the RFC uncertainties are greater by factors of 2.90 and 1.76 because of differences in the error scaling model: the RFC uncertainties account for the red noise while the ICRF3 uncertainties do not. From the other hand, for those sources for which the ICRF3 errors exceed 0.5 mas, the RFC errors are 0.35 and 0.57 of the ICRF3 errors for right ascensions and declinations. Among the sources with ICRF3 errors greater than 1.0 mas, their RFC errors are 0.28 and 0.38 of ICRF3 errors, i.e. the positional accuracy is better by a factor of 3–4 due to including more observations in analysis. Within each bin in Figure 20, about 60% of the sources have significant differences because their ICRF3 position uncertainties are too small, and remaining 30% have significant differences because the ICRF3 solution used only a small share of the observation that the RFC solution used. Sources with differences more than $3 \times \max(\sigma_{\text{rfc}}, \sigma_{\text{icrf3}})$ fall into two categories: the sources with many more used observations in the RFC than in the ICRF3 and peculiar sources, such as visual doubles. As an example, Figure 21 shows images of two sources that have position differences more than 25σ .

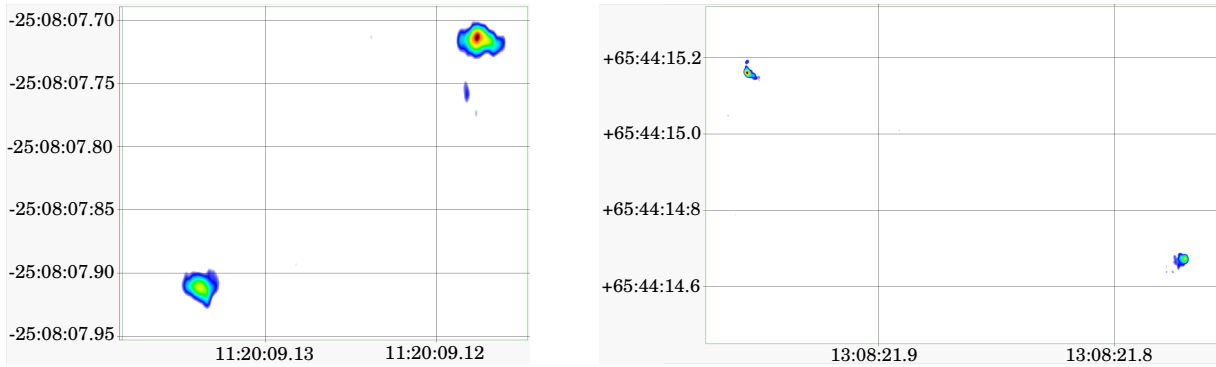


Figure 21. Example of S-band images of sources with large differences between RFC and ICRF3 catalogues. *Left:* RFC J1120–2508. *Right:* RFC J1308+6544.

The uncertainties of K-band positions are about a factor of 2 smaller in the RFC catalogue than in the ICRF3 catalogue owing to much more observations used. The declination bias of our K-band source positions with respect to ICRF3 is -0.075 mas. There is no declination bias of the ICRF3 K-band catalogue with respect to the ICRF3 dual-band catalogue. Since the ICRF3 catalogue used sixteen K-band experiments that are not publicly available, we cannot reproduce the K-band ICRF3 solution exactly. Therefore, the origin of the bias is not firmly established. We should note that in general, the declination bias in source positions derived from K-band is not stable since it depends on the total electron content in the ionosphere. We found comparable biases when we processed subsets of K-band data (see left plot in Figure 12). This helps to explain the discrepancies of the ICRF3 K-band catalogue against the RFC catalogue.

The 25%, 50%, and 75% quartiles of the semi-major error ellipse axes of the dual-band version of the ICRF3 are 0.14, 0.22 and 0.41 mas respectively. The same statistics of the RFC catalogue *among the list of sources present in the ICRF3* are 0.16, 0.22, and 0.29, respectively. We see that the first quartile of the positional error of the ICRF3 catalogue is 15% smaller because it does not account for the red noise, the second quartile, i.e. the median are the same, and the positional accuracy of the RFC is 38% greater in the third quartile because the RFC is based on more observations than the ICRF3. Table 4 shows the number of sources with positional errors less or greater than some limit. The number of sources with positional errors less than 0.21 mas is the same in both catalogues, but then this number from the RFC grows much faster.

Table 4. The number of sources with the semi-major error ellipse axis within certain error ranges in the ICRF3 and RFC catalogues.

Error (mas)	ICRF3 # src	RFC # src
< 0.2	2022	1887
< 0.3	2899	3896
< 0.5	3653	5658
< 0.7	3961	6797
< 1.0	4177	8547
< 1.5	4319	11690
< 2.0	4376	14111
> 2.0	160	7797

5. A BRIEF OVERVIEW OF THE IMAGE RESULTS

A catalogue that has only positions and does not provide information about source flux density has a limited use. We have imaged most of the sources. The current data release has information about historic median correlated flux densities for 21,730 sources, or 99%. For most of the VLBA experiments we processed the records of system

temperature measurements, flagged out outliers, interpolated them for missing values, computed the a priori system equivalent flux density (SEFD), and calibrated fringe amplitudes. Then we applied group delay and phase delay rate determined by the fringe fitting procedure, calibrated the complex bandpass, estimated and applied amplitude renormalization, determined time intervals when antennas did not point on sources and flagged them out, flagged the observations that have been deselected during the astrometric analysis, averaged fringe visibilities over time within a scan and over frequency within each IF for each source and each band, and combined averaged visibilities for a given source over a certain period time in the range from one experiment (4–24 hours) to 4 months. Since most of the sources were observed in one or several scans, combining data densifies the uv -coverage, and therefore, improves image fidelity. From the other hand, combining data over a longer period of time may distort an image because of source variability. The process of generation of a priori calibrated time- and frequency-averaged visibilities from survey data was performed with *PTMA* for most of the campaigns, except VCS1–6, NPC5, and some other experiments that were calibrated with AIPS and imaged with Difmap (Shepherd 1997). We produced images performing the hybrid synthesis technique in a batch mode. This follows the approach suggested by Pearson et al. (1994) utilizing the software package Difmap. Finally, we have screened all the images and reprocessed manually those images that showed anomalies, usually related to flagging of data with poor amplitude calibration. This procedure is discussed in more details in Petrov (2021).

We put all the images, a priori calibrated visibility data, also known as uva-data, self-calibrated visibility data after the hybrid image reconstruction algorithm, also known as uvs-data, in a publicly accessible Astroge0 VLBI FITS image database <https://doi.org/10.25966/kyy8-yp57>. In addition to our own work, the database has the contributions from many scientists who decided to make images that they have synthesized publicly available. Here is the list of contributors in the alphabetic order: Alessandra Bertarini, Nicholas Corey, Yuzhu Cui, Xuan He, Dan Homan, Laura Vega Garcia, Jose-Luis Gomez, Leonid Gurvits, Svetlana Jorstad, Tatiana Koryukova, Sang-Sung Lee, Rocco Lico, Elisabetta Liuzzo, Matt Lister, Alan Marsher, Christopher Marvin, Alexandr Popkov, Alexandr Pushkarev, Eduardo Ros, Tuomas Savolainen, Kirill Sokolovsky, An Tao, Greg Taylor, Alet de Witt, Minghui Xu, and Bo Zhang.

Most of the contributors used AIPS (Greisen 2003) for a priori calibration. By September 24, 2024, the database had 125,623 images of 20,472 sources and this number is growing. For many sources images at different bands and at different epochs are available. An example of an image and a plot of the correlated flux density is shown in Figure 22.

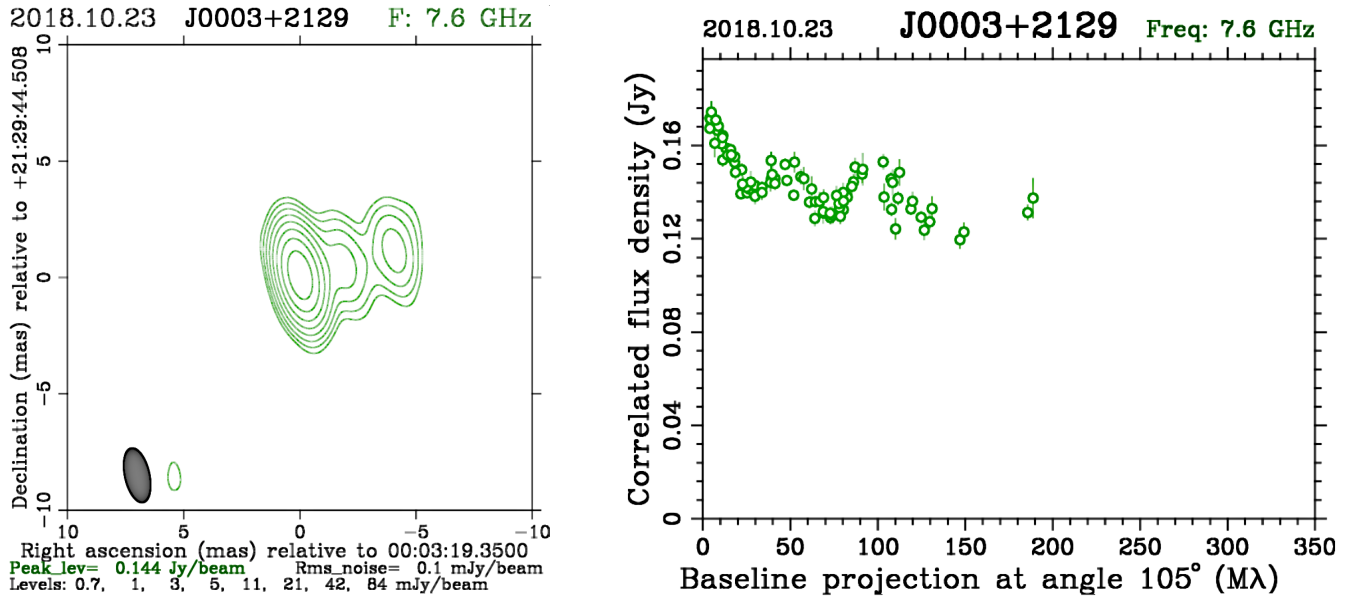


Figure 22. Example of an image and a plot of the correlated flux density with respect to the baseline projection length. The image presented in the left plot is a result of a convolution of the CLEAN component model and the clean beam that is represented by an elliptical Gaussian with the full width half maximum size shown in the left bottom corner. The first contour in the image plot is shown at the 5 times the image rms level. The correlated flux density data points presented in the right plot are calculated as an average per baseline, frequency, and scan, and the error bars accounts for the thermal noise only.

Table 5. Bands names used in this work.

Band	Freq. range GHz
S	2.2–2.4
C	4.1–5.0
X	7.3–8.8
U	15.2–15.5
K	22.0–24.2

The quality and fidelity of source images varies strongly. For sources with 4–6 detections an image has very limited fidelity, often follows the shape of a clean beam, and does not reveal much structure. Estimates of a typical source size and compactness are still possible from calibrated visibility data. On the other hand, images from hundreds of observations have a dynamic range over 1:1000 and provide fine details. The typical image noise rms was 0.3–0.5 mJy for sources observed in 1995–2010. Due to the use of wider bandwidths, the image noise rms reduced and 0.1–0.2 mJy for sources observed in 2015–2022.

5.1. *Correlated flux density at short medium, and long baselines*

The full information about source brightness distributions is contained in images. In order to characterize the source strength in a concise form, we computed the median correlated flux density in three baseline projection length ranges: short (< 1000 km), medium (1000 to 5000 km), and long (> 5000 km). We used calibrated visibility amplitudes after self-calibration and imaging while taking into account data flagging and station-based amplitude correction. The visibility data were averaged in frequency over all IFs and in time over all time epochs of a given image. The correlated flux densities were computed for each band separately. Used band names are presented in Table 5. When images of a given source and a given band are available for more than one epoch, we computed the median flux density values over all visibility datasets related to reconstructed images.

A radio interferometer does not provide the total flux density. The correlated flux density corresponds to a fraction of the total flux density of components with a typical sizes less than 1–5 mas at long baselines, 5–20 mas at medium baselines, and 20–100 mas at short baselines, with an extended emission from components larger than 100–200 mas being lost.

We did not image sources from certain campaigns, for instance many segments of LCS1 and LCS2 campaigns because of scarcity of calibration information. Instead, in most of these cases we performed the non-imaging analysis described in Petrov et al. (2019a). That procedure included three steps: computation of the a priori SEFD using recorded system temperature and prior antenna gain measurements, computation of multiplicative station-dependent gain corrections using publicly available images of calibrator sources, correcting the a priori SEFD, and then computation of the median correlated flux densities.

These correlated flux density estimates are helpful for a coarse assessment of the SNR in future observations. A caution should be exercised in using these estimates. First, for sources with a strong jet or an asymmetric core the correlated flux density strongly depends on the orientation of the baseline projection, whether along the jet or across the jet. In extreme cases the difference can reach a factor of ten. Second, source variability, typical for VLBI-selected AGNs, is expected to change the flux density.

6. THE CATALOGUE

The catalogue consists of three main ASCII tables: the master table, a table with the multi-band positional offsets, and a table with source associations, as well as eight auxiliary tables. Since the number of columns in the three main tables is too large to fit a page width, we do not show them and instead present a description of the variables in the Appendix. The distribution of sources in the catalogue over the celestial sphere in the equatorial coordinate system using the equi-area Hammer projection is shown in Figure 23.

The main master Table 9 presents the source positions from the fused dataset, re-scaled position uncertainties, correlations between right ascension and declination estimates, the number of observations, scans, and sessions used for data analysis, the weighted mean epoch of observations, and three estimates of correlated flux density as a median

Radio Fundamental Catalogue

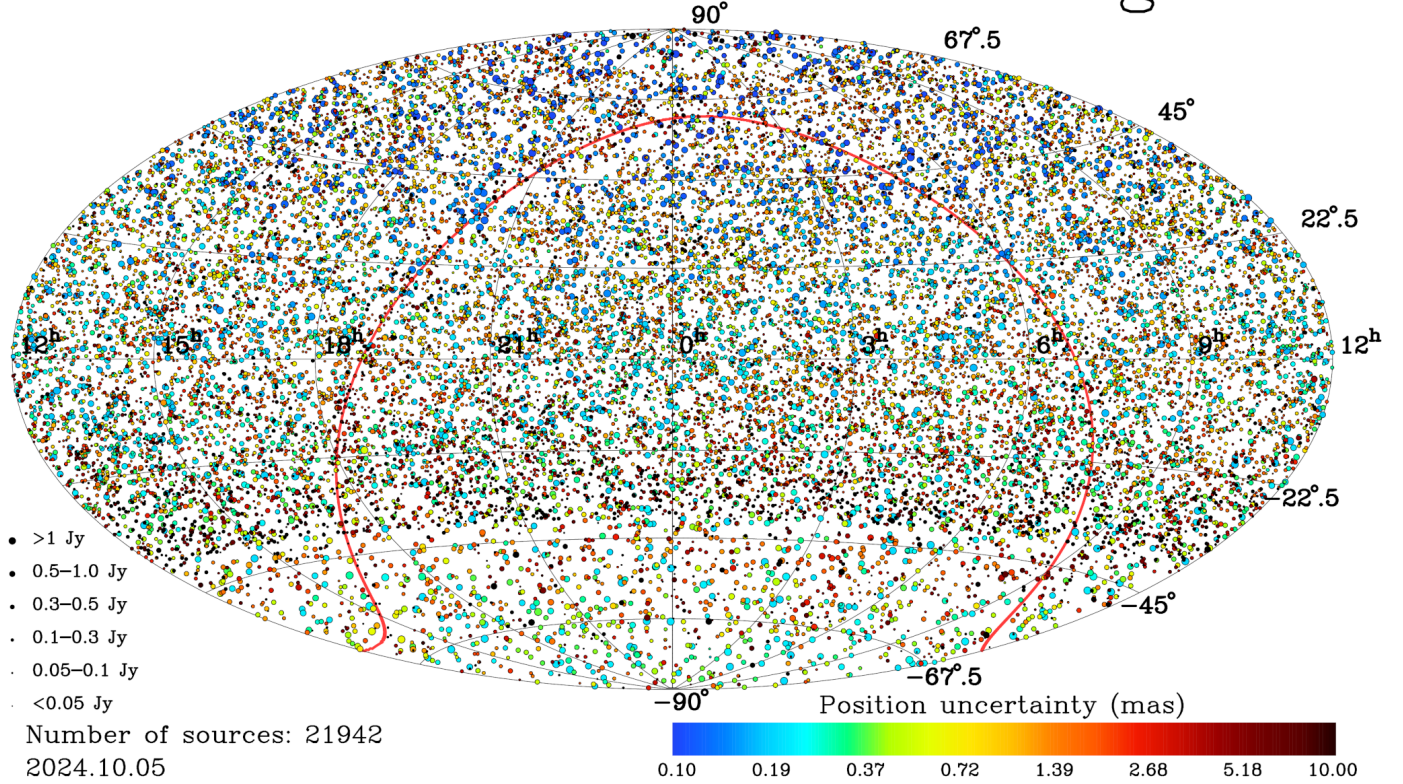


Figure 23. The distribution of RFC sources over the celestial sphere in the equatorial coordinate system. The circle size corresponds to flux density at 8 GHz (or at lower frequencies if a source was not detected at 8 GHz). The circle color corresponds to the semi-major axis of the positional error ellipse. The red line shows the Galactic plane.

in three ranges of baseline length projections at S, C, X, U, and K-bands. See Table 5 for the corresponding band names and frequencies. The epoch of the catalogue to account for precession-nutation: J2000.0, i.e. 2000.01.01, 12 UTC. The epoch of the catalogue to account for galactic aberration, proper motion, and parallax is 2016.0.

Positions derived from the dual-band datasets that include both X/C and X/S data, as well as single band positions at S, C, X, and K-band are presented in the multi-band Table 10 in a form of displacements along right ascension and declination with respect to the positions derived from the fused dataset. Their displacements, position uncertainties, correlation between right ascension and declination estimates, number of sessions, scans, and observations are presented in the multi-band table as well.

The association Table 11 provides the results of cross-matching of the RFC sources with other catalogues, as well as redshifts, source types, and jet directions from literature and NASA/IPAC Extragalactic Database (NED)⁵ Helou et al. (1991) when available. For completeness, we present an auxiliary Table 12 of 20,000 sources that were observed in wide-band high sensitivity VLBI programs at 4–8 GHz, but have not been detected at baselines with projection lengths 100–5000 km. The table shows the upper limit of the correlated flux density of observed sources that are *expected* to be detected within one arcminute of the pointing direction. That limit is set to 20% above the flux density of the faintest sources detected in an experiment that observed a given source. Although a lack of detection should not be construed as an absence of a VLBI source above the specified flux density, this table provides a hint that it is unlikely that strong emission from a mas-scale structure is present in the field.

Since source positional errors range from 0.090 mas to 1480 mas — four order of magnitude, RFC astrometry errors are characterized by the cumulative distributions of semi-minor error ellipse axes and semi-major error ellipse axes

⁵ <https://ned.ipac.caltech.edu/classic>

shown in Figure 24 with green and blue colors, respectively. Table 6 shows three quartiles of the RFC semi-minor and semi-major error ellipse axes.

Table 6. Three quartiles of RFC semi-minor and semi-major positional error ellipse axes in mas.

	σ_{\min}	σ_{\max}
25%	0.23	0.47
50%	0.59	1.37
75%	1.16	2.83

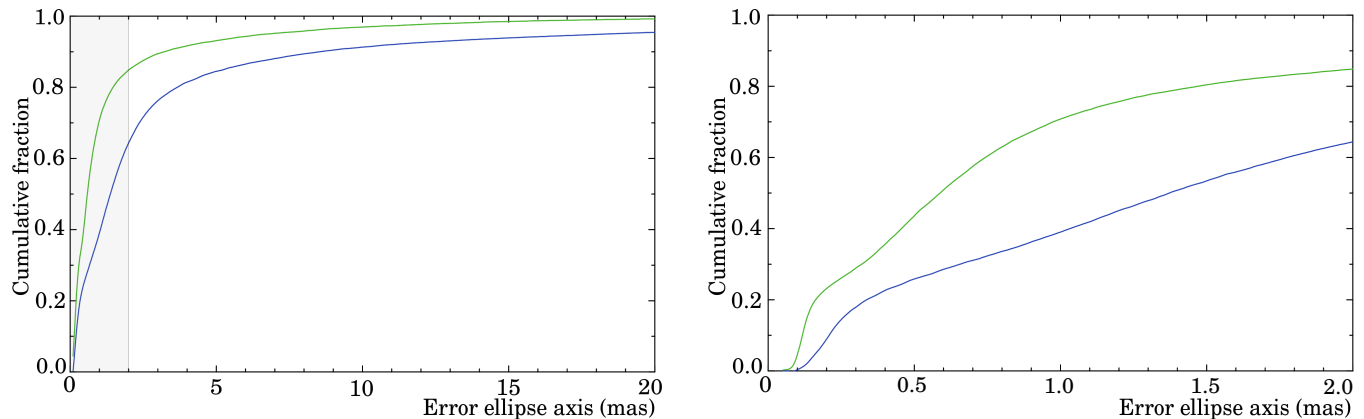


Figure 24. The cumulative error distributions. The upper green line: semi-minor positional error ellipse axes. The lower blue line: semi-major positional error ellipse axes. Right: zoom of the area that is marked with a gray color on the left panel.

Positional accuracy depends on source correlated flux density, array sensitivity, integration time, array geometry, and the number of observations. Left plot in Figure 25 shows the statistics of the number of scans in which individual sources have been observed. We see that roughly 50% of the sources have been observed in one scan. The cumulative distribution of the number of scans flattens beyond 28 scans. There are 1981 sources or 8% that have been observed and detected in 28 or more scans. There are 1483 sources, or 7%, that have been observed in 12 or more sessions. Right plot in Figure 25 show the cumulative distribution of the number of sessions per source. The thin vertical lines show the cutoff — 28 scans and 12 sessions beyond which the cumulative fraction of the number of scans and the number of sessions grow very slowly. These cutoffs roughly correspond to the contribution of geodetic sessions that observe a small subset of sources very often, up to 100,665 scans of RFC J0555+3948 and 12,299 sessions of J1800+7828. From the other hand, approximately 1/2 of sources were observed only in one scan and one session; 2/3 sources were observed in 4 scans or 2 sessions.

An increase of the number of scans and the number of observations reduces the position uncertainties. Figure 26 demonstrates the dependence of semi-major positional error ellipse axes on the number of scans and the number of observations. We see that beyond some limit using more observations does not improve accuracy because of the presence of red noise. Vertical lines in plots show the transition zone from random error dominated to the systematic error dominated: 13–19 scans and 600–850 observations.

It should be noted that the numbers above characterize the observing programs, not the intrinsic property of the VLBI technique. Observations at a different network with a different recording rate would have ended up with other limits of positional errors and the number of scans and observations that are needed to reach these limits.

Figure 27 shows the dependence of the position uncertainties in a form of the semi-major error ellipse axes on the correlated flux density at baselines shorter than 1000 km and at baselines longer than 5000 km. The gray area corresponds to the range of position uncertainties where systematic errors dominates the error budget. The vertical lines denote the flux density that corresponds to a transition from the regime when the contribution of systematic errors dominates to the regime when they do not impact source positions. The blue and green points in Figure 27

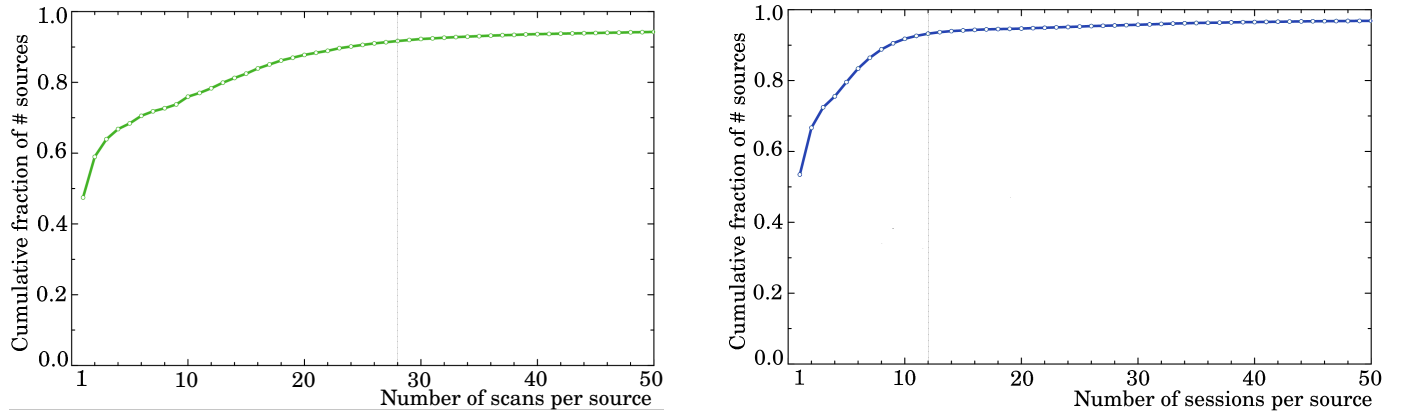


Figure 25. *Left:* the cumulative distribution of the number of scans per source. *Right:* the cumulative distribution of the number of observations per source.

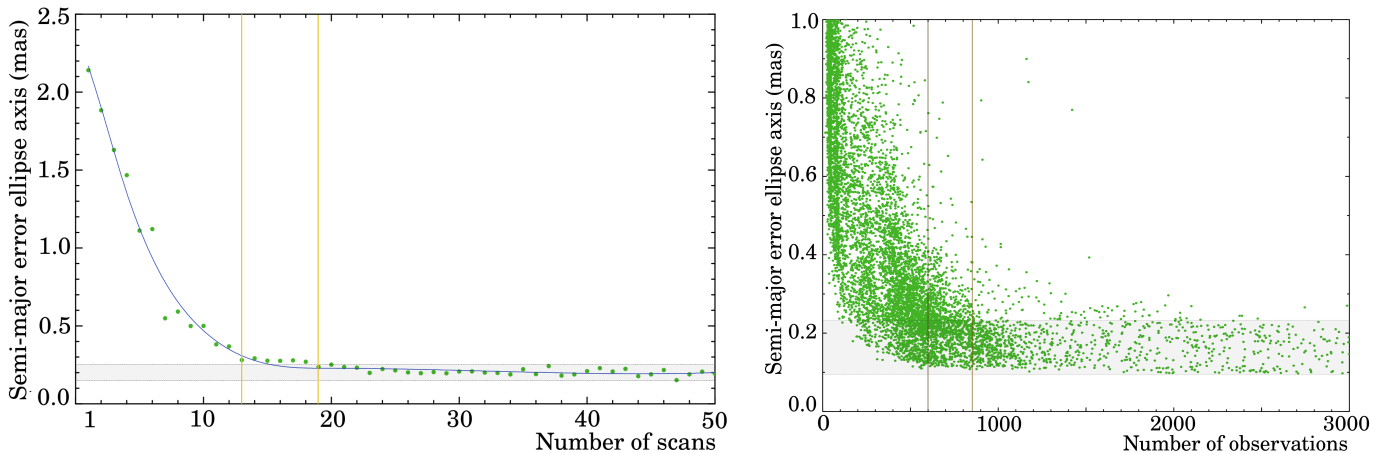


Figure 26. *Left:* the dependence of the median source positional error on the number of scans. *Right:* the dependence of the median source positional error on the number of observations. The gray area denotes the range of position errors dominated by the contribution of systematic errors. Two vertical bars denote the range of the number of scans or the number of observations in a transition zone from random-error dominated to the systematic-error dominated.

correspond to the median correlated flux density at 8 GHz in 10 mJy wide bins. The black line shows the result of smoothing. It follows from these plots that all the sources with the correlated flux density at short baselines greater than 0.16 Jy and at long baselines greater than 0.09 Jy at 8 GHz have position uncertainties dominated by systematic errors. We note that the RFC catalog contains the majority of extragalactic radio sources on the sky with total parsec-scale flux density at 8 GHz above 0.1 Jy because all the sources at declinations $> -40^\circ$ from VLASS catalogue brighter than 0.1 Jy have been observed. Detailed characteristics of the catalog completeness will be analyzed and presented in Paper II.

We can see in Figure 23 that the number of sources at declinations $< -40^\circ$ is low. Figure 28 shows the source density as a function of declination. The density has a jump at $< -40^\circ$. The average source density is 1950 objects per steradian at $\delta > -40^\circ$ and it drops by a factor of 3.0 to 640 objects per steradian at $\delta < -40^\circ$. This jump is due to the cutoff in declination in VLBA surveys, because below that declinations the zone mutual visibility of VLBA becomes small. The decrease of sky density at $\delta > 80^\circ$ is probably due to a statistical fluctuations since the area in high declination zones shrinks as $\cos \delta$. We can also notice that the average positional accuracy in the zone $[-40^\circ, -30^\circ]$ is worse than in other zones because these source were mainly observed with a part of VLBA without northern stations, which detrimentally affected the positional accuracy along the declination axis.

6.1. Naming convention

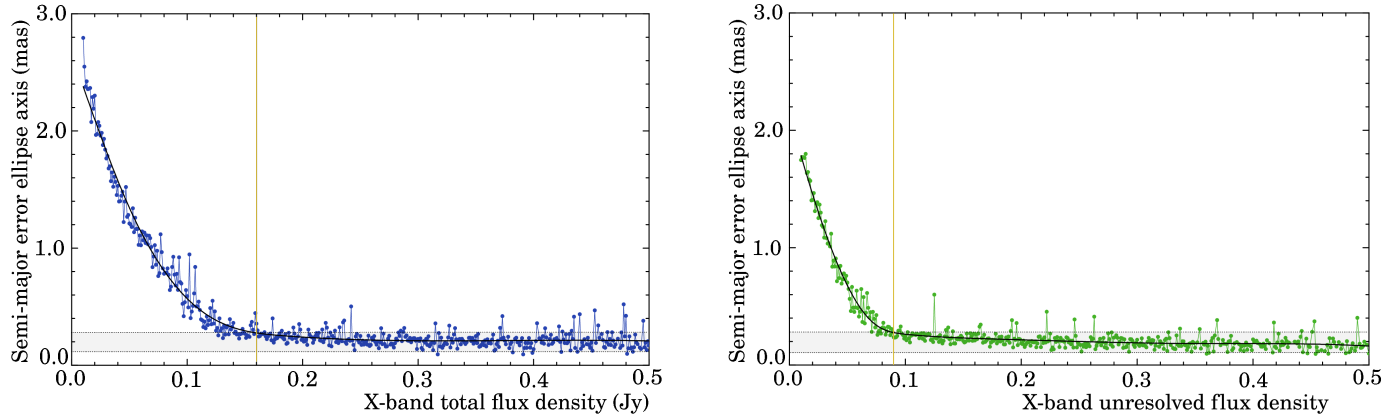


Figure 27. *Left:* the dependence of the median semi-major positional error ellipse on the median flux density at baselines shorter than 1000 km. *Right:* the dependence of the median semi-major positional error ellipse on the median flux density at baselines longer than 1000 km.

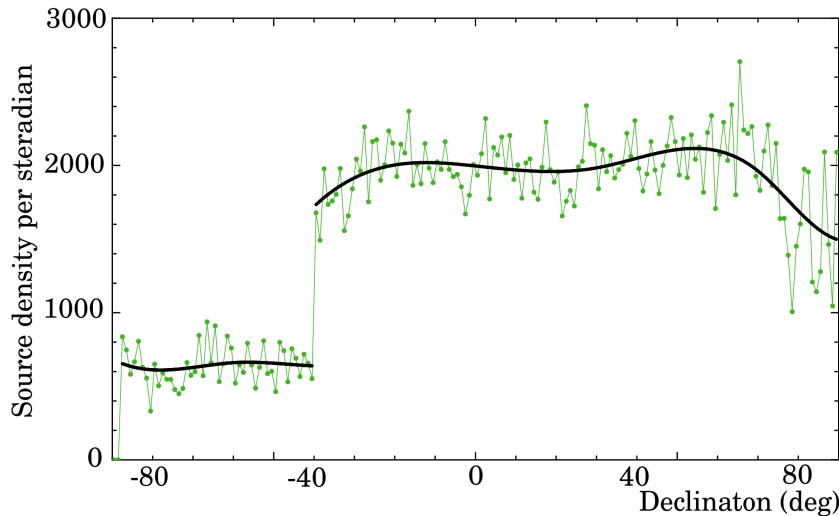


Figure 28. The RFC source density as a function of 1° wide declination stripe zones. The black line shows the source density smoothed using B-spline. Note that the zone area in the stripes depends on $\cos \delta$ which affects statistics close to the poles.

We followed the IAU convention⁶ for naming the sources. The RFC designators refer to the J2000.0 epoch, while the common names refer to the B1950.0 epoch following the tradition established in the 1980s. We assigned new designators and common names for those sources whose positions determined from VLBI observations were not reported in the literature. We did not change names for the sources which positions derived from VLBI observations have already been published. We used the same approach for 10-character long RFC designators (14 character long counting RFC prefix with a following blank) and 8-character long common names. We call those RFC designators that use only the coordinate system prefix J, digits, sign $-$ or $+$, and common names that use digits and sign $-$ or $+$ canonical. When two or more sources occupy the area in the sky that makes names ambiguous, we alter the last character of the name and assign it letter A, B, C, etc. We assigned a letter to a weaker source or a weaker source component. For those multi-component sources that have a sub-component designator known in literature we followed the published notation for sub-components. We call these names as well as names that correspond to a wrong position non-canonical. The Appendix contains Tables 14–15 with 137 non-canonical RFC designators and 427 non-canonical common names.

6.2. Multiple sources

⁶ <https://cds.unistra.fr/Dic/iau-spec.html>

More than one source can be detected in an antenna beam. The component separation procedure that was briefly described in section 3.6 allows us to detect reliably additional strong components at separations of 300 mas and greater. It works less efficiently at separations of 100–300 mas and usually fails at separations shorter than 100 mas. When a source has the second component at an angular distance less than $1''$, we always check the image. In rare cases when we cannot identify the second component in the images, we dropped unconfirmed components from the catalogue. We also dropped the second components with a separation less than 100 mas in rare cases when the component separation procedure ended up with two components. Images of many sources show more than one component, and we set the borderline at 100 mas to discriminate sources with multiple components that are identified on images from objects in which the second or third components have been determined during the astrometric analysis. The success of the component separation procedure depends on the ratio of peak flux density and the number of observations. If the second component is weaker than a factor of 5 and there were fewer than 30 observations of that source used in the solution, it is usually not separated and not reported in the catalogue as a separate source, but it still can be identified on images.

Table 16 in the Appendix presents 104 pairs of sources listed as separate objects in the RFC that are closer than one arcminute. Some of these pairs are known in the literature as gravitational lenses, some are known as AGNs at different redshifts that are just projected close to each others are not gravitationally bound, some sources in gravitationally bound systems, and some of these pairs are different component of the same AGN. We do not attempt to establish the nature of these sources in this study deferring it for future publications.

6.3. *Non-AGNs and nearby sources*

All but 24 sources in the RFC are AGNs. There are 22 stars, including one pulsar, two supernova remnants in the M82 galaxy, and the weak compact object in the center of our Galaxy, Sgr A*. We applied data for parallaxes of radio stars from the *Gaia* EDR3 catalogue when they were available and estimated proper motions of Galactic objects. The estimates of proper motions and their uncertainties from our main solution are presented in Table 7. Proper motion uncertainties were not re-scaled since not enough statistics are collected to make a judgment about validity of uncertainties. Since parallaxes from *Gaia* were used for processing observations of radio stars, the estimates of proper motions are not fully independent with respect to proper motions from *Gaia*.

6.4. *Cross-matching*

We performed cross-matching the RFC list against 14 large surveys listed in Table 8. We evaluated the sky density of a given survey as a number of sources per steradian. For some catalogues the density was considered constant. For other catalogues that have a large number of objects, such as *Gaia*, PanSTARRS (PS1) and ALLWISE, we computed the density on a 3D grid. The first two dimensions are along right ascension and declination, and the third dimension is over magnitude. Knowing the sky density of surveys, we computed the a priori probability of finding a source at a random direction assuming the distribution of sources over the sky or the grid element is uniform. We report all associations with the probability of false positive below 0.01.

This statistical association process is based on the following assumptions: a) an RFC source and its counterpart from a survey have the same position affected only by random positional errors with the second moments reported as uncertainties and b) the sources are distributed uniformly with a known density. Violation of these assumptions cause either missing a counterpart or reporting spurious counterparts.

Figure 29 demonstrates the difficulty of cross-matching. Source J0328+5509 is extended at its VLASS image. The compact component is between two bright extended radio lobes, and the algorithm that identifies point sources may miss it by considering it as a part of a source with a complex structure. Source J2137–1432 has emission at 22 GHz associated with the extended feature of a complex multi-component radiogalaxy.

To assess the impact of clustering, i.e. a deviation of the source distribution from uniform, and determine the a posteriori probability of false association, we rotated the RFC catalogue at random angles within $20\text{--}40'$ and computed the number of associations with the rotated catalogue. Comparing the numbers of these spurious associations with their mathematical expectations, we determined the fudge factor as the ratio of associations to their mathematical expectations based on the a priori probability. We repeated this procedure 1024 times on a grid of the a priori probability of false association. Interpolating this fudge factor as a function of the a priori probability of false association, we are able to generate a list of matches with rather accurate probability of false association. Figure 30 shows these fudge factors for the *Gaia* EDR3 catalogue.

Table 7. Proper motion of Galactic objects

(1)	(2)	(3)	(4)	(5)	(6)	(7)
RFC J0240+6113	star	−1.27	0.10	0.21	0.12	−0.223
RFC J0326+2842	star	52.18	−101.86	0.71	0.67	0.599
RFC J0336+0035	star	−31.22	−157.88	0.23	0.33	0.111
RFC J0535−052E	star	0.85	2.71	1.58	4.94	−0.569
RFC J0535−0523	star	4.41	−3.33	0.20	0.38	0.259
RFC J0835−4510	pulsar	−71.45	29.69	0.41	0.18	−0.237
RFC J0930+4429	star	−2.23	−0.72	3.20	3.07	−0.116
RFC J1055+6028	star	−73.01	−6.96	2.01	1.05	0.715
RFC J1331+1712	star	0.26	1.25	3.06	4.16	0.047
RFC J1406+3539	star	−0.21	−0.11	13.00	13.01	0.000
RFC J1500−0831	star	−65.62	−5.31	0.19	0.34	−0.235
RFC J1501+5619	star	0.06	−2.86	12.68	12.16	0.007
RFC J1534+2330	star	11.41	−0.67	5.90	1.47	−0.111
RFC J1553−2358	star	−14.78	−24.45	0.12	0.13	0.210
RFC J1614+3351	star	−322.20	−87.39	0.11	0.13	0.173
RFC J1745−2900	AGN	−3.58	−5.63	0.07	0.13	0.177
RFC J1818−1214	star	−2.78	−12.33	5.10	6.99	−0.667
RFC J1826−1450	star	8.31	−8.39	0.17	0.35	−0.119
RFC J1911+0458	star	−0.09	0.10	0.11	0.24	−0.281
RFC J2032+4057	star	−3.14	−3.61	0.57	0.47	0.536
RFC J2053+4423	star	35.95	−0.04	1.46	0.56	−0.393
RFC J2349+3625	star	−0.60	−44.54	1.59	1.33	0.089
RFC J2355+2838	star	646.03	34.56	0.54	0.63	−0.025
RFC J0955+6940	SN?	n/a	n/a	n/a	n/a	n/a
RFC J0955+6901	SN	n/a	n/a	n/a	n/a	n/a

NOTE—Column descriptions: (1) the RFC source name; (2) the object type: star, pulsar, or supernova; (3) the proper motion in right ascension in mas/year; (4) the proper motion in declination in mas/year; (5) the uncertainty of the proper motion in right ascension in mas/year without the $\cos \delta$ factor; (6) the uncertainty of the proper motion in declination in mas/year; (7) the correlation between proper motions in right ascension and declination.

Because of poor localization of *Fermi* LAT sources, we used a more sophisticated approach for establishing their association (see for full details Petrov et al. 2013). We determined the likelihood ratios defined as the ratio of the probability that a radio counterpart will be found inside a circle of a given radius to the probability of finding a background radio source with a given flux density or greater outside the same circle.

We report the probabilities of false associations for all the surveys, and set a lower limit of $1 \cdot 10^{-5}$ when our computations show lower probability, arguing that the assumptions that we used for cross-matching are broken for assessing very low probabilities of false association. The summary of cross-matching statistics of the RFC sources are given in Table 8. For *Gaia*, PanSTARRS, and ALLWISE the reported probabilities are a posteriori corrected for clustering. In addition, we added the jet direction angles determined by Plavin et al. (2022), as well as redshift and source type as collected by the NED. We did not validate redshifts and source types, but provided them as is. We should note that a caution should be exercised in using association for the population analysis considering all mentioned factors that can skew the statistics.

7. DISCUSSION

An absolute astrometry catalogue does not depend on the a priori positions of observed sources and the a priori positions of any other sources. A change in the a priori source positions, station positions, and the Earth orientation parameters does not affect the results. To check our software, we performed a test and added the zero mean random

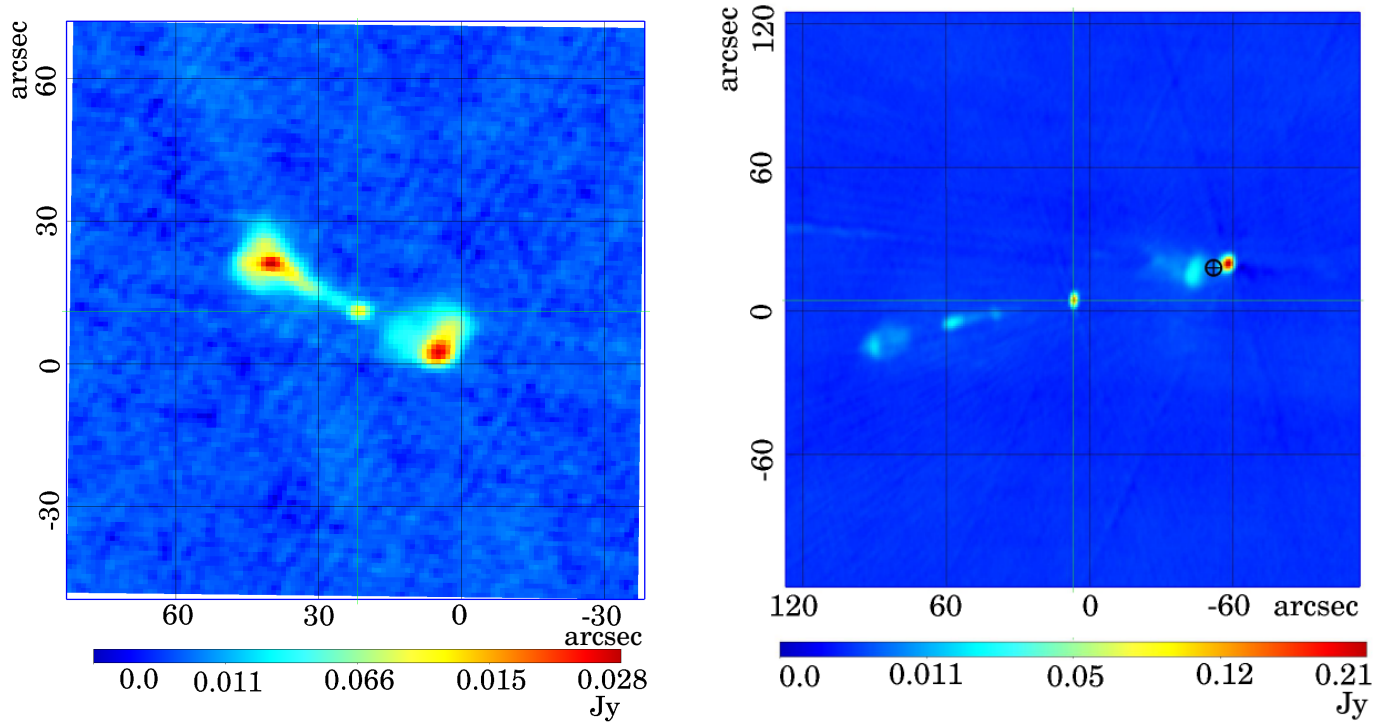


Figure 29. An example of VLASS images of areas in the vicinity of RFC sources. The thin green lines in the image centers show the RFC position. *Left:* RFC J0328+5509. *Right:* RFC J2137-1432. \oplus character denotes the AT20G position.

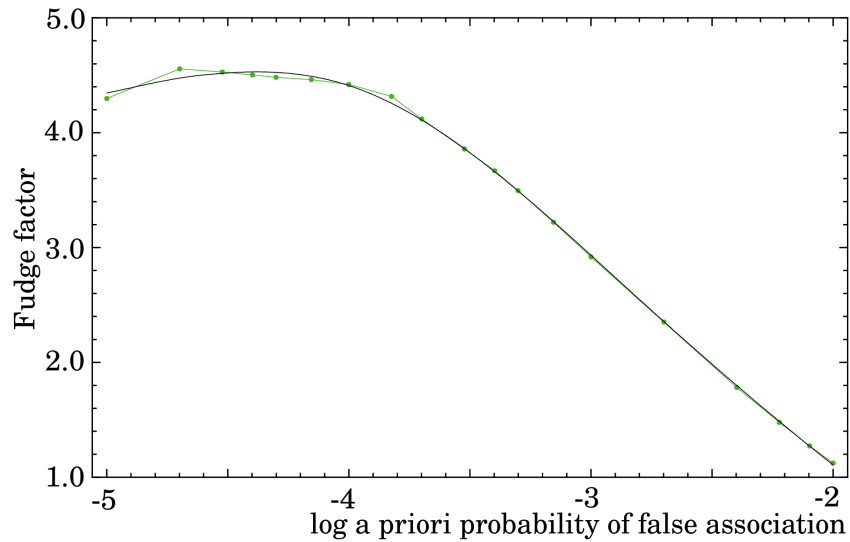


Figure 30. The empirical fudge factors to the a priori estimate of the probability of false association between *Gaia* EDR3 and the RFC catalogue.

noise with the second moments of 100 mas in source positions, 10 cm in station positions and 50 mm/yr to station velocities, and then we ran the solution. The results did not change within rounding errors. The ability to make a totally reference frame free solution is a substantial advance in the field.

The term “fundamental catalogue” coined by Auwers, A., (1879) was originally applied for a catalogue of observations of celestial objects made by absolute methods in right ascensions and declinations. In the past, fundamental catalogues were constructed by weighted combinations of *results* presented in individual absolute astrometry catalogues that were considered the most precise (Fricke 1985). Combining catalogues poses a significant challenge to account for differences

Table 8. Summary of the statistics of association of the RFC sources with 14 large surveys, as well as with the catalogue of jet angles, redshifts, and source types from NED.

Catalogue	Decl. range	Numb assoc	Area	Assoc. fraction	Range	Reference
NVSS	[−40°, 90°]	20186	0.82	98 %	1.4 GHz	Condon et al. (1998)
VLA	[−40°, 90°]	20298	0.82	99 %	2–4 GHz	Gordon et al. (2021)
SUMSS	[−90°, −30°]	2918	0.25	96 %	843 MHz	Bock et al. (1999); Mauch et al. (2003)
TGSS	[−53°, 90°]	17249	0.90	81 %	150 MHz	Intema et al. (2017)
AT20G	[−90°, 0°]	4359	0.50	46 %	5, 8, and 22 GHz	Murphy et al. (2010); McConnell et al. (2012)
<i>Gaia</i> EDR3	[−90°, 90°]	13320	1.00	60 %	400–1000 nm	Lindegren et al. (2021)
PanSTARRS	[−30°, 90°]	14532	1.00	76 %	445–1020 nm	Chambers et al. (2016); Flewelling et al. (2020)
ALLWISE	[−90°, 90°]	15116	1.00	69 %	3.6–22 μm	Wright et al. (2010)
2MASS	[−90°, 90°]	5877	1.00	26 %	1.4–2.2 μm	Skrutskie et al. (2006)
GALEX	[−90°, 90°]	6606	1.00	30 %	134–283 nm	Bianchi et al. (2017)
2RXS	[−90°, 90°]	2640	1.00	12 %	0.1 to 2.4 keV	Boller et al. (2016)
XMMSL	[−90°, 90°]	1657	1.00	7 %	0.1 to 12 keV	XMM-SSC (2018)
1eRASS	[−90°, 42°]	5649	0.50	56 %	0.2–5.0 keV	Merloni et al. (2024)
FERMI LAT	[−90°, 90°]	3272	1.00	14 %	50 MeV to 1 TeV	Abdollahi et al. (2022)
jet angle	[−90°, 90°]	9207	1.00	42 %	n/a	Plavin et al. (2022)
redshift	[−90°, 90°]	8885	1.00	40 %	n/a	NED (Helou et al. 1991)
source type	[−90°, 90°]	10067	1.00	45 %	n/a	NED (Helou et al. 1991)

NOTE—The associations are considered established if the probability of false association is below 0.01. The column Area shows the fraction of the celestial sphere a given catalogue covers. The column Assoc. fraction shows the fraction of the RFC sources that are associated within the area covered by a given catalogue.

(a) 1eRASS covers the area with galactic latitudes $b < 0^\circ$

in data reduction, in systematic errors of individual catalogue, and in assigning correct weights of individual catalogues. This procedure is not transparent, brings an element of subjectivity, and is not equivalent to the best fit of data in the least squares sense. We have overcome these difficulties by combining *all observations* in one least squares solution, leaving no data point behind. We argue that this approach provides the result that is closer to the ideal of the fundamental astronomy than what can be achieved by combining individual catalogues.

An absolute position catalogue has three free rotations, and these rotations cannot be determined from observations in principle. The observations determine a family of solutions that are transformed to each other via a 3D rotation. For convenience, we selected the orientation of the published RFC release to preserve the continuity to the previous versions of the RFC and to the ICRF families of catalogues and its precursors that can be traced back to the 1980s. In particular, the rotation of the RFC with respect to the ICRF3 catalogue is within 0.05 mas. This is a factor of 2–4 less than the contribution of systematic errors in position uncertainties, which are negligible for most of the applications. We should note that the rotation angles are not uniquely defined: they depend on the subset of common sources used for computation of the rotation and on assigned weights. We should point out that the relative rotation of two absolute catalogues is a quantity that does not have a physical meaning. Since the absolute orientation of a catalogue cannot be measured, any inference based on measurable quantities cannot depend on a specific choice of the catalogue orientation.

Absolute astrometry observing programs are rather demanding. The observing programs should be designed in such a way that source positions, station positions, and the Earth orientation be estimated with the highest accuracy. This can be achieved because a) source positions, station positions, and the Earth rotation evolve as slow continuous functions; and b) observing sessions have a significant fraction of overlaps. An overlap in observed sources means that a fraction of sources are observed in different experiments at different epochs, and these sources tie the system of equations together, provided source position evolution is negligible. An overlap in observed stations means arrays of

stations co-observed with other stations at different epochs. Since the model of station position evolution is adjusted, these observations tie all arrays together. An overlap in the Earth orientation means the common stations from all sub-arrays participate in observations dedicated to determination of the Earth orientation within several days of astrometric observations, and the parameters of the Earth orientation tie together geodetic and astrometric observing sessions since the Earth rotation is sufficiently smooth. We exploited the overlaps in the RFC solution explicitly by estimating source positions, parameters of the model of station evolution, and parameters of the mathematical model of the Earth orientation in a single global solution.

An absolute position catalogue defines the reference. That enables differential observations that are much less demanding for their design. Differential observations allow us to determine a positional offset of a target with respect to the reference sources, also known as calibrators. Knowing position of a reference source, we get the position of the target. As we mentioned in the Introduction, the positional error of the target is the sum in quadrature of the uncertainty of the target-calibrator position offset and the reference source position uncertainty. Therefore, characterizing positional errors of absolute astrometry catalogue is very important. We should emphasize that the RFC as well as all other VLBI absolute catalogues is derived from analysis of group delays. The impact of the core-shift on group delays and phase delays is different, and at frequencies below 10 GHz these differences are greater than other systematic errors. When a goal of differential astrometry observations is to analyze just target-calibrator positional offsets, for instance for determination of proper motions and parallaxes, this distinction can be omitted, provided the core-shift remains stable. However, for differential astrometry programs at frequencies below 10 GHz that require high positional accuracy, the core-shift should be determined. The technique of core-shift determination for the purpose of improving differential astrometry results is described in Ding et al. (2024).

The Radio Fundamental Catalogue provides a rich list of objects for phase referencing. The specific criteria for which a given source should satisfy to be considered as a phase calibrator depend on the application. As an example, we considered the following criteria: 1) flux density > 30 mJy at medium or long baselines and 2) semi-major error ellipse < 3 mas. We computed the probability to find a phase calibrator at a grid of $0.25^\circ \times 0.25^\circ$ as a function of the angular distance between target and calibrator on the entire celestial sphere for bands C, X, and K. Due to scarcity of 22 GHz flux density information, we dropped the first criterion for that band. We show the dependencies of these probabilities versus angular distance at zones $[-40^\circ, +90^\circ]$ and $[-90^\circ, -40^\circ]$ in Figure 31. The probability to find a phase calibrator within 2° at C or X band in the first zone is 96–98% and in the second zone is 81%.

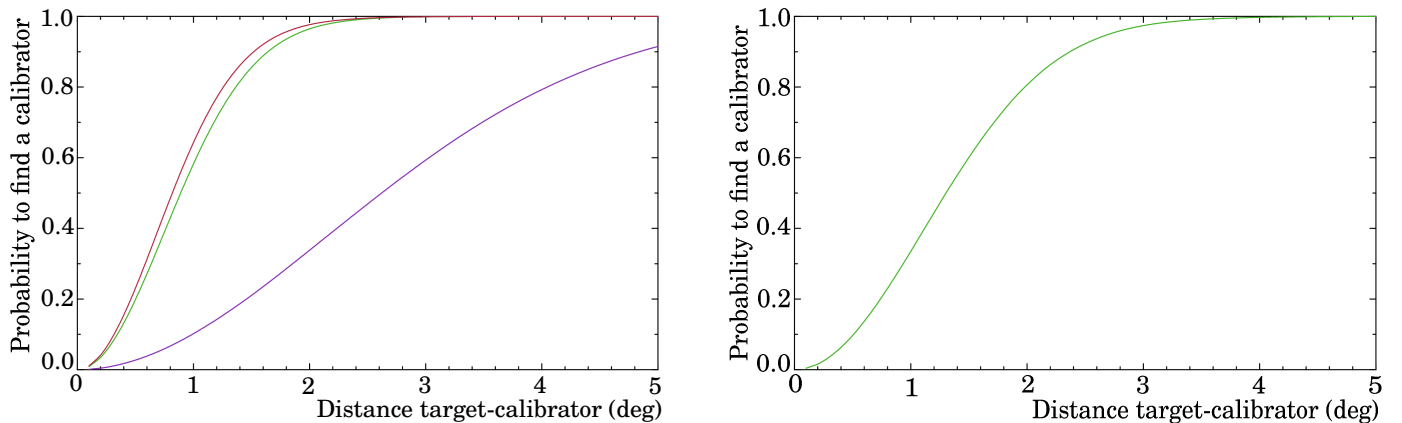


Figure 31. The probability to find a phase calibrator as a function of the angular distance target-calibrator for three bands: C, X, and K. *Left:* zone $[-40^\circ, +90^\circ]$. The upper red curve is for C-band, the middle green curve is for X-band, and the low purple curve is for K-band *Right:* zone $[-90^\circ, -40^\circ]$ for X-band.

Since there is no position catalogue with an accuracy significantly better than the RFC, we have to evaluate its positional accuracy indirectly. We showed that the decimation test provides rather different results depending on the order of splitting the observations into subsets. We interpret this as a consequence of the presence of correlations in the noise. White noise is an idealization that has a limited range of applicability. Figures 5–6 represent the manifestation of the red noise in the data. We used a sophisticated scheme for ad hoc weights update at four levels: 1) the additive weight correction during fringe fitting; 2) the additive elevation-dependent noise in group delays; 3) the additive

elevation-independent noise in group delays; 4) rescaling source positions uncertainties. All these empirical weight updates are made to compensate the impact of the deficiency of our error model. As we showed, one cannot reliably discriminate the error floor from the error scaling factor. We opted to using a hybrid scheme that adjusts error floor using the sources with small positional errors and the scaling factor for the rest of the sources. Here we argue that the scaling factor should not depend on position statistics. Although we can easily interpret the additive noise floor as a manifestation of errors that are independent of the observations, e.g. atmospheric path delay, or the source structure contribution, we cannot offer a simple interpretation for the scaling factor. We consider that relatively small scaling factors of 1.08 and 1.16 for right ascension and declination is a sign of an improvement of the error model.

The presence of a relatively large declination-dependent error floor in the range of 0.04 to 0.22 mas is somewhat disappointing. It is greater than the 0.03 and 0.05 mas floor reported in literature in the past (Charlot et al. 2020). This does not reflect a deficiency in our data analysis strategy that would have added an extra noise, but reflects our diligence in accounting for the red noise that was not considered in prior publications. The presence of the red noise has a critically important implication. When only the white noise affects observations, position accuracy improves indefinitely with an increase of the number of observations. In the presence of correlation, or using an equivalent formulation, the red noise, positional accuracy is approaching a limit with an increase of the number of observations, and upon reaching that limit does not grow any more.

A detailed investigation of the origin of the red noise goes well beyond the scope of this article. Three factors certainly play a role: 1) deficiency of the modeling path delay in the neutral atmosphere; 2) lack of modeling source structure contribution; and 3) mismodeling path delay in the ionosphere when processing single-band delay data. In Petrov (2024) we provided a detailed argumentation in favor of these factors.

It was known for decades that positions of radio sources exhibit changes at a level of tenths of a milliarcsecond (e.g. Ma & Shaffer 1991). These changes are not entirely random, but have a systematic component that in some cases is related to a flaring activity. This systematic component makes position changes correlated. The disparity of the global versus local floor-scale diagrams in Figures 5–6 is explained by these correlations. Although coordinate estimates determined over a short period time may characterize the source position over that period more precisely when very bright sources are observed, determination of epoch-based positions and their covariances poses a number of challenges. An epoch-based positional offset depends not only the contribution of random errors affecting a given source, but also on positional offsets of other sources observed in that experiment, which cause an additional network jitter. Position estimates are connected either explicitly through epoch-based net-rotation constraints, or implicitly by fixing positions of some sources. A typical number of observations in a given astrometry session is several hundreds, compare with a total number of 22 thousands sources. The observed jitter will be a superposition of the jitter caused by source structure, a network position jitter, and the jitter caused by propagation delay. The problem of separation of these contributions is not yet solved, as we can see from the recent work of Cigan et al. (2024): the excessive noise in source position time series over declination is roughly twice larger than over right ascension, which implies that *on average*, the observed jitter is dominated by mismodeling atmospheric path delay. The Radio Fundamental Catalogue provides the time averaged positions for the reported weighted mean epochs and serves as a reference for characterizing deviations with respect to the mean.

Comparison of the RFC with *Gaia* shows a significant improvement in the agreement of the normalized position differences with respect to early publications. We attribute this improvement to enhancements in the VLBI source positional error model, which made it more realistic. Analysis of the position difference leads us to the conclusion that both RFC and *Gaia* EDR3 error models are accurate to at least the 20% level. We cannot estimate the accuracy of the error model with a greater confidence because the *Gaia* positional errors are affected by the presence of optical jets that systematically shift the position of a *Gaia* centroid along the jet directions with respect to the center engine. Our comparison revealed the presence of the extra noise in *Gaia* EDR3 reflected as an increase of the χ^2/ndf quantity, and the presence of the elevation-dependent noise in the RFC that is more noticeable for sources that had fewer than 120 observations.

7.1. *The historical context of VLBI surveys*

Since the first pioneering work of Cohen & Shaffer (1971) that has demonstrated the use of VLBI for astrometry, further progress in VLBI astronomy evolved following four routes.

The first route is running pathfinder surveys. The goal of these surveys was to find compact sources and measure their correlated flux densities. Using the Deep Space Network, Morabito et al. (1982, 1983); Wehrle et al. (1984);

Morabito et al. (1985); Preston et al. (1985); Morabito et al. (1986) observed over 1500 targets at 2.3 and 8.6 GHz and have detected over 1000 objects. Using these surveys, positions of 323 sources were determined with an accuracy of 300–1000 mas. These surveys were not designed for astrometry and used a narrow bandwidth. This explains their low positional accuracy. Visibility data from these campaigns were not made publicly available and are not used in the RFC. The development of the VLBA in the 1990s made it possible to run large VLBI surveys. It was realized that when observations are made using a spanned bandwidth over 500 MHz, positional accuracy at the milliarcsecond level can be achieved.

The development of the Mark III recording system (Clark et al. 1985) allowed astronomers to record a spanned bandwidth of 360 MHz and later 720 MHz. That made it possible to re-observe the sources detected in pathfinder surveys and determine their positions with a sub-milliarcsecond level of accuracy. Ma et al. (1986) published the first absolute astrometry catalogue based on a wide-band system using observations collected under geodetic VLBI programs. Following that route, a number of observing sessions with expanded source lists were conducted. The outcome of these experiments were catalogues of sources with a milliarcsecond level precision that were disseminated in the IERS annual reports (Arias et al. 1995). Based on these observing programs, the ICRF1 absolute astrometry catalogue was published (Ma et al. 1998). Following that route, a large number of observing programs was organized. Several astrometric multi-program solutions were published, among them, ICRF2 (Fey et al. 2015), ICRF3 (Charlot et al. 2020), and WFCS (Petrov 2021).

With the development of the hybrid imaging algorithms (Readhead & Wilkinson 1978; Cotton 1979), it became possible to use VLBI for making images of observed radio sources. VLBI image surveys starting with the work of Pearson & Readhead (1988), which marked the third route of evolution of VLBI astronomy. A number of imaging survey followed. We mentioned here the two largest surveys: VIPS (Helmboldt et al. 2007) and 2 cm VLBA / MOJAVE (Kellermann et al. 1998; Lister et al. 2018), with 1119 and 623 sources, respectively. Although astrometric VLBI observations can be used for imaging (e.g., Piner et al. 2012; Pushkarev & Kovalev 2012), and imaging experiments could be used for astrometry and geodesy (see, for example, Krásná & Petrov 2021), these programs ran rather independently. In imaging experiments IFs are usually allocated contiguously, and that significantly reduces the astrometric accuracy. Astrometric programs often did not have a good amplitude calibration, what made imaging challenging and resulting flux density scale inaccurate. We should note that since 2020s all these three routes have a tendency to converge since the total bandwidth substantially increased, and even contiguous IF allocation provides wide enough spanned bandwidth for the precise group delay determination.

In Figure 32 we showed the growth of the number of sources in the RFC online releases (green line) and in other multi-program catalogues (blue line) shown as a reference.

For completeness, we should mention the fourth route: differential astrometry. Observing a pair of a calibrator and a target, atmospheric path delay contribution can be reduced roughly as a target-calibrator separation expressed in radians. This allows one to achieve the accuracy of the displacement of a target with respect to a calibrator at the level of 0.03 mas (Reid & Honma 2014). A target can be very weak, since it still can be detected using a long integration time. Deller & Middelberg (2014) published a large mJIVE-20 survey of 4336 sources detected using differential astrometry at 1.4 GHz. Only 73 sources from mJIVE-20 are common with the RFC. The median reported positional accuracy of mJIVE-20 is 0.7 mas. Systematic errors caused by the core-shift at L-band are expected to contribute at the level of 2 mas (Sokolovsky et al. 2011; Ding et al. 2024). We do not include this program in the RFC because mJIVE-20 does not fall into a category of absolute astrometry.

7.2. Future development

Undoubtedly, applying the source structure contribution in data reduction and refining models of atmospheric path delay will improve accuracy. Although as Thomas (1980) showed, computation of source structure contribution from source images is relatively straight-forward, logistically, this problem is very time consuming. That is why little progress in this area has been achieved for over four decades. Nevertheless, the availability of over 10^5 VLBI images brings certain optimism that some day in the future applying source structure contribution will become routine. In Petrov (2024) we showed that *on average*, the source structure contributes to source positional errors at a level of 0.05–0.07 mas per component, right ascension and declination.

We should acknowledge that our use of a sophisticated error re-scaling scheme is a reflection of the basic flaw in the current paradigm of space geodesy that uses the a priori weight matrices with zero off-diagonal terms, which implies the noise is uncorrelated, i.e. white. We envisage that the full covariance matrices of the noise in group delay observables

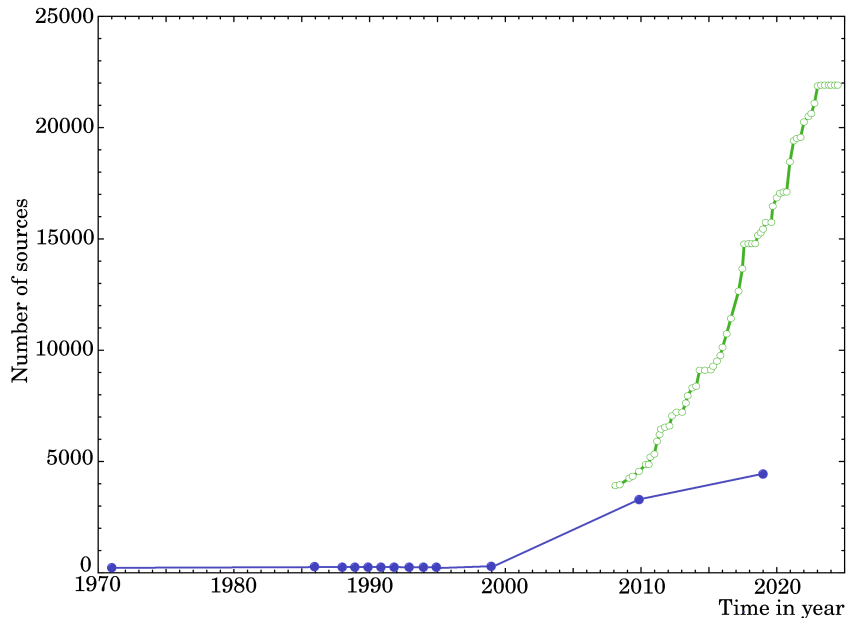


Figure 32. The evolution of the VLBI absolute astrometry catalogues. The green circles show releases of the RFC. The blue circles show the historical VLBI position catalogues: (Cohen & Shaffer 1971) followed by (Ma et al. 1986), the IERS series of source catalogues, then ICRF1, ICRF2, and ICRF3.

will be used in the future in line with ideas of Halsig et al. (2019) or similar. That will allow us to develop a robust error model without resorting to the use of the empirical floor and scaling factors. This model, in turn, will allow us to predict better positional errors from planned observations and optimize the observing strategy accordingly.

We do not envisage that the number of sources with positions determined with VLBI in the absolute astrometry mode will be improved significantly, i.e. by a factor of 1.5 or greater in the next 10–15 years because there is no planet-wise resource to perform such a program. Therefore, we anticipate that future observing programs will focus primarily on sources whose positions we want to improve. Beyond the 10–15 year horizon, new high sensitivity instruments, such as SKA and ngVLA will become operational and likely new observational programs for a support of these facilities will be initiated, either in the absolute or differential astrometry mode.

Re-observations of all the sources which were observed within one scan only in pathfinder VLBI surveys in four to six scans would improve their position uncertainties one order of magnitude down to the 0.2–0.5 mas level and significantly improve fidelity of reconstructed images needed for the source structure modeling. Because of a lack of resources to re-observe all the RFC sources with a positional accuracy worse than 0.2 mas before the SKA and ngVLA era, the priorities should be established. As we have shown, additional observations improve position accuracy only up to a certain limit. Unfortunately, this consideration was not always taken into account in the past, and we hope the situation will be improved in the future. We see several areas where new observations will have a big impact.

First, there are certain areas on the sky that are more frequently observed. These are the ecliptic band and the area close to the Galactic plane. The first area is of a great importance for space navigation and for planned observations of radio beacons on the Moon and other Solar system bodies. Many perspective calibrator sources have the positional accuracy of a factor of 3 to 10 above the limit set by the presence of the red noise. The areas in the Galactic plane are important for measurement of parallaxes and proper motions. Observations of targets in the vicinity of the Galactic plane at 23 GHz are advantageous because at this frequency the impact of scattering in the interstellar medium is significantly reduced.

Second, the positional accuracy of objects in the Southern Hemisphere not reachable by the VLBA can be improved by dual-band or quad-band observations with the LBA, and planned IVS radio telescopes in Thailand, Malaysia, and Indonesia, as well as the African VLBI network. With the on-going development of the Thai National VLBI Array (TVA) in Thailand (Sugiyama et al. 2024) and the South-East Asian VLBI Network (SEAVN) new opportunities for dedicated astrometric programs targeting the Southern Hemisphere are expected to emerge. Currently, most of RFC sources at declinations below -40° have been observed at X-band only, which limits the positional accuracy.

Third, a number of sources with a peculiar structure, such as visual doubles, or those showing an indication of a complex structure in existing images can be re-observed using more scans per source in order to provide high fidelity images, to establish their nature, and to improve their positions by applying source structure.

8. SUMMARY AND OUTCOMES

We present a catalogue of absolute positions and correlated flux densities of 21,942 sources detected with VLBI. All of them, but 24, are AGNs. This is a result of analysis of 17 thousand hours of VLBI observations dedicated for astrometry and 194 thousand hours dedicated for geodesy since 1980 through 2024. We used virtually all suitable publicly available VLBI observations to date in our analysis. Source position uncertainties range from 0.09 to 1480 mas with the median semi-minor and semi-major error ellipse axes 0.6 and 1.4 mas, respectively.

The Radio Fundamental Catalogue increases the number of sources reported in prior VLBI catalogues that accumulated data from historical observing programs by a factor of 5. It provides positions of all the sources reported in prior absolute astrometry VLBI catalogues with significantly improved positional accuracy and more realistic reported uncertainties. The Radio Fundamental Catalogue is accompanied with a collection of over 125,000 images of observed radio sources, cross-matches against 14 large surveys, sources properties collected by the NED, including redshifts for 1/3 of the objects, and jet directions reported in literature.

An advanced error model that accounts for the contribution of red noise is developed for the derivation of the Radio Fundamental Catalogue. Comparison of the Radio Fundamental Catalogue with the *Gaia* EDR3 catalogue in the optical range demonstrates a significant improvement in the agreement of the normalized arc length position difference with respect to prior publications. This comparison sets the upper limit of inaccuracy of the Radio Fundamental Catalogue error model: 20%.

Considering all these factors, we position the Radio Fundamental Catalogue as a new standard in VLBI radio astrometry that overrides previous catalogues used for realization of the celestial reference frame. The Radio Fundamental Catalogue is the most complete catalogue that provides milliarcsecond level accurate positions and correlated flux densities based on analysis of VLBI observations. The catalogue establishes the foundation for space geodesy, space navigation, differential astrometry, AGN jet and scattering studies, as well as population analysis in radio astronomy.

The first version of the catalogue became available online on February 12, 2008. Since then the catalogue is updated on a quarterly basis, and it will be updated with a three months cadence in the future. Each the catalogue release has a notation `rfc.yyyys`, where `yyyy` is the year and `s` is a suffix: `a`, `b`, `c`, or `d`. In each update cycle the astrometric solutions that use all the data since 1980 through present are updated. Each update includes fixes in prior experiments and incorporates new experiments. The new versions of the catalogue will be available at <https://doi.org/10.25966/dhrk-zh08>.

ACKNOWLEDGMENTS

This work was done using only the following publicly available datasets

1. collected with the VLBA network of the NRAO and available <https://data.nrao.edu/portal/>;
2. collected with the IVS network and available at the NASA Crustal Dynamics Data Informational System (CDDIS) <https://cddis.nasa.gov/archive/vlbi/>;
3. collected with the LBA network and available at <https://atoa.atnf.csiro.au>
4. collected with the EVN network and available at <http://archive.jive.nl/scripts/portal.php>;
5. collected at the EAVN network and available at <https://radio.kasi.re.kr/arch/search.php>
6. collected at the KVN network and available at <https://radio.kasi.re.kr/arch/search.php>
7. collected at the KaVa network and available at <https://radio.kasi.re.kr/arch/search.php>
8. collected at the VERA network and available at upon request to vera-contact@ml.nao.ac.jp
9. collected at the CVN network and available at upon request to sfc@shao.ac.cn

The NRAO is a facility of the National Science Foundation operated under cooperative agreement by Associated Universities, Inc. The author acknowledges use of the VLBA under the USNO's time allocation for some datasets. The Long Baseline Array is part of the Australia Telescope National Facility (<https://ror.org/05qajvd42>) which is funded by the Australian Government for operation as a National Facility managed by CSIRO. The European VLBI Network is a joint facility of independent European, African, Asian, and North American radio astronomy institutes. This

work is made use of the East Asian VLBI Network (EAVN), which is operated under cooperative agreement by National Astronomical Observatory of Japan (NAOJ), Korea Astronomy and Space Science Institute (KASI), Shanghai Astronomical Observatory (SHAO), Xinjiang Astronomical Observatory (XAO), Yunnan Astronomical Observatory (YNAO), National Astronomical Research Institute of Thailand (Public Organization: NARIT), and National Geographic Information Institute (NGII), with the operational support by Ibaraki University (for the operation of Hitachi 32-m and Takahagi 32-m telescopes), Yamaguchi University (for the operation of Yamaguchi 32 m telescope), and Kagoshima University (for the operation of VERA Iriki antenna). We are grateful to the staff of the KVN who helped to operate the array and to correlate the data. The KVN and a high-performance computing cluster are facilities operated by the Korea Astronomy and Space Science Institute (KASI). The KVN observations and correlations are supported through the high-speed network connections among the KVN sites provided by the Korea Research Environment Open NETwork (KREONET), which is managed and operated by the Korea Institute of Science and Technology Information (KISTI). We would like to thank all staff members of the VERA stations and the Mitaka correlation center for their assistance in the observations. This research has made use of data from the MOJAVE database that is maintained by the MOJAVE team (Lister et al. 2018). This research has made use of the NASA/IPAC Extragalactic Database (NED), which is funded by the National Aeronautics and Space Administration and operated by the California Institute of Technology.

L.Y.P was supported in part by the NASA Space Geodesy Project. Y.Y.K was supported by the MuSES project which has received funding from the European Research Council (ERC) under the European Union’s Horizon 2020 Research and Innovation Programme (grant agreement No 101142396). We certify that no machine learning or artificial intelligence techniques were used neither during data analysis, nor in manuscript preparation.

The work on the Radio Fundamental Catalogue commenced in 2000. For the course of twenty four years we got help and good advice from many colleagues. It is our pleasure to acknowledge Walter Alef, Karen Baver, Simone Bernhart, Alessandra Bertarini, Chirsian Bizouard, Johannes Böhm, Sergei Bolotin, Geraldine Bourda, Walter Brisken, Yoon Kyung Choi, Brian Corey, Nicholas Corey, Bill Cotton, Yuzhu Cui, Adam Deller, Philip Edwards, Martine Feissel, Alan Fey, Ed Fomalont, Laura Vega Garcia, John Gipson, Jose-Luis Gomez, Anne-Marie Gontier (deceased), David Gordon, Jakob Gruber, Sergei Gulyaev, Vadim Gubanov (deceased), Leonid Gurvits, Rudiger Haas, Xuan He, Dan Homan, Mareki Honma, Christopher Jacobs, Frederic Jaron, Megan Johnson, Michael Johnson, Svetlana Jorstad, Taehyun Jung, Nikolai Kardashev (deceased), Ken Kellermann, Segei Klioner, Leonid Kogan (deceased), Tetsuro Kondo, Tatiana Koryukova, Yuri A. Kovalev, Georgiy Krasinski (deceased), Hana Krasna, Thomas Krichbaum, Sergei Kurdubov, Sang-Sung Lee, Jeong Ae Lee, Rocco Lico, Elisabetta Liuzzo, Matt Lister, Andrei Lobanov, Chopo Ma, Lucia McCallum, Seiji Manabe, Dan MacMillan, Alan Marscher, Iván Martí-Vidal, Christopher Marvin, Leonid Matveenko (deceased), Alexey Melnkiov, Cristina Garcia Miro, Arthur Niell, Jim Moran, Ramesh Narayan, Axel Nothnagel, Kristina Nyland, Chris Phillips, Alexandr Plavin, Christian Ploetz, Sergei Pogrebenko, Alexandr Popkov, Richard Porcas, Alexandr Pushkarev, Cormac Reynolds, María Rioja, Eduardo Ros, Jim Ryan (deceased), Tuomas Savolainen, Fengchun Shu, Kirill Sokolovsky, Frank Schinzel, Harald Schuh, An Tao, Greg Taylor, Paulo Tomassi, Rene Vermeulen, Petr Voitsik, Jan Wagner, Alet de Witt, Craig Walker, Minghui Xu, Shuangjing Xu, Elenonora Yagudina, J. Anton Zensus, and Bo Zhang.

A significant part of the work was done at nights, weekends, and vacation. We thank our families for understanding and ask for forgiveness.

APPENDIX

The Radio Fundamental Catalogue main master Table 9, the Table 10 with dual-band and single-band source positions, and the cross-matching Table 11 are too wide to be shown here. They are presented as machine readable tables only.

The samples of the Table 13 with the parameters of the error floor as a function of declination for right ascension, the Table 14 of non-canonical RFC designator, the Table 15 of non-canonical common names, the Table 16 of close source pairs, the Table 12 with the list of source that were observed, but have not detected, the Table 17 of the names and dates of astrometric experiment names, the Table 18 of geodetic 24 hr experiment names, and the Table 19 of geodetic 1 hr experiment names are shown in the appendix. They are published entirely in the machine-readable format.

Table 9. Column description of the main master table with the Radio Fundamental Catalogue^a.

#	Unit	Label	Description
1	—	Name	RFC object designator. A 10 character long J2000-name with prefix RFC
2	—	Comnam	Common name
3	h	RAh	Hours of Right Ascension (J2000)
4	min	RAm	Minutes of Right Ascension (J2000)
5	s	RAs	Seconds of Right Ascension (J2000)
6	—	DE-	Sign of the Declination (J2000)
7	deg	DEd	Degrees of Declination (J2000)
8	arcmin	DEm	Arcminutes of Declination (J2000)
9	arcsec	DEs	Arcseconds of Declination (J2000)
10	mas	eRA	Error in right ascension without $\cos \delta$ factor
11	mas	eDE	Error in declination
12	—	Corr	Correlation between right ascension and declination
13	—	Nobs	Number of observations used in the fused solution
14	—	Nsca	Number of scans used in the fused solution
15	—	Nses	Number of observing sessions used in the fused solution
16	Jy	FsS	Median flux density at S-band, [2.2, 2.4] GHz, at baseline projection lengths shorter than 1000 km ^b
17	Jy	FmS	Median flux density at S-band, [2.2, 2.4] GHz, at baseline projection lengths in the range 1000 to 5000 km
18	Jy	FIS	Median flux density at S-band, [2.2, 2.4] GHz, at baseline projection lengths longer than 5000 km ^c
19	Jy	FsC	Median flux density at C-band, [4.3, 5.1] GHz, at baseline projection lengths shorter than 1000 km ^b
20	Jy	FmC	Median flux density at C-band, [4.3, 5.1] GHz, at baseline projection lengths in the range 1000 to 5000 km
21	Jy	FIC	Median flux density at C-band, [4.3, 5.1] GHz, at baseline projection lengths longer than 5000 km ^c
22	Jy	FsX	Median flux density at X-band, [7.3, 8.6] GHz, at baseline projection lengths shorter than 1000 km ^b
23	Jy	FmX	Median flux density at X-band, [7.3, 8.6] GHz, at baseline projection lengths in the range 1000 to 5000 km
24	Jy	FIX	Median flux density at X-band, [7.3, 8.6] GHz, at baseline projection lengths longer than 5000 km ^c
25	Jy	FsU	Median flux density at U-band, [15.2, 15.5] GHz, at baseline projection lengths shorter than 1000 km ^b
26	Jy	FmU	Median flux density at U-band, [15.2, 15.5] GHz, at baseline projection lengths in the range 1000 to 5000 km
27	Jy	FIU	Median flux density at U-band, [15.2, 15.5] GHz, at baseline projection lengths longer than 5000 km ^c
28	Jy	FsK	Median flux density at K-band, [23.2, 24.2] GHz, at baseline projection lengths shorter than 1000 km ^b
29	Jy	FmK	Median flux density at K-band, [23.2, 24.2] GHz, at baseline projection lengths in the range 1000 to 5000 km
30	Jy	FIK	Median flux density at K-band, [23.2, 24.2] GHz, at baseline projection lengths longer than 5000 km ^c
31	yr	MeaEpo	Weighted mean epoch of observations

(a) Table 9 is too wide to be shown here. It is published in the machine-readable format only as file rfc.txt.

(b) Represent an estimate of the flux density integrated over VLBI image.

(c) Represent an estimate of the unresolved flux density of VLBI image.

(d) -9.99 indicates a Null value: no estimate is available.

Table 10. Column description of the table with source positions from dual-band, S-band, C-band, X-band, and K-band as differences with respect to the RFC positions derived from analysis of the fused group delays^a.

#	Unit	Label	Description
1	—	Name	RFC object designator. A 10 character long J2000-name with prefix RFC
2	mas	eRA	Error in right ascension without $\cos \delta$ factor applied
3	mas	eDE	Error in declination
4	—	Nobs	Number of observations used in the fused solution
5	—	Nsca	Number of scans used in the fused solution
6	—	Nses	Number of observing sessions used in the fused
7	mas	dxD	Offset of the dual-band position along the right ascension axis without $\cos \delta$ factor applied with respect to the position from the fused solution
8	mas	dyD	Offset of the dual-band position along the declination axis with respect to the position from the fused solution
9	mas	exD	Uncertainty of the dual-band position along the right ascension axis without $\cos \delta$ factor applied
10	mas	eyD	Uncertainty of the dual-band position along the declination axis
11	—	CorrD	Correlation between right ascension and declination of the dual-band source position
12	—	NobsD	Number of observations used in the dual-band solution
13	—	NscaD	Number of scans used in the dual-band solution
14	—	NsesD	Number of observing sessions used in the dual-band solution
15	mas	dxS	Offset of the S-band position along the right ascension axis without $\cos \delta$ factor applied with respect to the position from the fused solution
16	mas	dxS	Offset of the S-band position along the declination axis with respect to the position from the fused solution
17	mas	exS	Uncertainty of the S-band position along the right ascension axis without $\cos \delta$ factor applied
18	mas	eyS	Uncertainty of the S-band position along the declination axis
19	—	CorrS	Correlation between right ascension and declination of the S-band source position
20	—	NobsS	Number of observations used in the S-band solution
21	—	NscaS	Number of scans used in the S-band solution
22	—	NsesS	Number of observing sessions used in the S-band solution
23	mas	dxC	Offset of the C-band position along the right ascension axis without $\cos \delta$ factor applied with respect to the position from the fused solution
24	mas	dyC	Offset of the C-band position along the declination axis with respect to the position from the fused solution
25	mas	exC	Uncertainty of the C-band position along the right ascension axis without $\cos \delta$ factor applied
26	mas	eyC	Uncertainty of the C-band position along the declination axis
27	—	CorrC	Correlation between right ascension and declination of the C-band source position
28	—	NobsC	Number of observations used in the C-band solution
29	—	NscaC	Number of scans used in the C-band solution
30	—	NsesC	Number of observing sessions used in the C-band solution
31	mas	dxX	Offset of the X-band position along the right ascension axis without $\cos \delta$ factor applied with respect to the position from the fused solution
32	mas	dyX	Offset of the X-band position along the declination axis with respect to the position from the fused solution
33	mas	exX	Uncertainty of the X-band position along the right ascension axis without $\cos \delta$ factor applied

Table 10 continued on next page

Table 10 (*continued*)

#	Unit	Label	Description
34	mas	eyX	Uncertainty of the X-band position along the declination axis
35	—	CorrX	Correlation between right ascension and declination of the X-band source position
36	—	NobsX	Number of observations used in the X-band solution
37	—	NscaX	Number of scans used in the X-band solution
38	—	NsesX	Number of observing sessions used in the X-band solution
39	mas	dxK	Offset of the K-band position along the right ascension axis without $\cos \delta$ factor applied with respect to the position from the fused solution
40	mas	dyK	Offset of the K-band position along the declination axis with respect to the position from the fused solution
41	mas	exK	Uncertainty of the K-band position along the right ascension axis without $\cos \delta$ factor applied
42	mas	eyK	Uncertainty of the K-band position along the declination axis
43	—	CorrK	Correlation between right ascension and declination of the K-band source position
44	—	NobsK	Number of observations used in the K-band solution
45	—	NscaK	Number of scans used in the K-band solution
46	—	NsesK	Number of observing sessions used in the K-band solution

(a) Table 10 is too wide to be shown here. It is published in the machine-readable format only as file multi_band.txt

(b) -9.99 indicates a null value: no estimate is available.

Table 11. Column description of the table with Cross-matching RFC with 14 surveys^a.

#	Unit	Label	Description
1	—	Name	RFC object designator
2	—	NVSS_name	Name of the association in the NVSS catalogue
3	arcsec	NVSS_dist	Angular distance to the association in the NVSS catalogue
4	—	NVSS_pfa	The probability of falls association with a counterpart from the NVSS catalogue
5	—	VLASS_name	Name of the association in the VLASS catalogue
6	arcsec	VLASS_dist	Angular distance to the association in the VLASS catalogue
7	—	VLASS_pfa	The probability of false association with a counterpart from the VLASS catalogue
8	—	SUMSS_name	Name of the association in the SUMSS catalogue
9	arcsec	SUMSS_dist	Angular distance to the association in the SUMSS catalogue
10	—	SUMSS_pfa	The probability of false association with a counterpart from the SUMSS catalogue
11	—	TGSS_name	Name of the association in the TGSS catalogue
12	arcsec	TGSS_dist	Angular distance to the association in the TGSS catalogue
13	—	TGSS_pfa	The probability of false association with a counterpart from the TGSS catalogue
14	—	AT20G_name	Name of the association in the AT20G catalogue
15	arcsec	AT20G_dist	Angular distance to the association in the AT20G catalogue
16	—	AT20G_pfa	The probability of false association with a counterpart from the AT20G catalogue
17	—	Gaia_name	Name of the association in the Gaia catalogue
18	arcsec	GAIA_dist	Angular distance to the association in the Gaia catalogue
19	—	GAIA_pfa	The probability of false association with a counterpart from the Gaia catalogue

Table 11 *continued on next page*

Table 11 (*continued*)

#	Unit	Label	Description
20	—	PS1_name	Name of the association in the PS1 catalogue
21	arcsec	PS1_dist	Angular distance to the association in the PS1 catalogue
22	—	PS1_pfa	The probability of false association with a counterpart from the PS1 catalogue
23	—	WISE_name	Name of the association in the WISE catalogue
24	arcsec	WISE_dist	Angular distance to the association in the WISE catalogue
25	—	WISE_pfa	The probability of false association with a counterpart from the WISE catalogue
26	—	2MASS_name	Name of the association in the 2MASS catalogue
27	arcsec	2MASS_dist	Angular distance to the association in the 2MASS catalogue
28	—	2MASS_pfa	The probability of false association with a counterpart from the 2MASS catalogue
29	—	GALEX_name	Name of the association in the GALEX catalogue
30	arcsec	GALEX_dist	Angular distance to the association in the GALEX catalogue
31	—	GALEX_pfa	The probability of false association with a counterpart from the GALEX catalogue
32	—	2RXS_name	Name of the association in the 2RXS catalogue
33	arcsec	2RXS_dist	Angular distance to the association in the 2RXS catalogue
34	—	2RXS_pfa	The probability of false association with a counterpart from the VLASS catalogue
35	—	XMMLS_name	Name of the association in the XMMLS catalogue
36	arcsec	XMMLS_dist	Angular distance to the association in the XMMLS catalogue
37	—	XMMLS_pfa	The probability of false association with a counterpart from the XMMLS catalogue
38	—	1eRASS_name	Name of the association in the 1eRASS catalogue
39	arcsec	1eRASS_dist	Angular distance to the association in the 1eRASS catalogue
40	—	1eRASS_pfa	The probability of false association with a counterpart from the 1eRASS catalogue
41	—	FERMI_name	Name of the association in the FERMI catalogue
42	arcsec	FERMI_dist	Angular distance to the association in the FERMI catalogue
43	—	FERMI_pfa	The probability of false association with a counterpart from the FERMI catalogue
44	deg	PosAng	Jet position angle
45	—	z	Redshift
46	—	z_ref	Astrophysics Data System (ADS) reference to the redshift
47	—	type	Source type according to NED

^(a) Table 11 is too wide to be shown here. It is published in the machine-readable format only as file `cross_match.txt`

Table 12. Table of the sources that were observed at 4–8 GHz but have not been detected.

R.A.	decl	Flux density mJy
00 00 01.53	+68 10 02.4	12.0
00 00 02.87	+09 57 06.6	12.0
00 00 19.40	+55 39 03.0	12.0
00 00 23.80	+62 15 02.0	12.0
00 00 27.09	−33 19 36.7	12.0
...

NOTE—The third column shows the upper limit of the expected correlated flux density in units of mJy. Table 12 is published in its entirety in machine-readable format as file nondetections.txt. A portion is shown here for guidance regarding its form and content.

Table 13. The error floor as a function of declination for right ascension scaled by $\cos \delta$ and declination. Units are milliarcseconds. The first five lines of the table are shown below.

δ deg	R.A. mas	decl mas
−90.0	0.104	0.214
−89.0	0.104	0.214
−88.0	0.103	0.214
−87.0	0.103	0.214
−86.0	0.103	0.214
...

NOTE—Table 13 is published in its entirety in the machine-readable format as file error_floor_model.txt. A portion is shown here for guidance regarding its form and content.

Table 14. Table of non-canonical RFC designators.

(1)	(2)	(3)	(4)
RFC J0000+030B	J0000+0307	close	262.04
RFC J0008−233A	J0008−2339	close	481.40
RFC J0023+273A	J0023+2734	pair	0.16
RFC J0031+540A	J0031+5401	pair	0.14
RFC J0116+242A	J0116+2422	close	73.63
...

NOTE—Column descriptions: (1) the non-canonical RFC designator; (2) the RFC designator to the closest source with a canonical designator; (3) reason of assigning a non-canonical name; (4) the distance to the corresponding source with a canonical common name in arcseconds when applicable. Table 14 is published in its entirety in the machine-readable format as file noncanonical_jnames.txt. A portion is shown here for guidance regarding its form and content.

Table 15. Table of non-canonical common names.

(1)	(2)	(3)	(4)	(5)
RFC J0009+0625	0006+06A	0006+061	close	244.38
RFC J0010+1058	IIIZW2	0007+106	icrf1	...
RFC J0013-3227	0011-32B	0011-327	pair	53.65
RFC J0017+6750	0014+67A	0014+675	pair	51.98
RFC J0022+0014	4C+00.02	0019-000	vcs1	...
...

NOTE—Column descriptions: (1) the RFC designator of a source with non-canonical common name; (2) the non-canonical common name; (3) the common canonical name of the closest source; (4) reason of assigning a non-canonical name; (5) the distance to the corresponding source in arcseconds with a canonical common name when applicable. Table 15 is published in its entirety in the machine-readable format as file noncanonical_comnams.txt. A portion is shown here for guidance regarding its form and content.

Table 16. Table of pairs of sources within 1'.

(1)	(2)	(3)
RFC J0031+5401	RFC J0031+540A	0.1
RFC J0134-093C	RFC J0134-093A	0.1
RFC J0904+5938	RFC J0904+593A	0.1
RFC J2108-210A	RFC J2108-2101	0.1
RFC J0023+273A	RFC J0023+2734	0.2
...

NOTE—Columns descriptions: (1) the RFC designator of the first source in the pair; (2) the RFC designator of the second source in the pair; (3) the angular distance between sources in the pair in arcseconds. Table 16 is published in its entirety in the machine-readable format as file pairs.txt. A portion is shown here for guidance regarding its form and content.

Table 17. Table of the session names, experiment codes, and data archive names of astrometric experiments.

Session name	Exp name	Archive
19950412_p	br025	NRAO
19950419_p	bb023b	NRAO
19950531_p	rdwps1	NRAO
19950607_p	rdgeo1	NRAO
19950625_p	bb041b	NRAO
...

NOTE—Table 17 is published in its entirety in the machine-readable format as file astro_exp_names.txt. A portion is shown here for guidance regarding its form and content.

Table 18. Table of the session names, experiment codes, and data archive names of 24 hr geodetic experiments.

Session name	Exp name	Archive
19800411.a	xus801	CDDIS
19800413.a	hdsrvy	CDDIS
19800726.a	mert01	CDDIS
19800727.a	mert02	CDDIS
19800728.a	mert03	CDDIS
...

NOTE—Table 18 is published in its entirety in the machine-readable format as file geod24hr_exp_names.txt. A portion is shown here for guidance regarding its form and content.

Table 19. Table of the session names, experiment codes, and data archive names of 1 hr geodetic experiments.

Session name	Exp name	Archive
19920103.i	i92003	CDDIS
19920104.i	i92004	CDDIS
19920105.i	i92005	CDDIS
19920111.i	i92011	CDDIS
19920112.i	i92012	CDDIS
...

NOTE—Table 19 is published in its entirety in the machine-readable format as file geod1hr_exp_names.txt. A portion is shown here for guidance regarding its form and content.

Table 20. The list of 72 VLBI absolute astronomy observing campaigns used for deriving the RFC.

Campaign	Network	Id	Reference	Frequency		Dur. Num	Dates		Number of sources			
				low GHz	high GHz		start	end	obs	det	unique	
Pathfinder surveys:												
VCS1	VLBA	bb023	Beasley et al. (2002)	2.3	8.4	264	11	1994.08.12	1997.08.27	1838	1823	1
VLBApls	VLBA	bh019	Fomalont et al. (2000)	2.3	22.2	16	1	1996.06.05	1996.06.05	228	214	0
	VLBA	bb041	PI: T. Beasley, 1995	2.3	8.4	40	2	1995.06.25	1996.02.16	57	56	0
	VLBA	bu007	Ulvestad et al. (1999)		4.9	12	1	1996.12.19	1996.12.19	163	162	67
	VLBA	bg069	Liuzzo et al. (2009)		5.0	60	4	1997.04.06	2005.06.17	67	61	3
	VLBA	bb119	Britzen et al. (2007)		5.0	72	3	1999.11.21	1999.11.26	88	87	0
	EVN	ec013	Charlot et al. (2004)	8.4	2.3	71	3	2000.05.31	2003.10.17	161	161	0
VCS2	VLBA	bf071	Fomalont et al. (2003)	2.3	8.7	48	2	2002.01.31	2002.05.14	371	367	2
	VLBA	bb177	Bolton et al. (2006a)		5.0	12	1	2004.02.06	2004.02.06	38	35	9
VCS3	VLBA	bp110	Petrov et al. (2005)	2.3	8.7	72	3	2004.04.30	2004.05.27	533	487	0
VCS4	VLBA	bp118	Petrov et al. (2006)	2.3	8.7	72	3	2005.05.12	2005.06.30	504	410	0
	VLBA	bc151	Bolton et al. (2006b)		5.0	30	4	2005.06.16	2005.08.04	85	82	23

Table 20 continued on next page

Table 20 (continued)

Campaign	Network	Id	Reference	Frequency		Dur. Num		Dates		Number of sources		
				low	high		ses	start	end	obs	det	unique
				GHz	GHz	hour						
VCS5	VLBA	bk124	Kovalev et al. (2007)	2.3	8.7	72	3	2005.07.08	2005.07.20	748	701	0
VIPS	VLBA	bt085	Helmboldt et al. (2007), Petrov & Taylor (2011)		4.9	174	16	2006.01.03	2006.08.12	858	857	262
NPCS	VLBA	bk130	Popkov et al. (2021)	2.3	8.7	72	3	2006.02.14	2006.02.23	526	194	5
VGaPS	VLBA	bp125	Petrov et al. (2011a)		24.5	72	3	2006.06.04	2006.10.20	543	388	24
	VLBA	bm252	Majid et al. (2009)		8.7	20	2	2006.11.06	2006.11.13	74	53	30
VCS6	VLBA	bp133	Petrov et al. (2008)	2.3	8.7	48	2	2006.12.18	2007.01.11	347	329	0
VEGaPS	VERA	r07030a	PI: L. Petrov, 2007		22.2	28	2	2007.01.30	2007.03.21	125	110	0
LCS-1	LBA	v230r	Petrov et al. (2011b)		8.4	108	5	2007.06.24	2009.07.04	597	574	158
OBRS-1	EVN	gc030	Petrov (2011), Bourda et al. (2011)	2.3	8.4	48	1	2008.03.07	2008.03.07	115	115	1
EGaPS	EVN	ep066	Petrov (2012)		22.2	48	1	2009.10.27	2009.10.27	437	183	52
BeSSel-Cal1	VLBA	br145	Immer et al. (2011)		8.4	153	34	2009.11.16	2010.08.29	1535	364	95
	VLBA	bt110	Linford et al. (2012)		4.9	76	7	2009.11.22	2010.07.30	308	308	1
LCS-2	LBA	v271dr	Petrov et al. (2019a)	2.3		368	16	2009.12.12	2016.06.28	1401	959	480
BeSSel-Cal2	VLBA	br149	PI: M. Reid, 2010		8.4	43	14	2010.02.06	2013.08.04	574	176	37
	EVN	gb073	Petrov (2013), Bourda et al. (2011)	2.3	8.4	216	7	2010.03.23	2012.05.27	378	377	67
V2M	VLBA	bc191	Condon et al. (2017)	4.4	7.2	637	96	2010.07.15	2013.12.06	2701	1868	458
1FGL-VLBI	VLBA	s3111	PI: Y. Kovalev, 2010		8.7	72	3	2010.12.05	2011.01.09	283	279	84
VCS7	VLBA	bp171	Petrov (2021)	4.2	7.6	73	17	2013.02.08	2013.08.01	1626	968	422
2FGL-VLBIa	VLBA	s4195	PI: Y. Kovalev, 2013		7.6	72	3	2013.05.07	2013.06.22	322	289	136
2FGL-VLBIc	VLBA	s5272	Schinzel et al. (2015)		7.6	47	4	2013.08.06	2013.12.05	211	153	47
	VLBA	bp175	Petrov (2021)	2.3	8.1	43	10	2013.10.26	2013.12.26	405	401	0
VCS8	VLBA	bp177	Petrov (2021)	4.4	7.6	48	10	2014.01.07	2014.02.23	1386	927	446
VEPS-1	CVN	veps	Shu et al. (2017)		8.6	425	18	2015.02.13	2017.12.14	4571	973	0
2FGL-VLBIb	VLBA	bs241	Schinzel et al. (2015)		7.6	54	7	2015.02.16	2015.07.01	451	308	77
VCS9	VLBA	bp192	Petrov (2021)	4.4	7.6	528	99	2015.08.07	2016.09.07	11016	5688	3945
3FGL-VLBI	VLBA	s7104	Schinzel et al. (2017)		7.6	63	9	2016.06.25	2016.07.26	607	416	104
SOFUS	LBA	sofus	PI: L. Petrov, 2017		8.5	85	4	2017.04.07	2021.05.08	324	207	126
VOFUS-1	VLBA	bs262	Bruzewski et al. (2021)	4.4	7.6	70	21	2018.04.08	2018.07.24	970	883	319
VOFUS-2	VLBA	sb072	Bruzewski et al. (2021)	4.4	7.6	110	31	2018.08.25	2019.02.17	1467	1322	551
AGaPS	EAVN	ap001a	PI: L. Petrov, 2018		22.2	24	4	2018.10.09	2019.01.28	193	121	0
VCS10-CX	VLBA	bp242	PI: A. Popkov, 2019	4.4	7.6	94	20	2019.07.24	2020.03.17	2779	1491	1125
VCS10-SX	VLBA	bp245u	PI: A. Popkov, 2020	2.3	8.7	23	6	2020.03.02	2020.03.23	638	210	27
GC-KVN	KVN	n20lp01	PI: L. Petrov, 2020	22.7	43.9	69	14	2020.03.05	2020.06.16	400	174	0
	VLBA	bb409	PI: A. Beasley, 2020	4.9	6.7	24	4	2020.05.10	2020.07.20	656	28	16
VCS11	VLBA	br235	PI: T. Readhead, 2020	4.4	7.6	108	18	2020.09.11	2021.02.16	3328	2623	2150
VCS12	VLBA	bp252	PI: L. Petrov, 2021	4.4	7.7	244	53	2021.09.21	2022.12.18	9564	3318	2284

Table 20 continued on next page

Table 20 (*continued*)

Campaign	Network	Id	Reference	Frequency		Dur. Num		Dates		Number of sources		
				low GHz	high GHz	ses	hour	start	end	obs	det	unique
Astrometric follow-ups surveys:												
RDV	VLBA	rv	Petrov et al. (2009)	2.3	8.4	5265	219	1994.07.08	2023.07.04	2281	2236	7
	VLBA	bf025	Fey & Charlot (1997)	2.3	8.4	48	2	1997.01.10	1997.01.11	226	225	0
VCS-II	VLBA	bg219	Gordon et al. (2016)	2.3	8.7	196	9	2014.01.04	2015.03.17	2597	2532	0
VEPS-V1	VLBA	bs250	Shu et al. (2017)	2.3	8.7	32	4	2016.03.22	2016.05.19	163	163	0
VCS-III	VLBA	uf001	de Witt et al. (2021)	2.3	8.7	478	20	2017.01.16	2017.10.21	3654	3647	0
GAIA-L2	LBA	v561	PI: L. Petrov, 2017	2.3	8.6	71	2	2017.06.16	2018.03.14	306	303	0
SOAP	LBA	aua025	PI: L. Petrov, 2017	2.3	8.6	568	24	2017.08.22	2019.12.04	444	422	6
VCS-IV	VLBA	ug002	de Witt et al. (2021)	2.3	8.7	573	24	2018.01.18	2019.01.21	4416	4238	10
VEPS-3	CVN	epa	PI: L. Petrov, 2018	2.3	8.6	44	2	2018.01.24	2018.02.10	182	181	0
VEPS-2	VLBA	bs264	PI: F. Shu, 2018	2.3	8.7	48	6	2018.03.21	2018.06.15	357	357	0
GAIA-V1	VLBA	bp222	PI: L. Petrov, 2018	2.3	8.7	304	38	2018.05.15	2020.04.19	1367	1367	0
VCS-V	VLBA	ug003	de Witt et al. (2021)	2.3	8.7	620	26	2019.01.27	2020.08.09	4167	4162	1
VCS-VI	VLBA	uh007	de Witt et al. (2021)	2.3	8.7	667	28	2020.09.18	2022.12.12	2545	2536	0
High frequency extensions:												
K/Q-Survey	VLBA	bl115	Lanyi et al. (2010), Charlot et al. (2010)	24.5	43.2	336	14	2002.05.15	2011.02.05	343	334	0
KVNCS	KVN	n13jl01	Lee et al. (2023);		23.0	196	7	2013.09.04	2014.12.24	790	752	0
	VLBA	bj083	de Witt et al. (2023)		24.6	105	5	2015.07.21	2016.06.20	286	286	0
	EVN	ec076	Gomez et al. (2021)		22.3	48	2	2016.06.15	2020.10.23	172	169	0
	VLBA	ud001	de Witt et al. (2023)		23.6	564	24	2017.01.08	2018.07.22	738	734	0
	VLBA	ud009	de Witt et al. (2023)		23.6	823	35	2018.09.09	2021.06.12	821	818	0
GAJI	KVN	gaji	PI: L. Petrov, 2018	21.7	43.8	22	4	2018.09.25	2018.12.29	151	90	0
	EAVN	a20	PI: S. Xu, 2020		21.3	240	10	2020.05.07	2023.06.08	328	318	0
GC-VLBA	VLBA	bp251	PI: Y. Pihlstrom, 2021	24.0	43.2	34	8	2021.03.19	2022.05.25	138	138	1
	VLBA	ud015	PI: A. de Witt, 2021		23.6	426	18	2021.07.26	2023.01.06	919	914	0
	VLBA	ud018	PI: A. de Witt, 2023		23.6	16	4	2023.07.03	2023.07.24	68	68	0
Total						16944	1140			42469	21940	13659

NOTE—Principal Investigator name is given for the observing campaigns that do not have publications.

NOTE—Two sources, 0528–654 and 1144+404 were observed only in geodetic experiments and are not counted here.

NOTE—The last columns shows the number of detected sources that are unique for that campaign and were not detected in any other campaign.

Facilities: VLBA,LBA, CVN, EVN, EAVN, IVS, KaVa, VERA, KVN

Software: SGDASS (L. Petrov, under review, 2025), AIPS (Greisen 2003), Difmap (Shepherd 1997)

REFERENCES

- Abbasi, R., Ackermann, M., Adams, J., et al. 2023, *ApJ*, 954, 75, doi: [10.3847/1538-4357/acdfcb](https://doi.org/10.3847/1538-4357/acdfcb)
- Abdo, A. A., Ackermann, M., Ajello, M., et al. 2010, *The Astrophysical Journal Supplement Series*, 188, 405–436, doi: [10.1088/0067-0049/188/2/405](https://doi.org/10.1088/0067-0049/188/2/405)
- Abdollahi, S., Acero, F., Baldini, L., et al. 2022, *ApJS*, 260, 53, doi: [10.3847/1538-4365/ac6751](https://doi.org/10.3847/1538-4365/ac6751)
- Abellán, F. J., Martí-Vidal, I., Marcaide, J. M., & Guirado, J. C. 2018, *A&A*, 614, A74, doi: [10.1051/0004-6361/201731869](https://doi.org/10.1051/0004-6361/201731869)
- Acero, F., Ackermann, M., Ajello, M., et al. 2015, *ApJS*, 218, 23, doi: [10.1088/0067-0049/218/2/23](https://doi.org/10.1088/0067-0049/218/2/23)
- Ajello, M., Angioni, R., Axelsson, M., et al. 2020, *The Astrophysical Journal*, 892, 105, doi: [10.3847/1538-4357/ab791e](https://doi.org/10.3847/1538-4357/ab791e)
- Altamimi, Z., Sillard, P., & Boucher, C. 2002, *Journal of Geophysical Research: Solid Earth*, 107, doi: [10.1029/2001jb000561](https://doi.org/10.1029/2001jb000561)
- Arias, E. F., Charlot, P., Feissel, M., & Lestrade, J. F. 1995, *A&A*, 303, 604
- Auwers, A., 1879, *Publication der Astronomischen Gesellschaft*, XIV, doi: [10.1051/0004-6361/202347165](https://doi.org/10.1051/0004-6361/202347165)
- Beasley, A. J., Gordon, D., Peck, A. B., et al. 2002, *ApJS*, 141, 13, doi: [10.1086/339806](https://doi.org/10.1086/339806)
- Bellenghi, C., Padovani, P., Resconi, E., & Giommi, P. 2023, *ApJL*, 955, L32, doi: [10.3847/2041-8213/acf711](https://doi.org/10.3847/2041-8213/acf711)
- Bianchi, L., Shiao, B., & Thilker, D. 2017, *The Astrophysical Journal Supplement Series*, 230, 24, doi: [10.3847/1538-4365/aa7053](https://doi.org/10.3847/1538-4365/aa7053)
- Blandford, R., Meier, D., & Readhead, A. 2019, *ARA&A*, 57, 467, doi: [10.1146/annurev-astro-081817-051948](https://doi.org/10.1146/annurev-astro-081817-051948)
- Blandford, R. D., & Königl, A. 1979, *ApJ*, 232, 34, doi: [10.1086/157262](https://doi.org/10.1086/157262)
- Bock, D. C.-J., Large, M. I., & Sadler, E. M. 1999, *AJ*, 117, 1578, doi: [10.1086/300786](https://doi.org/10.1086/300786)
- Boller, T., Freyberg, M. J., Trümper, J., et al. 2016, *A&A*, 588, A103, doi: [10.1051/0004-6361/201525648](https://doi.org/10.1051/0004-6361/201525648)
- Bolton, R. C., Chandler, C. J., Cotter, G., et al. 2006a, *MNRAS*, 370, 1556, doi: [10.1111/j.1365-2966.2006.10578.x](https://doi.org/10.1111/j.1365-2966.2006.10578.x)
- . 2006b, *MNRAS*, 367, 323, doi: [10.1111/j.1365-2966.2005.09952.x](https://doi.org/10.1111/j.1365-2966.2005.09952.x)
- Bourda, G., Collioud, A., Charlot, P., Porcas, R., & Garrington, S. 2011, *A&A*, 526, A102, doi: [10.1051/0004-6361/201014249](https://doi.org/10.1051/0004-6361/201014249)
- Britzen, S., Vermeulen, R. C., Taylor, G. B., et al. 2007, *A&A*, 472, 763, doi: [10.1051/0004-6361:20052677](https://doi.org/10.1051/0004-6361:20052677)
- Browne, I. W. A., Wilkinson, P. N., Patnaik, A. R., & Wrobel, J. M. 1998, *MNRAS*, 293, 257, doi: [10.1046/j.1365-8711.1998.01072.x](https://doi.org/10.1046/j.1365-8711.1998.01072.x)
- Bruzewski, S., Schinzel, F. K., Taylor, G. B., & Petrov, L. 2021, *ApJ*, 914, 42, doi: [10.3847/1538-4357/abf73b](https://doi.org/10.3847/1538-4357/abf73b)
- Campbell, J., Schuh, H., & Zeppenfeld, G. 1988, in *The Impact of VLBI on Astrophysics and Geophysics*, ed. M. J. Reid & J. M. Moran, Vol. 129, 427
- Chamani, W., Savolainen, T., Ros, E., et al. 2023, *A&A*, 672, A130, doi: [10.1051/0004-6361/202243435](https://doi.org/10.1051/0004-6361/202243435)
- Chambers, K. C., Magnier, E. A., Metcalfe, N., et al. 2016, *arXiv e-prints*. <https://arxiv.org/abs/1612.05560>
- Charlot, P. 1990, *AJ*, 99, 1309, doi: [10.1086/115419](https://doi.org/10.1086/115419)
- Charlot, P., Fey, A. L., Jacobs, C. S., et al. 2004, in *European VLBI Network on New Developments in VLBI Science and Technology*, 313–316. <https://arxiv.org/abs/astro-ph/0412458>
- Charlot, P., Boboltz, D. A., Fey, A. L., et al. 2010, *AJ*, 139, 1713, doi: [10.1088/0004-6256/139/5/1713](https://doi.org/10.1088/0004-6256/139/5/1713)
- Charlot, P., Jacobs, C. S., Gordon, D., et al. 2020, *A&A*, 644, A159, doi: [10.1051/0004-6361/202038368](https://doi.org/10.1051/0004-6361/202038368)
- Cigan, P., Makarov, V. V., Secrest, N. J., et al. 2024, *The Astrophysical Journal Supplement Series*, 274, 28, doi: [10.3847/1538-4365/ad6772](https://doi.org/10.3847/1538-4365/ad6772)
- Claeskens, J.-F., & Surdej, J. 2002, *A&A Rv*, 10, 263, doi: [10.1007/s001590000010](https://doi.org/10.1007/s001590000010)
- Clark, T. A., Corey, B. E., Davis, J. L., Herring, T. A., & Elgered, G. 1985, *IEEE Transactions on Geoscience and Remote Sensing*, 23, 438, doi: [10.1109/TGRS.1985.289433](https://doi.org/10.1109/TGRS.1985.289433)
- Cohen, M. H., & Shaffer, D. B. 1971, *AJ*, 76, 91, doi: [10.1086/111090](https://doi.org/10.1086/111090)
- Condon, J. J., Cotton, W. D., Greisen, E. W., et al. 1998, *AJ*, 115, 1693, doi: [10.1086/300337](https://doi.org/10.1086/300337)
- Condon, J. J., Darling, J., Kovalev, Y. Y., & Petrov, L. 2017, *ApJ*, 834, 184, doi: [10.3847/1538-4357/834/2/184](https://doi.org/10.3847/1538-4357/834/2/184)
- Condon, J. J., Griffith, M. R., & Wright, A. E. 1993, *AJ*, 106, 1095, doi: [10.1086/116707](https://doi.org/10.1086/116707)
- Cotton, W. D. 1979, *AJ*, 84, 1122, doi: [10.1086/112519](https://doi.org/10.1086/112519)
- de Witt, A., Jacobs, C. S., Gordon, D., et al. 2023, *AJ*, 165, 139, doi: [10.3847/1538-3881/aca012](https://doi.org/10.3847/1538-3881/aca012)
- de Witt, A., Basu, S., Charlot, P., et al. 2021, in *25th European VLBI Group for Geodesy and Astrometry Working Meeting*, ed. R. Haas, Vol. 25, 1
- Deller, A. T., & Middelberg, E. 2014, *AJ*, 147, 14, doi: [10.1088/0004-6256/147/1/14](https://doi.org/10.1088/0004-6256/147/1/14)
- Deller, A. T., Tingay, S. J., Bailes, M., & West, C. 2007, *PASP*, 119, 318, doi: [10.1086/513572](https://doi.org/10.1086/513572)
- Deller, A. T., Brisken, W. F., Phillips, C. J., et al. 2011, *PASP*, 123, 275, doi: [10.1086/658907](https://doi.org/10.1086/658907)

- Diamantidis, P.-K., & Haas, R. 2023, *Earth, Planets and Space*, 75, 114, doi: [10.1186/s40623-023-01872-x](https://doi.org/10.1186/s40623-023-01872-x)
- Ding, H., Deller, A. T., Freire, P. C. C., & Petrov, L. 2024, arXiv e-prints, arXiv:2407.13324, doi: [10.48550/arXiv.2407.13324](https://doi.org/10.48550/arXiv.2407.13324)
- Fanti, C., Fanti, R., Ficarra, A., & Padrielli, L. 1974, *A&AS*, 18, 147
- Fey, A. L., & Charlot, P. 1997, *ApJS*, 111, 95, doi: [10.1086/313017](https://doi.org/10.1086/313017)
- Fey, A. L., Gordon, D., Jacobs, C. S., et al. 2015, *AJ*, 150, 58, doi: [10.1088/0004-6256/150/2/58](https://doi.org/10.1088/0004-6256/150/2/58)
- Flewelling, H. A., Magnier, E. A., Chambers, K. C., et al. 2020, *The Astrophysical Journal Supplement Series*, 251, 7, doi: [10.3847/1538-4365/abb82d](https://doi.org/10.3847/1538-4365/abb82d)
- Fomalont, E. B., Frey, S., Paragi, Z., et al. 2000, *ApJS*, 131, 95, doi: [10.1086/317368](https://doi.org/10.1086/317368)
- Fomalont, E. B., Petrov, L., MacMillan, D. S., Gordon, D., & Ma, C. 2003, *AJ*, 126, 2562, doi: [10.1086/378712](https://doi.org/10.1086/378712)
- Fricke, W. 1985, *Celestial Mechanics*, 36, 207, doi: [10.1007/BF01230737](https://doi.org/10.1007/BF01230737)
- Gomez, M. E., Charlot, P., Campbell, R. M., Kettanis, M., & Keimpema, A. 2021, in 25th European VLBI Group for Geodesy and Astrometry Working Meeting, ed. R. Haas, Vol. 25, 39–42
- Gordon, D., Cappallo, R., & Titus, M. 2012, in Seventh General Meeting (GM2012) of the international VLBI Service for Geodesy and Astrometry (IVS), 256–260
- Gordon, D., Jacobs, C., Beasley, A., et al. 2016, *AJ*, 151, 154, doi: [10.3847/0004-6256/151/6/154](https://doi.org/10.3847/0004-6256/151/6/154)
- Gordon, Y. A., Boyce, M. M., O’Dea, C. P., et al. 2021, *The Astrophysical Journal Supplement Series*, 255, 30, doi: [10.3847/1538-4365/ac05c0](https://doi.org/10.3847/1538-4365/ac05c0)
- Gregory, P. C., Scott, W. K., Douglas, K., & Condon, J. J. 1996, *ApJS*, 103, 427, doi: [10.1086/192282](https://doi.org/10.1086/192282)
- Greisen, E. W. 2003, in *Astrophysics and Space Science Library*, Vol. 285, Information Handling in Astronomy - Historical Vistas, ed. A. Heck, 109, doi: [10.1007/0-306-48080-8_7](https://doi.org/10.1007/0-306-48080-8_7)
- Griffith, M. R., & Wright, A. E. 1993, *AJ*, 105, 1666, doi: [10.1086/116545](https://doi.org/10.1086/116545)
- Griffith, M. R., Wright, A. E., Burke, B. F., & Ekers, R. D. 1994, *ApJS*, 90, 179, doi: [10.1086/191863](https://doi.org/10.1086/191863)
- . 1995, *ApJS*, 97, 347, doi: [10.1086/192146](https://doi.org/10.1086/192146)
- Gwinn, C. R., Kovalev, Y. Y., Johnson, M. D., & Soglasnov, V. A. 2014, *ApJL*, 794, L14, doi: [10.1088/2041-8205/794/1/L14](https://doi.org/10.1088/2041-8205/794/1/L14)
- Halsig, S., Bertarini, A., Haas, R., et al. 2019, *Journal of Geodesy*, 93, 593, doi: [10.1007/s00190-018-1184-5](https://doi.org/10.1007/s00190-018-1184-5)
- Hartmann, T., & Wenzel, H.-G. 1995, *Geophys. Res. Lett.*, 22, 3553, doi: [10.1029/95GL03324](https://doi.org/10.1029/95GL03324)
- Hawarey, M., Hobiger, T., & Schuh, H. 2005, *Geophys. Res. Lett.*, 32, L11304, doi: [10.1029/2005GL022729](https://doi.org/10.1029/2005GL022729)
- Healey, S. E., Romani, R. W., Taylor, G. B., et al. 2007, *ApJS*, 171, 61, doi: [10.1086/513742](https://doi.org/10.1086/513742)
- Helmboldt, J. F., Taylor, G. B., Tremblay, S., et al. 2007, *ApJ*, 658, 203, doi: [10.1086/511005](https://doi.org/10.1086/511005)
- Helou, G., Madore, B. F., Schmitz, M., et al. 1991, in *Astrophysics and Space Science Library*, Vol. 171, Databases and On-line Data in Astronomy, ed. M. A. Albrecht & D. Egret, 89–106, doi: [10.1007/978-94-011-3250-3_10](https://doi.org/10.1007/978-94-011-3250-3_10)
- Herring, T. A., Gwinn, C. R., & Shapiro, I. I. 1986, *J. Geophys. Res.*, 91, 4745, doi: [10.1029/JB091iB05p04745](https://doi.org/10.1029/JB091iB05p04745)
- Hovatta, T., Aller, M. F., Aller, H. D., et al. 2014, *AJ*, 147, 143, doi: [10.1088/0004-6256/147/6/143](https://doi.org/10.1088/0004-6256/147/6/143)
- Immer, K., Brunthaler, A., Reid, M. J., et al. 2011, *ApJS*, 194, 25, doi: [10.1088/0067-0049/194/2/25](https://doi.org/10.1088/0067-0049/194/2/25)
- Intema, H. T., Jagannathan, P., Mooley, K. P., & Frail, D. A. 2017, *A&A*, 598, A78, doi: [10.1051/0004-6361/201628536](https://doi.org/10.1051/0004-6361/201628536)
- Jackson, C. A., Wall, J. V., Shaver, P. A., et al. 2002, *A&A*, 386, 97, doi: [10.1051/0004-6361:20020119](https://doi.org/10.1051/0004-6361:20020119)
- Johnson, M. D., Kovalev, Y. Y., Gwinn, C. R., et al. 2016, *ApJL*, 820, L10, doi: [10.3847/2041-8205/820/1/L10](https://doi.org/10.3847/2041-8205/820/1/L10)
- Jones, D. L., Folkner, W. M., Jacobson, R. A., et al. 2020, *AJ*, 159, 72, doi: [10.3847/1538-3881/ab5f5d](https://doi.org/10.3847/1538-3881/ab5f5d)
- Kardashev, N. S., Khartov, V. V., Abramov, V. V., et al. 2013, *Astronomy Reports*, 57, 153, doi: [10.1134/S1063772913030025](https://doi.org/10.1134/S1063772913030025)
- Kellermann, K. I., Vermeulen, R. C., Zensus, J. A., & Cohen, M. H. 1998, *AJ*, 115, 1295, doi: [10.1086/300308](https://doi.org/10.1086/300308)
- Königl, A. 1981, *ApJ*, 243, 700, doi: [10.1086/158638](https://doi.org/10.1086/158638)
- Koryukova, T. A., Pushkarev, A. B., Kiehlmann, S., & Readhead, A. C. S. 2023, *MNRAS*, 526, 5932, doi: [10.1093/mnras/stad3052](https://doi.org/10.1093/mnras/stad3052)
- Koryukova, T. A., Pushkarev, A. B., Plavin, A. V., & Kovalev, Y. Y. 2022, *MNRAS*, 515, 1736, doi: [10.1093/mnras/stac1898](https://doi.org/10.1093/mnras/stac1898)
- Kovalev, Y. Y. 2009, *ApJL*, 707, L56, doi: [10.1088/0004-637X/707/1/L56](https://doi.org/10.1088/0004-637X/707/1/L56)
- Kovalev, Y. Y., Lobanov, A. P., Pushkarev, A. B., & Zensus, J. A. 2008, *A&A*, 483, 759, doi: [10.1051/0004-6361:20078679](https://doi.org/10.1051/0004-6361:20078679)
- Kovalev, Y. Y., Petrov, L., Fomalont, E. B., & Gordon, D. 2007, *AJ*, 133, 1236, doi: [10.1086/511157](https://doi.org/10.1086/511157)
- Kovalev, Y. Y., Petrov, L., & Plavin, A. V. 2017, *A&A*, 598, L1, doi: [10.1051/0004-6361/201630031](https://doi.org/10.1051/0004-6361/201630031)

- Krásná, H., & Petrov, L. 2021, *Journal of Geodesy*, 95, 101, doi: [10.1007/s00190-021-01551-3](https://doi.org/10.1007/s00190-021-01551-3)
- Kutkin, A. M., Sokolovsky, K. V., Lisakov, M. M., et al. 2014, *MNRAS*, 437, 3396, doi: [10.1093/mnras/stt2133](https://doi.org/10.1093/mnras/stt2133)
- Lambert, S., Sol, H., & Pierron, A. 2024, *A&A*, 684, A202, doi: [10.1051/0004-6361/202347210](https://doi.org/10.1051/0004-6361/202347210)
- Lanyi, G. E., Boboltz, D. A., Charlot, P., et al. 2010, *AJ*, 139, 1695, doi: [10.1088/0004-6256/139/5/1695](https://doi.org/10.1088/0004-6256/139/5/1695)
- Le Bail, K., Gipson, J. M., Gordon, D., et al. 2016, *AJ*, 151, 79, doi: [10.3847/0004-6256/151/3/79](https://doi.org/10.3847/0004-6256/151/3/79)
- Lee, J. A., Jung, T., Sohn, B. W., & Byun, D.-Y. 2023, *Journal of Korean Astronomical Society*, 56, 159, doi: [10.5303/JKAS.2023.56.2.159](https://doi.org/10.5303/JKAS.2023.56.2.159)
- Lee, J. A., Sohn, B. W., Jung, T., Byun, D.-Y., & Lee, J. W. 2017, *The Astrophysical Journal Supplement Series*, 228, 22, doi: [10.3847/1538-4365/228/2/22](https://doi.org/10.3847/1538-4365/228/2/22)
- Lindgren, L., Klioner, S. A., Hernández, J., et al. 2021, *A&A*, 649, A2, doi: [10.1051/0004-6361/202039709](https://doi.org/10.1051/0004-6361/202039709)
- Linford, J. D., Taylor, G. B., Romani, R. W., et al. 2012, *ApJ*, 744, 177, doi: [10.1088/0004-637X/744/2/177](https://doi.org/10.1088/0004-637X/744/2/177)
- Lister, M. L., Aller, M. F., Aller, H. D., et al. 2018, *ApJS*, 234, 12, doi: [10.3847/1538-4365/aa9c44](https://doi.org/10.3847/1538-4365/aa9c44)
- Liuzzo, E., Giovannini, G., Giroletti, M., & Taylor, G. B. 2009, *A&A*, 505, 509, doi: [10.1051/0004-6361/200912586](https://doi.org/10.1051/0004-6361/200912586)
- Lobanov, A. P. 1998, *A&A*, 330, 79, doi: [10.48550/arXiv.astro-ph/9712132](https://doi.org/10.48550/arXiv.astro-ph/9712132)
- Lovell, J. E. J., Jauncey, D. L., Bignall, H. E., et al. 2003, *AJ*, 126, 1699, doi: [10.1086/378053](https://doi.org/10.1086/378053)
- Ma, C., & Shaffer, D. B. 1991, in *IAU Colloq. 127: Reference Systems*, ed. J. A. Hughes, C. A. Smith, & G. H. Kaplan, 135
- Ma, C., Clark, T. A., Ryan, J. W., et al. 1986, *AJ*, 92, 1020, doi: [10.1086/114232](https://doi.org/10.1086/114232)
- Ma, C., Arias, E. F., Eubanks, T. M., et al. 1998, *AJ*, 116, 516, doi: [10.1086/300408](https://doi.org/10.1086/300408)
- Majid, W. A., Fomalont, E. B., & Bagri, D. S. 2009, in *Astronomical Society of the Pacific Conference Series*, Vol. 402, *Approaching Micro-Arcsecond Resolution with VSOP-2: Astrophysics and Technologies*, ed. Y. Hagiwara, E. Fomalont, M. Tsuboi, & M. Yasuhiro, 448. <https://arxiv.org/abs/0806.3061>
- Martí-Vidal, I., Ros, E., Pérez-Torres, M. A., et al. 2010, *A&A*, 515, A53, doi: [10.1051/0004-6361/201014203](https://doi.org/10.1051/0004-6361/201014203)
- Matveenko, L. I., Kardashev, N.-S., & Sholomitskii, G.-B. 1965, *Soviet Radiophys.*, 461, 461
- Mauch, T., Murphy, T., Buttery, H. J., et al. 2003, *MNRAS*, 342, 1117, doi: [10.1046/j.1365-8711.2003.06605.x](https://doi.org/10.1046/j.1365-8711.2003.06605.x)
- McConnell, D., Sadler, E. M., Murphy, T., & Ekers, R. D. 2012, *MNRAS*, 422, 1527, doi: [10.1111/j.1365-2966.2012.20726.x](https://doi.org/10.1111/j.1365-2966.2012.20726.x)
- Merloni, A., Lamer, G., Liu, T., et al. 2024, *A&A*, 682, A34, doi: [10.1051/0004-6361/202347165](https://doi.org/10.1051/0004-6361/202347165)
- Morabito, D. D., Niell, A. E., Preston, R. A., et al. 1986, *AJ*, 91, 1038, doi: [10.1086/114080](https://doi.org/10.1086/114080)
- Morabito, D. D., Preston, R. A., Slade, M. A., & Jauncey, D. L. 1982, *AJ*, 87, 517, doi: [10.1086/113124](https://doi.org/10.1086/113124)
- Morabito, D. D., Preston, R. A., Slade, M. A., Jauncey, D. L., & Nicolson, G. D. 1983, *AJ*, 88, 1138, doi: [10.1086/113403](https://doi.org/10.1086/113403)
- Morabito, D. D., Wehrle, A. E., Preston, R. A., et al. 1985, *AJ*, 90, 590, doi: [10.1086/113764](https://doi.org/10.1086/113764)
- Murphy, T., Sadler, E. M., Ekers, R. D., et al. 2010, *MNRAS*, 402, 2403, doi: [10.1111/j.1365-2966.2009.15961.x](https://doi.org/10.1111/j.1365-2966.2009.15961.x)
- Myers, S. T., Jackson, N. J., Browne, I. W. A., et al. 2003, *MNRAS*, 341, 1, doi: [10.1046/j.1365-8711.2003.06256.x](https://doi.org/10.1046/j.1365-8711.2003.06256.x)
- Nolan, P. L., Abdo, A. A., Ackermann, M., et al. 2012, *The Astrophysical Journal Supplement Series*, 199, 31, doi: [10.1088/0067-0049/199/2/31](https://doi.org/10.1088/0067-0049/199/2/31)
- Nothnagel, A., Zhihan, Q., Nicolson, G. D., & Tomasi, P. 1994, *Bulletin Geodesique*, 68, 1, doi: [10.1007/BF00806747](https://doi.org/10.1007/BF00806747)
- Oyama, T., Nagayama, T., Yamauchi, A., et al. 2024, *Publications of the Astronomical Society of Japan*, 76, 163, doi: [10.1093/pasj/psad088](https://doi.org/10.1093/pasj/psad088)
- Patnaik, A. R., Browne, I. W. A., Wilkinson, P. N., & Wrobel, J. M. 1992, *MNRAS*, 254, 655, doi: [10.1093/mnras/254.4.655](https://doi.org/10.1093/mnras/254.4.655)
- Pearson, T. J., & Readhead, A. C. S. 1988, *ApJ*, 328, 114, doi: [10.1086/166274](https://doi.org/10.1086/166274)
- Pearson, T. J., Shepherd, M. C., Taylor, G. B., & Myers, S. T. 1994, in *American Astronomical Society Meeting Abstracts*, Vol. 185, *American Astronomical Society Meeting Abstracts*, 08.08
- Petit, G., & Luzum, B. 2010, *IERS Technical Note*, 36, 1
- Petrov, L. 2007, *A&A*, 467, 359, doi: [10.1051/0004-6361:20065091](https://doi.org/10.1051/0004-6361:20065091)
- . 2011, *AJ*, 142, 105, doi: [10.1088/0004-6256/142/4/105](https://doi.org/10.1088/0004-6256/142/4/105)
- . 2012, *MNRAS*, 419, 1097, doi: [10.1111/j.1365-2966.2011.19765.x](https://doi.org/10.1111/j.1365-2966.2011.19765.x)
- . 2013, *AJ*, 146, 5, doi: [10.1088/0004-6256/146/1/5](https://doi.org/10.1088/0004-6256/146/1/5)
- . 2015a, *arXiv e-prints*, arXiv:1503.00191, doi: [10.48550/arXiv.1503.00191](https://doi.org/10.48550/arXiv.1503.00191)
- . 2015b, *ArXiv e-prints*, 1502.06678. <https://arxiv.org/pdf/1502.06678>
- . 2021, *AJ*, 161, 14, doi: [10.3847/1538-3881/abc4e1](https://doi.org/10.3847/1538-3881/abc4e1)
- . 2023, *AJ*, 165, 183, doi: [10.3847/1538-3881/acc174](https://doi.org/10.3847/1538-3881/acc174)

- . 2024, arXiv e-prints, arXiv:2404.08800, doi: [10.48550/arXiv.2404.08800](https://doi.org/10.48550/arXiv.2404.08800)
- Petrov, L., de Witt, A., Sadler, E. M., Phillips, C., & Horiuchi, S. 2019a, MNRAS, 485, 88, doi: [10.1093/mnras/stz242](https://doi.org/10.1093/mnras/stz242)
- Petrov, L., Gordon, D., Gipson, J., et al. 2009, Journal of Geodesy, 83, 859, doi: [10.1007/s00190-009-0304-7](https://doi.org/10.1007/s00190-009-0304-7)
- Petrov, L., Hirota, T., Honma, M., et al. 2007, AJ, 133, 2487, doi: [10.1086/513146](https://doi.org/10.1086/513146)
- Petrov, L., & Kovalev, Y. Y. 2017a, MNRAS, 467, L71, doi: [10.1093/mnras/lsx001](https://doi.org/10.1093/mnras/lsx001)
- . 2017b, MNRAS, 471, 3775, doi: [10.1093/mnras/stx1747](https://doi.org/10.1093/mnras/stx1747)
- Petrov, L., Kovalev, Y. Y., Fomalont, E. B., & Gordon, D. 2005, AJ, 129, 1163, doi: [10.1086/426920](https://doi.org/10.1086/426920)
- . 2006, AJ, 131, 1872, doi: [10.1086/499947](https://doi.org/10.1086/499947)
- . 2008, AJ, 136, 580, doi: [10.1088/0004-6256/136/2/580](https://doi.org/10.1088/0004-6256/136/2/580)
- . 2011a, AJ, 142, 35, doi: [10.1088/0004-6256/142/2/35](https://doi.org/10.1088/0004-6256/142/2/35)
- Petrov, L., Kovalev, Y. Y., & Plavin, A. V. 2019b, MNRAS, 482, 3023, doi: [10.1093/mnras/sty2807](https://doi.org/10.1093/mnras/sty2807)
- Petrov, L., & Ma, C. 2003, Journal of Geophysical Research (Solid Earth), 108, 2190, doi: [10.1029/2002JB001801](https://doi.org/10.1029/2002JB001801)
- Petrov, L., Mahony, E. K., Edwards, P. G., et al. 2013, MNRAS, 432, 1294, doi: [10.1093/mnras/stt550](https://doi.org/10.1093/mnras/stt550)
- Petrov, L., Phillips, C., Bertarini, A., Murphy, T., & Sadler, E. M. 2011b, MNRAS, 414, 2528, doi: [10.1111/j.1365-2966.2011.18570.x](https://doi.org/10.1111/j.1365-2966.2011.18570.x)
- Petrov, L., & Taylor, G. B. 2011, AJ, 142, 89, doi: [10.1088/0004-6256/142/3/89](https://doi.org/10.1088/0004-6256/142/3/89)
- Piner, B. G., Pushkarev, A. B., Kovalev, Y. Y., et al. 2012, ApJ, 758, 84, doi: [10.1088/0004-637X/758/2/84](https://doi.org/10.1088/0004-637X/758/2/84)
- Plank, L., Shabala, S. S., McCallum, J. N., et al. 2016, MNRAS, 455, 343, doi: [10.1093/mnras/stv2080](https://doi.org/10.1093/mnras/stv2080)
- Plavin, A., Kovalev, Y. Y., Kovalev, Y. A., & Troitsky, S. 2020, ApJ, 894, 101, doi: [10.3847/1538-4357/ab86bd](https://doi.org/10.3847/1538-4357/ab86bd)
- Plavin, A. V., Kovalev, Y. Y., Kovalev, Y. A., & Troitsky, S. V. 2021, ApJ, 908, 157, doi: [10.3847/1538-4357/abceb8](https://doi.org/10.3847/1538-4357/abceb8)
- . 2023, MNRAS, 523, 1799, doi: [10.1093/mnras/stad1467](https://doi.org/10.1093/mnras/stad1467)
- Plavin, A. V., Kovalev, Y. Y., & Petrov, L. Y. 2019a, ApJ, 871, 143, doi: [10.3847/1538-4357/aaf650](https://doi.org/10.3847/1538-4357/aaf650)
- Plavin, A. V., Kovalev, Y. Y., & Pushkarev, A. B. 2022, ApJS, 260, 4, doi: [10.3847/1538-4365/ac6352](https://doi.org/10.3847/1538-4365/ac6352)
- Plavin, A. V., Kovalev, Y. Y., Pushkarev, A. B., & Lobanov, A. P. 2019b, MNRAS, 485, 1822, doi: [10.1093/mnras/stz504](https://doi.org/10.1093/mnras/stz504)
- Popkov, A. V., Kovalev, Y. Y., Petrov, L. Y., & Kovalev, Y. A. 2021, AJ, 161, 88, doi: [10.3847/1538-3881/abd18c](https://doi.org/10.3847/1538-3881/abd18c)
- Porcas, R. W. 2004, VLBI Observations of Gravitational Lenses (Springer Netherlands), 219–231, doi: [10.1007/1-4020-2406-1_13](https://doi.org/10.1007/1-4020-2406-1_13)
- Porcas, R. W. 2009, A&A, 505, L1, doi: [10.1051/0004-6361/200912846](https://doi.org/10.1051/0004-6361/200912846)
- Preston, R. A., Morabito, D. D., Williams, J. G., et al. 1985, AJ, 90, 1599, doi: [10.1086/113869](https://doi.org/10.1086/113869)
- Purcell, C. R., Hoare, M. G., & Diamond, P. 2008, in Astronomical Society of the Pacific Conference Series, Vol. 387, Massive Star Formation: Observations Confront Theory, ed. H. Beuther, H. Linz, & T. Henning, 389
- Pushkarev, A. B., Hovatta, T., Kovalev, Y. Y., et al. 2012, A&A, 545, A113, doi: [10.1051/0004-6361/201219173](https://doi.org/10.1051/0004-6361/201219173)
- Pushkarev, A. B., & Kovalev, Y. Y. 2012, A&A, 544, A34, doi: [10.1051/0004-6361/201219352](https://doi.org/10.1051/0004-6361/201219352)
- . 2015, MNRAS, 452, 4274, doi: [10.1093/mnras/stv1539](https://doi.org/10.1093/mnras/stv1539)
- Pushkarev, A. B., Kovalev, Y. Y., Lister, M. L., et al. 2013, A&A, 555, A80, doi: [10.1051/0004-6361/201321484](https://doi.org/10.1051/0004-6361/201321484)
- Readhead, A. C. S., & Wilkinson, P. N. 1978, ApJ, 223, 25, doi: [10.1086/156232](https://doi.org/10.1086/156232)
- Reid, M. J., & Honma, M. 2014, ARA&A, 52, 339, doi: [10.1146/annurev-astro-081913-040006](https://doi.org/10.1146/annurev-astro-081913-040006)
- Reid, M. J., Menten, K. M., Brunthaler, A., et al. 2014, ApJ, 783, 130, doi: [10.1088/0004-637X/783/2/130](https://doi.org/10.1088/0004-637X/783/2/130)
- Reid, M. J., Brunthaler, A., Menten, K. M., et al. 2017, AJ, 154, 63, doi: [10.3847/1538-3881/aa7850](https://doi.org/10.3847/1538-3881/aa7850)
- Rienecker, M., Suarez, M., Todling, R., et al. 2018, NASA Technical Memorandum, 104606, 1. <https://ntrs.nasa.gov/citations/20120011955>
- Rodriguez, C., Taylor, G. B., Zavala, R. T., et al. 2006, ApJ, 646, 49, doi: [10.1086/504825](https://doi.org/10.1086/504825)
- Schaer, S. 1999, Geod.-Geophys. Arb. Schweiz, Vol. 59., 59
- Schartner, M., & Böhm, J. 2020, Journal of Geodesy, 94, 12, doi: [10.1007/s00190-019-01340-z](https://doi.org/10.1007/s00190-019-01340-z)
- Schartner, M., Plötz, C., & Soja, B. 2021, Journal of Geodesy, 95, 58, doi: [10.1007/s00190-021-01512-w](https://doi.org/10.1007/s00190-021-01512-w)
- Schinkel, F. K., Petrov, L., Taylor, G. B., & Edwards, P. G. 2017, ApJ, 838, 139, doi: [10.3847/1538-4357/aa6439](https://doi.org/10.3847/1538-4357/aa6439)
- Schinkel, F. K., Petrov, L., Taylor, G. B., et al. 2015, ApJS, 217, 4, doi: [10.1088/0067-0049/217/1/4](https://doi.org/10.1088/0067-0049/217/1/4)
- Schlüter, W., & Behrend, D. 2007, Journal of Geodesy, 81, 379, doi: [10.1007/s00190-006-0131-z](https://doi.org/10.1007/s00190-006-0131-z)
- Sekido, M., Takiguchi, H., Koyama, Y., et al. 2008, Earth, Planets and Space, 60, 865, doi: [10.1186/BF03352838](https://doi.org/10.1186/BF03352838)
- Shen, Y., Chen, Y.-C., Hwang, H.-C., et al. 2021, Nature Astronomy, 5, 569, doi: [10.1038/s41550-021-01323-1](https://doi.org/10.1038/s41550-021-01323-1)
- Shepherd, M. C. 1997, in Astronomical Society of the Pacific Conference Series, Vol. 125, Astronomical Data Analysis Software and Systems VI, ed. G. Hunt & H. E. Payne (San Francisco: ASP), 77
- Shu, F., Petrov, L., Jiang, W., et al. 2017, ApJS, 230, 13, doi: [10.3847/1538-4365/aa71a3](https://doi.org/10.3847/1538-4365/aa71a3)

- Skrutskie, M. F., Cutri, R. M., Stiening, R., et al. 2006, *AJ*, 131, 1163, doi: [10.1086/498708](https://doi.org/10.1086/498708)
- Smith, H. E., Smith, E. O., & Spinrad, H. 1976, *Publications of the Astronomical Society of the Pacific*, 88, 621, doi: [10.1086/130001](https://doi.org/10.1086/130001)
- Sokolovsky, K. V., Kovalev, Y. Y., Pushkarev, A. B., & Lobanov, A. P. 2011, *A&A*, 532, A38, doi: [10.1051/0004-6361/201016072](https://doi.org/10.1051/0004-6361/201016072)
- Souchay, J., & Kinoshita, H. 1996, *A&A*, 312, 1017
— 1997, *A&A*, 318, 639
- Souchay, J., Loysel, B., Kinoshita, H., & Figueira, M. 1999, *A&AS*, 135, 111, doi: [10.1051/aas:1999446](https://doi.org/10.1051/aas:1999446)
- Sugiyama, K., Jaroenjittichai, P., Leckngam, A., et al. 2024, in *IAU Symposium*, Vol. 380, *Cosmic Masers: Proper Motion Toward the Next-Generation Large Projects*, ed. T. Hirota, H. Imai, K. Menten, & Y. Pihlström, 461–469, doi: [10.1017/S1743921323002909](https://doi.org/10.1017/S1743921323002909)
- Tasker, N. J., Condon, J. J., Wright, A. E., & Griffith, M. R. 1994, *AJ*, 107, 2115, doi: [10.1086/117022](https://doi.org/10.1086/117022)
- Thomas, C. C., MacMillan, D. S., & Le Bail, K. 2024, *Advances in Space Research*, 73, 317, doi: [10.1016/j.asr.2023.07.020](https://doi.org/10.1016/j.asr.2023.07.020)
- Thomas, J. 1980, *JPL Publ.*, 810–005
- Titov, O., Frey, S., Melnikov, A., et al. 2022, *MNRAS*, 512, 874, doi: [10.1093/mnras/stac038](https://doi.org/10.1093/mnras/stac038)
- Ulvestad, J. S., Fomalont, E. B., & Kimora, H. 1999, in *American Astronomical Society Meeting Abstracts*, Vol. 194, *American Astronomical Society Meeting Abstracts #194*, 50.23
- Véron-Cetty, M. P., & Véron, P. 2010, *A&A*, 518, A10, doi: [10.1051/0004-6361/201014188](https://doi.org/10.1051/0004-6361/201014188)
- Wehrle, A. E., Morabito, D. D., & Preston, R. A. 1984, *AJ*, 89, 336, doi: [10.1086/113518](https://doi.org/10.1086/113518)
- White, R. L., Becker, R. H., Helfand, D. J., & Gregg, M. D. 1997, *ApJ*, 475, 479, doi: [10.1086/303564](https://doi.org/10.1086/303564)
- Wilkinson, P. N., Browne, I. W. A., Patnaik, A. R., Wrobel, J. M., & Sorathia, B. 1998, *MNRAS*, 300, 790, doi: [10.1046/j.1365-8711.1998.01941.x](https://doi.org/10.1046/j.1365-8711.1998.01941.x)
- Wright, A. E., Griffith, M. R., Burke, B. F., & Ekers, R. D. 1994, *ApJS*, 91, 111, doi: [10.1086/191939](https://doi.org/10.1086/191939)
- Wright, A. E., Griffith, M. R., Hunt, A. J., et al. 1996, *ApJS*, 103, 145, doi: [10.1086/192272](https://doi.org/10.1086/192272)
- Wright, E. L., Eisenhardt, P. R. M., Mainzer, A. K., et al. 2010, *AJ*, 140, 1868, doi: [10.1088/0004-6256/140/6/1868](https://doi.org/10.1088/0004-6256/140/6/1868)
- XMM-SSC. 2018, *VizieR Online Data Catalog*: XMM-Newton slew survey Source Catalogue, version 2.0 (XMM-SSC, 2017), *VizieR On-line Data Catalog*: IX/53. Originally published in: XMM-SSC, Leicester, UK (2017)
- Xu, M. H., Savolainen, T., Anderson, J. M., et al. 2022, *A&A*, 663, A83, doi: [10.1051/0004-6361/202140840](https://doi.org/10.1051/0004-6361/202140840)
- York, D. G., Adelman, J., Anderson, John E., J., et al. 2000, *AJ*, 120, 1579, doi: [10.1086/301513](https://doi.org/10.1086/301513)